Title
Magnetic Resonance Investigations of Adsorbate Dynamics in Metal-Organic Frameworks

Author
Chen, Joseph Jung-Wen

Publication Date
2014

Peer reviewed|Thesis/dissertation

Magnetic Resonance Investigations of Adsorbate Dynamics in Metal-Organic Frameworks

By

Joseph Jung-Wen Chen

A dissertation submitted in partial satisfaction of the
requirements for the degree of
Doctor of Philosophy

in

Chemical Engineering
in the
Graduate Division
of the
University of California, Berkeley

Committee in charge:

Professor Jeffrey A. Reimer, Chair
Professor Susan J. Muller
Professor Jeffrey R. Long

Fall 2014

Magnetic Resonance Investigations of Adsorbate Dynamics in Metal-Organic Frameworks

Abstract

Magnetic Resonance Investigations of Adsorbate Dynamics in Metal-Organic Frameworks

By

Joseph Jung-Wen Chen

Doctor of Philosophy in Chemical Engineering
University of California, Berkeley
Professor Jeffrey A. Reimer, Chair

Metal-organic frameworks (MOFs), a new class of porous materials, are crystalline networks of metal clusters or ions connected by organic linkers through coordination bonds. These frameworks exhibit a rich diversity of structures, chemistries, and topologies, as evidenced by the explosion of new MOF structures in the last decade. However, the nearly infinite number of possible network connectivities and framework compositions, as well as the significant impact of minor changes in reaction conditions on the structure obtained, impedes optimization. Although high-throughput synthesis can greatly accelerate the discovery of new materials, the speed of subsequent characterization, such as gas adsorption measurements, limits the rate of optimization. In response to this challenge, we describe the development of a high-throughput nuclear magnetic resonance (NMR) porosity screening tool that uses NMR relaxation times of adsorbed molecules to estimate porosity. The diffusion and exchange processes uncovered during the development of this NMR screening tool highlight the lack of a molecular understanding of how adsorbed molecules, or guests, move in metal-organic frameworks. Thus, we investigate adsorbate dynamics in detail using NMR relaxation and diffusion experiments. Our relaxation experiments, combined with molecular simulations, establish the presence of a new condensation phenomenon occurring in a model adsorbate-MOF system. Our diffusion studies explore the interplay between the adsorbate-adsorbent interaction energy and this new condensation phenomenon on adsorbate diffusion in MOFs. These fundamental investigations, as well as our more practical efforts in developing a porosity screening tool, provide detailed insight into molecular dynamics in confined systems, and this knowledge possesses broad implications for applications in separations and catalysis.

Dedication

It would be an understatement to say that my years in graduate school have been the most eventful of my young life. Unsurprisingly, this turmoil has also yielded great personal change and growth. It is without question that I sincerely owe such growth to the support of my mentors, colleagues, friends, and family.

To Professor Jeff Reimer, my adviser, who, possessing at times a bewildering level of optimism and patience, allowed me to explore, to fail, and then, to finally succeed.

To the Reimer Group members who humored my scientific questions, my bad jokes, my grumpy grumbles, and all my other tics that only appear when you spend countless hours together.

To the Segalman Group members, who, in addition to their unwavering support, impressed upon me the level of scientific rigor necessary for good research.

To Dr. Bruce Eldridge and Kathleen Dyre for their guidance, wisdom, and affection for their partially adopted son.

To my friends Eric, David, Berger, and Alan, for being the brothers I never had.

To Bijal, Quyen, Robert, and Janis for being my most steadfast friends and picking me up even in my worst moments.

Finally, to my family, Mom, Dad, and Joanna. As the youngest in the family, I have always loved, admired, and looked up to you all. You provide the inspiration and the motivation that underlies all of my ambitions to better myself, in my career and in life.

Contents

List of Figures

List of Tables

Chapter 1
Introduction

1.1 Overview and Motivation

Porous materials serve as critical components in a vast number of industrial processes across a plethora of industrial sectors. Common industrial porous materials, such as zeolites, porous silicas, and porous carbons, can be found in membranes, heterogeneous catalysts, and adsorbents in chemical plants, petroleum refineries, and water treatment facilities, to name a few. The vast number of applications for porous materials motivates our efforts to improve their performance. Tailoring the pore structure and chemistry for the desired application is one strategy to achieve such improvements. Unfortunately, zeolites, porous silicas, and porous carbons all possess chemically inflexible systems that defy easy, controllable modification. In contrast, metal-organic frameworks (MOFs), a new class of porous materials, are crystalline networks of metal clusters or ions connected by organic linkers through coordination bonds. These frameworks exhibit a rich diversity of structures, chemistries, and topologies, as evidenced by the explosion of new MOFs in the last decade.[1] This inherent tunability has led to novel materials exhibiting record-breaking porosities and specific surface areas.[2-3]

Despite this rapid structural development, many challenges remain before MOFs can serve as useful industrial materials. Optimization of these frameworks for a given application remains difficult due to the effectively infinite number of metal-ligand combinations and the large number of phases that can emerge for even a single choice of metal and ligand. The modular nature of the solventothermal preparation of metal-organic frameworks makes high-throughput synthesis an effective means for rapidly exploring the parameter space.[4-6] However, the subsequent characterization of new compounds, which is relatively slow, now becomes a bottleneck. In response to this challenge, we describe the development of a high-throughput nuclear magnetic resonance (NMR) porosity screening tool. This tool uses NMR relaxation times of adsorbed solvent as a contrast mechanism to distinguish between adsorbed and free

liquid molecules and can help expedite the optimization of MOFs in a high-throughput workflow.

The diffusion and exchange processes uncovered during the development of this NMR screening tool highlight the lack of a molecular understanding of how adsorbed molecules move in metal-organic frameworks. Since the efficacy of these frameworks in application, such as in separations or heterogeneous catalysis, depends strongly on the rates of mass transfer, an understanding of adsorbate motion is critical for MOF development. Therefore, we investigate adsorbate dynamics in detail using NMR diffusion and relaxation experiments. Our relaxation experiments, combined with molecular simulations, establish the presence of a new condensation phenomenon occurring in a model adsorbate-MOF system. Our diffusion studies explore the interplay between the adsorbate-adsorbent interaction energy and this new condensation phenomenon on adsorbate diffusion in MOFs. These fundamental investigations, as well as our more practical efforts in developing a porosity screening tool, provide detailed insight into molecular dynamics in confined systems on multiple length and time scales, and this knowledge possesses broad implications for applications in separations and catalysis.

1.2 Metal-Organic Frameworks

As previously mentioned, metal-organic frameworks are porous crystalline solids consisting of networks of metal clusters or ions connected by organic linkers through coordination bonds. These frameworks are generally synthesized by dissolving the ligands and metal salts in a solvent at elevated temperatures, though many other types of synthetic methods exist.[7] Since these structures are held together by coordination bonds, the resulting frameworks are less thermally stable than covalently-bound porous structures (e.g. zeolites). However, since coordination bonds are generally reversible during synthesis, the growing structure can rearrange to eliminate defects, resulting in a near-ideal crystalline porous material.

A classic example of a metal-organic framework is MOF-5 (IRMOF-1, $Zn_4O(BDC)_3$, BDC = 1,4-benzenedicarboxylate)[8] as shown in Figure 1.1. This cubic framework consists of $Zn_4(O)O_{12}C_6$ clusters acting as "vertices" of the cube and BDC linkers acting as the "edges" of the cube. The rigidity of the structure allows for the MOF to remain crystalline and porous even after evacuation of the synthetic solvent (i.e. "permanent porosity"). MOF-5 was the first metal-organic framework to possess this characteristic, as previous frameworks tended to collapse upon the removal of solvent molecules. Combined with its structural simplicity, ease of preparation, and high porosity (79% by volume), MOF-5 is a near-ideal porous system, and therefore, is arguably the most studied metal-organic framework. Furthermore, by varying the linker

chemistry with the same connectivity, the pore chemistry and pore size of MOF-5 can easily be tuned while still maintaining the same cubic topology. The IRMOF series (see Figure 1.1), so named for their isoreticular, or topologically identical, structures, illustrates this concept by replacing BDC with other dicarboxylic acids (NH_2-BDC, 2-aminoterepthalate; BPDC, biphenyl-4,4'-dicarboxylate; and TPDC, *p*-tertphenyl-4,4"-dicarboxylate).

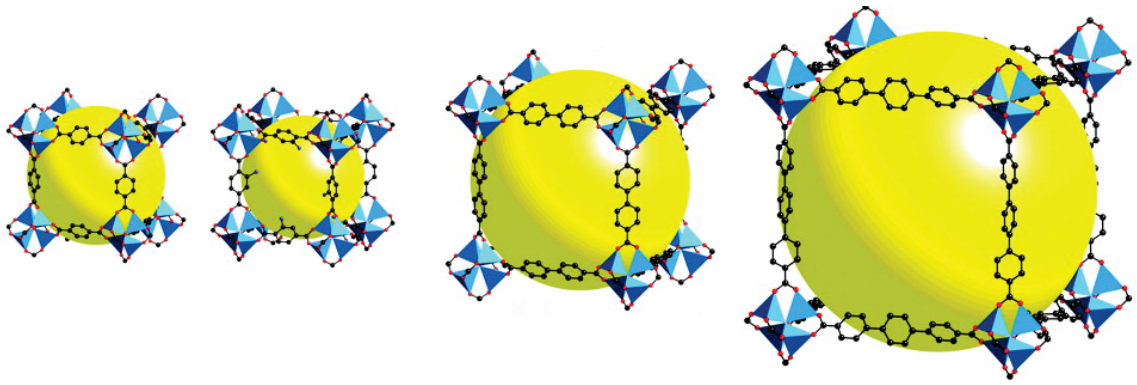

Figure 1.1. Crystal structures of the IRMOF series.[3] Left to right: MOF-5 or IRMOF-1 with BDC linkers, IRMOF-3 with NH_2-BDC linkers, IRMOF-10 with BPDC linkers, and IRMOF-16 with TPDC. All possess the same cubic topology and $Zn_4(O)O_{12}C_6$ clusters at the vertices. Color scheme is as follows: Zn (blue polyhedra), O (red spheres), C (black spheres), and N (grey spheres), with hydrogen atoms omitted. The yellow spheres represent the largest sphere that would fit in the pore cavities.

Mixtures of linkers with different chemical functionalities can also be incorporated into the cubic MOF-5 topology, resulting in multivariate frameworks, or MTV-MOFs, adding further complexity in tuning the chemistry of the pore space.[9]

Many other different framework topologies and chemistries have been explored, with notable examples being HKUST-1[10-11] and MOF-74 structures.[12-16] The former possesses three-dimensionally interconnected pores of two different sizes and is as well-studied as MOF-5. The latter possesses hexagonal one-dimensional pores that are lined with uncoordinated metal sites at the vertices. These uncoordinated sites give frameworks in this family unique adsorption properties and presents opportunities for post-modification.[17] The chemistry and properties of both HKUST-1 and MOF-74 structures can also be easily tuned by changing the metal type.[11, 14] Some frameworks, such as those in the MIL-53 family of structures, exhibit framework flexibility that allows for pores to open and close, leading to complex adsorption behavior.[18]

Other frameworks, such as those in the UiO-66 family, possess outstanding thermal and moisture stability that make these materials attractive for practical application.[19]

In summary, metal-organic frameworks offer an unprecedented level of structural control, which had led to great interest in the development of these porous materials for industrial purposes. This structural control also presents an ideal opportunity for fundamental studies of the transport and interfacial phenomena of porous materials in general.

1.3 Nuclear Magnetic (NMR) Relaxometry and Diffusometry

Nuclear magnetic resonance (NMR) operates on the energy differences of spin-active nuclei placed in a magnetic field. An isolated spin-½ nucleus (e.g. ^{1}H and ^{13}C) can be thought of as possessing a magnetic moment and two energy states when subject to a magnetic field: aligned and anti-aligned with the magnetic field. The energy of the anti-aligned state is higher than that of the aligned state, though this energy is extremely small (<<kT at room temperature). Nevertheless, because of this energy difference, an ensemble of spin-½ nuclei at equilibrium possesses a net magnetic moment aligned with the magnetic field. This effect, called the Zeeman effect, forms the basis of magnetic resonance, and the energy difference can be modulated by a plethora of interactions that affect the local magnetic field surrounding the nuclei (e.g. chemical shift, electric quadrupole coupling, J-coupling, dipole-dipole coupling, etc.).[20] In general, NMR spectroscopy encompasses the study of these energy differences.

NMR relaxometry and diffusometry operate under the same principles as NMR spectroscopy, but instead, focuses on how molecular motions affect the lifetime of magnetization. To describe these transient effects, a model is required, and for spin-½ nuclei, the Bloch-Torrey equations[21] provide a sufficient description of the relevant spin dynamics. This equation describes the time evolution of the magnetization vector $\boldsymbol{M}(\boldsymbol{r},t)$ with Fick's second law assuming isotropic diffusion and ignoring convection.

$$\frac{\partial \boldsymbol{M}(\boldsymbol{r},t)}{\partial t} = \gamma \boldsymbol{M} \times \boldsymbol{B}(\boldsymbol{r},t) - \frac{(M_z - M_0)}{T_1} - \frac{M_x \boldsymbol{i} + M_y \boldsymbol{j}}{T_2} + D\nabla^2 \boldsymbol{M} \qquad 1.1$$

In this equation, the first term describes the interaction of the magnetization with the magnetic field $\boldsymbol{B}$, which in the case of a static applied field by convention $B_x = B_y = 0$ and $B_z = B_0$. The gyromagnetic ratio, or γ, describes the proportionality between the magnetic field strength and the resonance, or Larmor, frequency. The second and third terms introduce two decay time

constants that return the non-equilibrium magnetization back to equilibrium in an exponential fashion. The magnetization along the z-axis, or M_z, decays back to its equilibrium value M_0 along the positive z-axis with a time constant T_1, called the spin-lattice or longitudinal relaxation time. The magnetization in the x-y plane, described by M_x and M_y, is zero at equilibrium, and the corresponding decay constant is T_2, the spin-spin or transverse relaxation time. Finally, the last term describes the effect of molecular self-diffusion, with a coefficient of D, on the magnetization.

By monitoring the time-dependence of the magnetization with various experiments (e.g. spin echo experiments), the relaxation time constants and the diffusion coefficients can be measured. The values of T_1 and T_2 are governed by the underlying molecular motions that cause the local magnetic field surrounding the active nuclei to fluctuate with time. In turn, these fluctuations drive spin transitions that return the spin state to equilibrium. The same interactions that affect NMR spectra by perturbing the local magnetic field, such as chemical shift, dipole-dipole coupling, and quadrupolar coupling interactions, are also mechanisms for relaxation. By identifying the relevant mechanisms and measuring T_1 and T_2, a detailed description of molecular motions can be obtained. Diffusion coefficients are most often measured by the application of a uniform field gradient in the z-axis ($B_z=B_0+gz$) during the experiment, where g is strength of the field gradient.[22] In essence, the gradient labels the position of nuclei using the Larmor frequency which allows for the observation of translational motion. The specifics of relaxation and diffusion measurements will be described in the relevant chapters.

Chapter 2

Ex-Situ Relaxometry of Metal-Organic Frameworks for Rapid Surface Area Screening

2.1 Abstract

Metal-organic frameworks represent a rapidly emerging class of crystalline porous materials exhibiting exceptional physical properties and chemical tunability. However, the nearly infinite number of possible network connectivities and framework compositions, as well as the significant impact of minor changes in reaction conditions on the structure obtained, impede materials optimization towards specific applications. Although high-throughput synthesis can greatly accelerate the discovery of new materials, the speed of subsequent characterization, such as gas adsorption measurements, limits the rate of optimization. Here, we demonstrate a robust characterization technique to estimate the surface area of a variety of microporous metal-organic frameworks and zeolites using the NMR relaxation behavior of imbibed solvent. This technique is amenable to automation and can expedite the characterization of microporous materials by identifying and discarding any non-porous or low-surface area structure, precluding the need for time-consuming gas adsorption analysis in the initial stages of a discovery workflow.

2.2 Introduction

Metal-organic frameworks can exhibit exceptional gas storage capacities and adsorptive selectivities;[2, 14-15, 23-26] these properties have led to their investigation for a vast number of applications.[27-28] However, optimization remains difficult due to the effectively infinite number of metal-ligand combinations and the large number of phases that can emerge for even a single choice of metal and ligand. Synthetic reaction conditions play a crucial role in determining which phase precipitates from solution. Thus, preparation of the desired material in pure, crystalline form relies on extensive systematic screening of many reaction parameters.[7, 29-30] The modular

nature of the solventothermal preparation of metal-organic frameworks makes high-throughput synthesis an effective means for rapidly exploring the parameter space.[4-6] However, the subsequent characterization of new compounds becomes a bottleneck for this type of workflow, since structural characterization by X-ray diffraction (XRD) or evaluation of the Brunauer-Emmett-Teller (BET) surface area via adsorption measurements are not practical for large numbers of unknown samples. Thus, the development of a porosity analysis tool that precludes the need to perform labor-intensive tasks (i.e. activation and sorption measurements) on each sample would greatly accelerate the discovery of potentially interesting frameworks by quickly eliminating non-porous or low-surface area materials that are not of interest.

Nuclear magnetic resonance (NMR) relaxometry can potentially provide an initial estimate of the pore volume and surface area of an unknown metal-organic framework. These methods use imbibed fluid nuclei as probes of the internal surface area and have been used extensively to characterize porous media, including rocks, silica, zeolites, cements, and soils.[31-47] The transverse relaxation rate (T_2) of liquid nuclei imbibed in porous media generally depends on the degree of confinement due to interactions with the pore walls[48] and internal field gradients.[45, 49] Though some relaxation studies of hydrocarbon gases in MOF-5 and $Cu_3(BTC)_2$ have been conducted,[50-52] the relaxation behavior of liquids in metal-organic frameworks and its connection to internal surface area has yet to be studied systematically.

Herein, we demonstrate a correlation between the BET surface area and the transverse relaxation of solvent-imbibed metal-organic frameworks and zeolites. The use of a liquid probe greatly simplifies sample preparation to washing and filtration, minimizing the amount of necessary automation hardware while eliminating the time-consuming process of sample isolation and activation. Furthermore, the relaxation measurements described in this study can be performed considerably faster than a typical BET surface area measurement. Lastly, the integration of autosampling hardware allows large numbers of samples to be screened without the need for manual sample transfer or instrument operation, providing a convenient initial screening method well-suited for integration into a high-throughput workflow (see Appendix F). Note that this technique does not replace adsorption-based characterization experiments, but should facilitate the identification of a generally small fraction of highly porous materials within a combinatorial library of unknown samples, allowing researchers to perform time-consuming workup on the most promising frameworks.

2.3 Experimental Details

2.3.1 Preparation of Na-faujasite, Na-mordenite, and Ni-Na-X Zeolites

Na-faujasite (Si:Al = 2.6) and Na-mordenite (Si:Al = 6.5) were purchased from Zeolyst. Na-faujasite samples were dried at 413 K under vacuum to remove residual adsorbed water. Due to smaller pore sizes and evidence of residual water after the previous vacuum drying, Na-mordenite samples were treated with a more rigorous calcination procedure as reported in literature.[53] N_2 adsorption experiments were carried out on the dried samples using a Micromeritics Tristar 3000 instrument.

Ni–Na-X was prepared and characterized as previously reported.[53]

2.3.2 Synthesis and Activation of Metal-Organic Frameworks

All reagents were obtained from commercial vendors and used without further purification. UHP-grade (99.999% purity) nitrogen and helium were used for all adsorption measurements. Powder X-ray diffraction patterns were collected on a Bruker AXS D8 Advance diffractometer equipped with Cu-Kα radiation (λ = 1.5418 Å), a Göbel mirror, a Lynxeye linear position-sensitive detector, and mounting the following optics: fixed divergence slit (0.6 mm), receiving slit (3 mm), and secondary beam Soller slits (2.5°). The generator was set at 40 kV and 40 mA.

Gas adsorption isotherms were measured using a Micromeritics ASAP 2020 instrument. For standard measurements in ASAP low-pressure glass sample holders, activated samples were transferred under a N_2 atmosphere to preweighed analysis tubes, which were capped with a Transeal. The samples were evacuated on the ASAP until the outgas rate was less than 3 μbar per min. The evacuated analysis tubes containing degassed samples were then carefully transferred to an electronic balance and weighed to determine the mass of sample (typically 100-200 mg). The tube was fitted with an isothermal jacket and transferred back to the analysis port of the gas adsorption instrument. The outgas rate was again confirmed to be less than 3 μbar per min. Langmuir surface areas were determined by measuring N_2 adsorption isotherms in a 77 K liquid N_2 bath and calculated using the Micromeritics software, assuming a value of 16.2 $Å^2$ for the molecular cross-sectional area of N_2. All isotherms measured are shown in Figure B.4.

The compound Mg_2(dobdc) was prepared and activated according to literature procedure.[14, 54] The successful synthesis and activation of the framework was confirmed by comparing the X-ray powder diffraction pattern and Langmuir and BET surface areas to those previously reported (see Figure B.1).

The compound Zn_2(dobdc) was synthesized and activated in a manner similar to that previously reported.[2a] Here, $Zn(NO_3)_2 \cdot 6H_2O$ (1.911 g, 6.424 mmol) and 2,5-dihydroxyterephthalic acid (H_4dobdc) (0.5760 g, 2.907 mmol) were dissolved in a mixture of 240 mL of *N*,*N*,-dimethylformamide (DMF), 16 mL of absolute ethanol, and 16 mL of deionized water. This solution was distributed into twenty-four 20 mL vials and heated on a dry bath at 120 ˚C for 24 hours. The yellow microcrystalline Zn_2(dobdc) was collected from the vials and combined into a 100 mL jar. The mother liquor was exchanged for anhydrous DMF, and the sample was transferred to a glove box. The material was soaked in DMF at 100 ˚C. The DMF was exchanged four times over a period of two days. Similarly, methanol washes at 70 ˚C were performed every 8 hours for a total of eight washes. The material was then activated under vacuum for 24 hours at 180 ˚C prior to the 77 K N_2 adsorption measurement. The successful synthesis and activation of the framework was confirmed by comparing the X-ray powder diffraction pattern and Langmuir and BET surface areas to those previously reported (see Figure B.2).

The compound Co_2(dobdc) was prepared and activated according to literature procedure.[2a] Here, the red microcrystalline Co_2(dobdc) was activated under vacuum for 24 hours at 180 ˚C after DMF and methanol washes. The successful synthesis and activation of the framework was confirmed by comparing the X-ray powder diffraction pattern and Langmuir and BET surface areas to those previously reported (see Figure B.2).

The compound Ni_2(dobdc) was prepared and activated according to literature procedure.[2a] Here, the brown microcrystalline Ni_2(dobdc) was activated under vacuum for 24 hours at 180 ˚C after DMF and methanol washes. The successful synthesis and activation of the framework was confirmed by comparing the X-ray powder diffraction pattern and Langmuir and BET surface areas to those previously reported (see Figure B.2).

The compound Cu-HKUST-1 was synthesized and activated in a manner similar to that previously reported.[55] Here, $Cu(NO_3)_2 \cdot 2.5H_2O$ (8.750 g, 37.63 mmol) and 1,3,5-benzenetricarboxylic acid (H_3BTC) (4.200 g, 20.00 mmol) were dissolved in 250 mL of absolute ethanol in a 500 mL round-bottom flask. The resulting solution was refluxed at 70 ˚C for 48 hours. The resulting blue Cu-HKUST-1 was recovered by filtration and placed under vacuum at 100˚C for 24 hours until the material turned a deep purple. The successful synthesis and activation of the framework was confirmed by comparing the X-ray powder diffraction pattern and Langmuir and BET surface areas to those previously reported (see Figure B.3).

The compound UiO-66 was synthesized and activated in a manner similar to that previously reported.[19, 56] Here, $ZrCl_4$ (0.4672 g, 2.000 mmol) and 1,4-benzenedicarboxylic acid (H_2BDC) (0.6589 g, 4.000 mmol) were dissolved in 77 mL of DMF and 3.4 mL of acetic acid.

This stock solution was distributed into eight 20 mL vials. The vials were heated on a dry bath at 120 ˚C for 24 hours. The resulting white powder was recovered by filtration. Four DMF exchanges were performed at 70 ˚C over the course of two days. The DMF was then decanted and replaced with CH_2Cl_2. The UiO-66 was soaked in CH_2Cl_2 at 25˚C for a minimum of 6 hours between each of the 6 CH_2Cl_2 exchanges. The UiO-66 was then activated under dynamic vacuum at 120 ˚C for 24 hours. The successful synthesis and activation of the framework was confirmed by comparing the X-ray powder diffraction pattern and Langmuir and BET surface areas to those previously reported (see Figure B.3).

2.3.3 Solvent Imbibition

MOFs were imbibed by flashing the solvent into an evacuated (~7 Pa for one hour) chamber containing the MOF then allowing the MOF to soak overnight. This ensured that no gas would be trapped in the MOF so that the solvent would fully penetrate any accessible pore volume. The MOFs were then filtered and dried in a N_2 atmosphere to evaporate excess solvent. Subsequent thermogravimetric analysis (TGA Q50, TA Instruments, New Castle, DE) was used to quantify solvent content of the solvent-filled MOF (see Appendix B.3). Approximately 3 mg of solvent-loaded powder was placed on a 100 μL platinum sample pan. Samples were held at room temperature for 10 minutes then heated to 500˚C at 1˚C per min under a nitrogen purge. Solvent content was determined from the mass loss prior to degradation temperatures for each material. Solvent content was normalized to the dry weight of the MOF sample, and was systematically varied by micropipette addition or thermal evaporation. Finally, NMR experiments were conducted using the same MOF samples tested by adsorption experiments and focused on collecting NMR data with higher signal-to-noise, though the measurement time was still kept to a reasonable length in light of high-throughput requirements (~30 minutes per CPMG experiment). Identical NMR experiments were performed multiple times on each sample to quantify the error of the NMR experiment as well as the variability of the least-squares fit to experimental noise. Each sample consisted of ~10-15 mg of solvent-loaded MOF in a 6 mm ID glass vial tightly sealed with a plastic cap.

2.3.4 NMR Experimental Procedures

^{1}H-NMR relaxation was measured using a single-sided 13.1 MHz Profile NMR-MOUSE (**MO**bile **U**niversal **S**urface **E**xplorer) magnet[57-59] where the sample is placed in the stray field of a permanent magnet (Figure 2.1) with a linear gradient of 7 $T \cdot m^{-1}$. A Kea II spectrometer was used for pulse generation and signal acquisition, and all pulse programs,

including automation software, was written using Prospa v3.11 software package. An automated sample handler built by J-KEM Scientific was used to handle vials from a 96-vial holder, and interfaces with the Kea II spectrometer via TTL outputs. Custom software was provided with the sample handler. NMR experiments are synced with the autosampler by sending on-off signals from the spectrometer to the robot, which is then interpreted by the autosampler software as a command to add or remove sample vials.

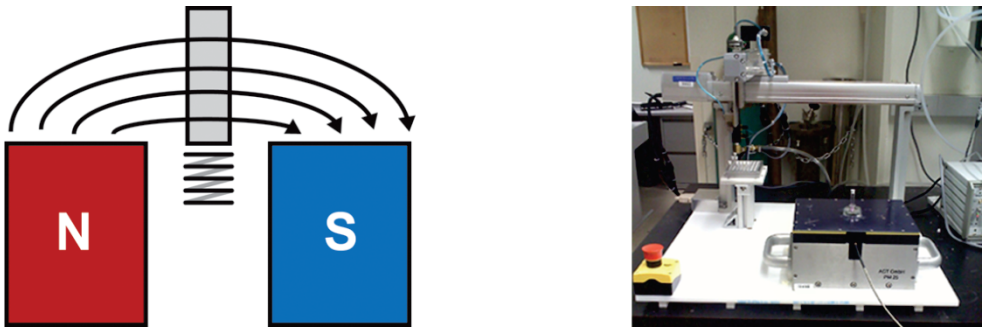

Figure 2.1. Schematic (left) of a single-sided magnet and picture (right) of the NMR-MOUSE with automation hardware (see Appendix F for further details on automation).

Carr-Purcell-Meiboom-Gill (CPMG) pulse sequences[60-61] were used to measure the T_2 relaxation of each sample. The pulse sequence parameters were optimized for accurate detection of short T_2 components and for maximum signal (2 μs excitation pulses with an echo time of 55 μs).[62] The length of the echo train was varied so that the entire T_2 decay could be acquired for each sample (i.e. when the signal decays to approximately the noise level). The recycle delay was determined using saturation recovery experiments on each sample. All samples were measured at ambient temperature, which was approximately 22 ± 2°C.

2.3.5 NMR Data Analysis Procedures

An algorithm for finding numerical solutions to a Fredholm integral equation of the first kind, known colloquially as an inverse Laplace transform (ILT) or Laplace inversion,[63-64] deconvolutes multi-exponential transverse relaxation into individual components. The ILT seeks to minimize the mismatch between the acquired data and the summation of prescribed exponential components. Further details about the Laplace inversion can be found in Appendix E.

2.4 Results and Discussion

2.4.1 T_2 Relaxation Distributions of Imbibed Frameworks

Samples of solvent-imbibed metal-organic frameworks can be approximated as having two pore size regimes, as shown in Figure 2.2 using Mg_2(dobdc) (Mg-MOF-74, CPO-27-Mg; $dobdc^{4-}$ = 2,5-dioxido-1,4-benzenedicarboxylate) as an example: nanometer-sized pores belonging to the inherent structure of the framework (intra-particle) and micron-sized voids between the individual crystallites (inter-particle).

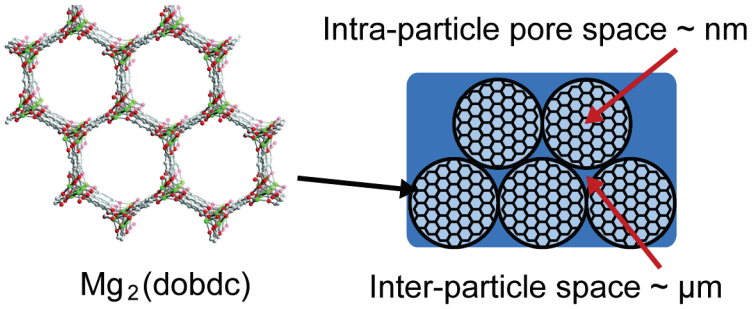

Figure 2.2. Crystal structure of Mg_2(dobdc) (left) and a schematic of packed particles indicating the two length scales formed (right). Green, grey and red spheres represent Mg, C and O atoms, respectively, while H atoms are omitted for clarity.

Since solvent molecules are expected to diffuse slowly between the two types of pores, relaxation should exhibit multi-exponential behavior, where faster relaxation occurs for intra-particle solvent, and slower relaxation for inter-particle solvent. An algorithm referred to as an inverse Laplace transform (ILT) or Laplace inversion, deconvolutes multi-exponential transverse relaxation into individual exponential components (Figure 2.3). Relaxation measurements were conducted on samples with known amounts of solvent using single-sided NMR-MOUSE (**MO**bile **U**niversal **S**urface **E**xplorer). This setup measures the ^{1}H-NMR signal of samples placed outside the magnet, simplifying the incorporation of automation hardware.

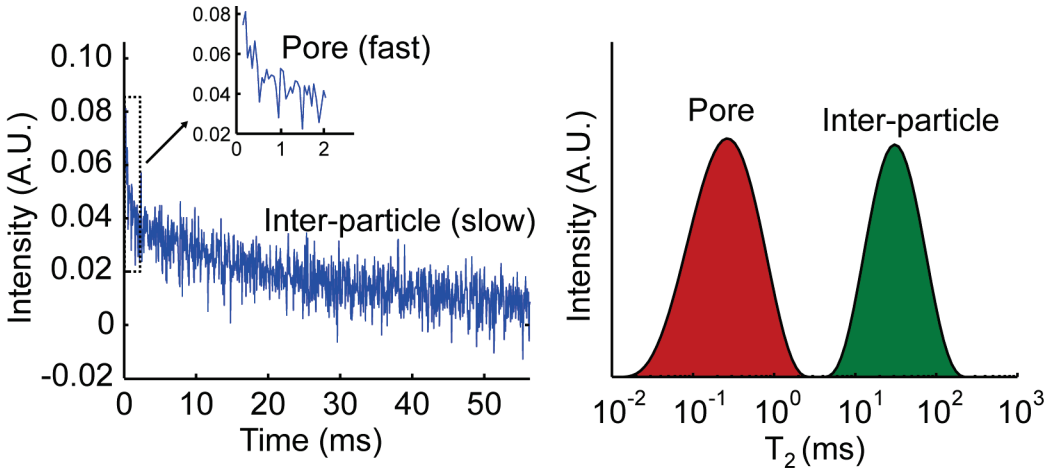

Figure 2.3. NMR signal vs. time showing relaxation with slow and fast exponential decays (left) and Laplace inversion of relaxation data with two relaxation populations corresponding to pore and inter-particle solvent (right).

As shown in Figure 2.4, the T_2 "relaxation spectra" of dimethyl sulfoxide (DMSO) protons imbibed in Mg_2(dobdc) (Figure 2.2; BET surface area = 1660 m^2g^{-1}) exhibits multi-exponential relaxation for a series of solvent contents. Note that DMSO was chosen as a probe solvent due to its common use in the synthesis of metal-organic frameworks and its inert nature towards most compounds. T_2 relaxation was measured using a CPMG sequence with an approximate experiment duration of 15-30 minutes.

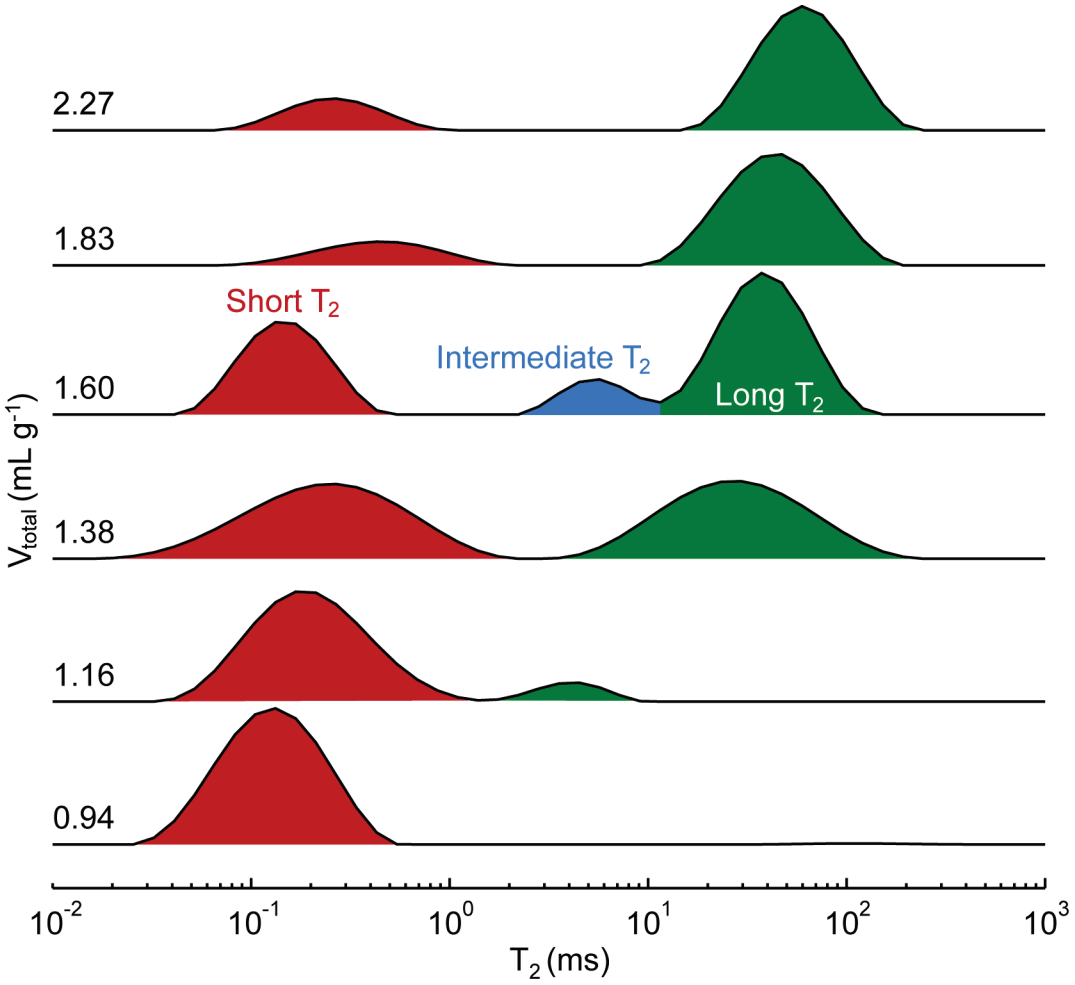

Figure 2.4. Profiles of T_2 relaxation times, or "relaxation spectra," for Mg_2(dobdc) with various amounts of DMSO added (V_{total}). Solvent content is normalized to the mass of the evacuated framework. Relaxation times can be roughly grouped into short, intermediate, and long T_2 regimes. The total intensity at each solvent content is normalized to unity.

At low solvent content, a single peak appears, representing a population of solvent with a short T_2 (~10^{-2} to 10^0 ms). Due to the short relaxation times compared to neat DMSO ($T_{2,DMSO}$ ≈ 300 ms on the NMR-MOUSE), the protons associated with this relaxation population reside on solvent molecules confined within the one-dimensional channels of Mg_2(dobdc). The presence of a single population indicates that little solvent exists in the inter-particle voids, which can be attributed to the much stronger solvent binding expected within the confines of the pores

compared to the voids between the individual particles. As solvent is added, a second population appears at longer T_2 (10^0 to 10^3 ms), and the corresponding relaxation peak shifts to longer times. Since the pores are completely filled at higher solvent contents, this peak can be assigned to inter-particle solvent. Successive solvent addition leads to a greater proportion of molecules that interact weakly with the framework, causing the relaxation time to approach the value for neat DMSO. Notably, a third intermediate relaxation population occasionally appears with intermediate relaxation times (10^0 to 10^1 ms). This range of relaxation times also corresponds to that for the long-T_2 peaks at lower solvent content which suggests that the intermediate relaxation peaks correspond to solvent localized near the surface of the particles rather than inside the framework pores. Sufficiently fast diffusional exchange between the pores and inter-particle space during the NMR experiment would indeed generate an intermediate relaxation environment, as discussed later. Also, note that each relaxation population is represented by broad peaks spanning orders of magnitude, and given the low signal-to-noise ratio associated with using the NMR-MOUSE and the uniform pore size of metal-organic frameworks, the breadth of the spectrum represents an uncertainty originating from experimental noise rather than the existence of a wide pore size distribution.

2.4.2 Porosity Analysis of Relaxation Distributions

Since the peak area in the relaxation spectrum is proportional to the number of spins (i.e., solvent volume) of that relaxation population, a direct connection between the pore volume and the relaxation distribution can be made. The surface area in microporous media is roughly proportional to the pore volume, and frameworks with high surface areas should exhibit relaxation spectra with proportionally larger short-T_2 peaks at a given solvent content. Indeed, the relaxation behavior for a variety of other samples, including low-surface area zeolites, metal-organic frameworks with paramagnetic metal centers (e.g., Ni_2(dobdc)), or frameworks with higher dimensionality pores (e.g., UiO-66), remains qualitatively similar to that for Mg_2(dobdc) (see Appendix C.1).

The fraction of total intensity encompassed by the short-T_2 peak corresponding to the solvent molecules within the micropores is shown in Figure 2.5 for Mg_2(dobdc) and a low-surface area zeolite Na-mordenite (BET surface area = 398 m^2g^{-1}). Note that the short-T_2 peak is defined as the fastest relaxation population in "relaxation spectra" displaying multiple peaks.

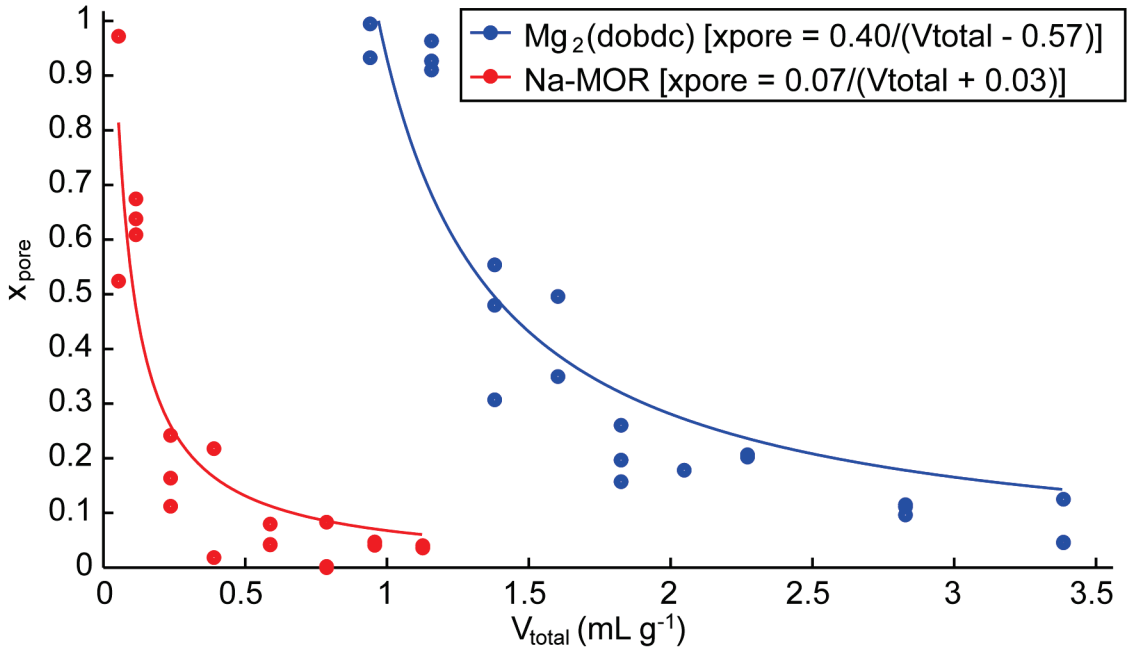

Figure 2.5. Decay of the fraction of total intensity (x_{pore}) encompassed by the pore-confined solvent plotted vs. increasing solvent content (V_{total}). The solid lines indicate the fits of the data with Eq. 1. Na-MOR is the zeolite sodium mordenite.

Spectra with single peaks are classified as belonging to either solvent within the pores or within the bulk liquid, depending on the magnitude of relaxation times. The fraction of total signal associated with pores (x_{pore}) should be equal to the ratio of the normalized pore volume to the normalized total solvent content ($V_{pore}V_{total}^{-1}$). However, a small amount of strongly-bound immobile solvent may go undetected due to the extremely short relaxation times that these nuclei exhibit (T_2 ~ 10 μs). Therefore, the ratio for x_{pore} must be modified, resulting in the expression below.

$$x_{pore}=\frac{V_{pore}-V_{total}}{V_{total}-V_{im}} \qquad 2.1$$

V_{im} represents the normalized volume of immobile solvent, and the fits of Eq. 1 are shown in Figure 2.5. For Mg_2(dobdc), V_{im} is relatively large, while for Na-MOR, the V_{im} is small (and positive due to experimental noise), indicating that Mg_2(dobdc) binds solvent more strongly than

Na-MOR, most likely due to the presence of open metal sites in Mg_2(dobdc). Figure 2.6 shows the correlation of V_{pore} with the experimental nitrogen BET surface area (SA_{BET}) for a variety of porous materials imbibed with DMSO. *N*,*N*-Dimethylformamide (DMF), a ubiquitous solvent in metal-organic framework synthesis, was also used as a probe solvent with similar results. A satisfactory linear correlation can be applied (Figure 2.6), the results of which are shown in Table D.1.

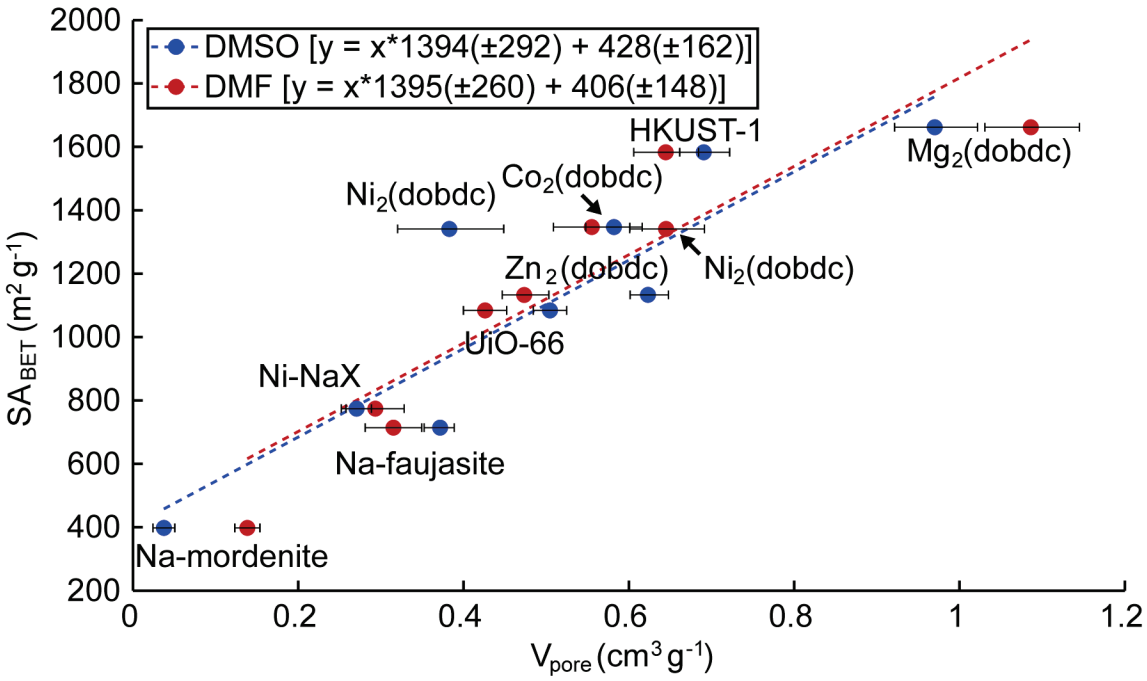

Figure 2.6. Correlation of BET surface area (SA_{BET}) to the fitted V_{pore} using DMSO and DMF. Dashed lines indicate the fit for each solvent. The error bars encapsulate the ILT error, the pore decay fitting error, and the error in NMR measurement. All samples were tested at room temperature.

The NMR-predicted surface area agrees well with the measured surface area, with error (± standard deviation) being dominated by the linear regression error that is expected to improve as more frameworks are tested and as the testing protocol is refined. The analysis clearly distinguishes low-porosity samples from high-surface area metal-organic frameworks, demonstrating its potential for implementation alongside high-throughput synthesis

instruments. Also, the flexibility in solvent choice could further simplify sample preparation by enabling testing of as-synthesized frameworks.

2.4.3 Bloch-Torrey Analysis of Relaxation Behavior

A PDE model was developed to further elucidate the physics of a diffusing, heterogeneous framework-solvent system and to understand the limitations of our analysis. This model utilizes the Bloch-Torrey equation (see Equation 1.1) to describe the evolution of NMR magnetization in a single spherically-symmetric particle of radius R_1 surrounded by varying amounts of bulk inter-particle solvent of thickness R_2 (Figure 2.7). Each region has its own diffusion coefficient and relaxation time, with $D_{pore} < D_{bulk}$ and $T_{2,\,pore} < T_{2,\,bulk}$ due to restriction by and interactions with the pore walls.

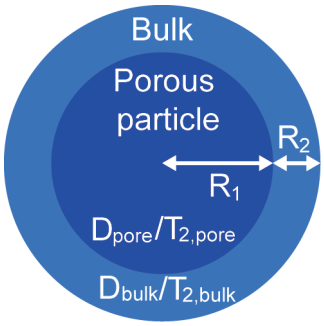

Figure 2.7. Schematic of Block-Torrey model describing relaxation of solvent in a single MOF particle.

The model calculates the temporal decay of the NMR signal due to relaxation and diffusion (see Appendix G.1 for further details). Note that the relaxation time inside the particle is assumed to be homogeneous. Since the diffusion length of a solvent molecule is typically larger than the pore diameter of MOFs and given the regularity of the framework structure, the relaxation time of the solvent inside the framework can be approximated as a single value.

An NMR magnetization decay was computed for base-case parameters (see Figure 2.8 below) and various film thicknesses (R2), mimicking the actual experiment of adding additional solvent. This decay was then subject to the same ILT process as "real" NMR data.

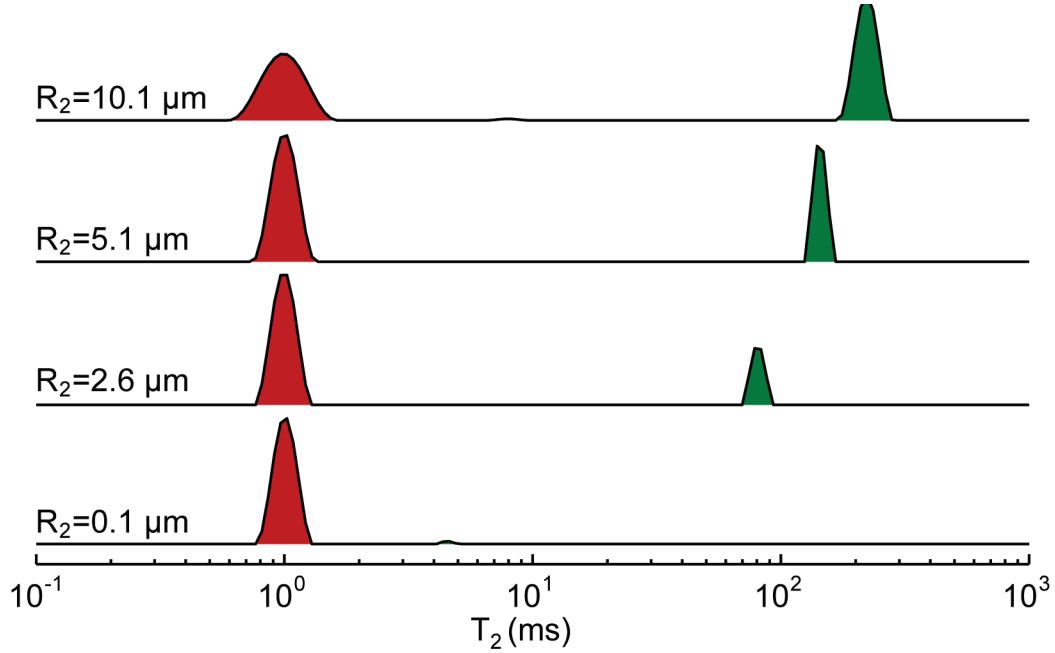

Figure 2.8. Relaxation distributions of magnetization decays generated by the Bloch-Torrey model. Parameters used are R_1 = 10 µm, $T_{2,pore}$ = 1 ms, $T_{2,bulk}$ = 300 ms, D_{pore} = 1 x 10^{-12} m^2/s, D_{bulk} = 7 x 10^{-10} m^2/s. Properties of the solvent are derived from measurements of neat DMSO on the NMR-MOUSE, while properties of pore-confined solvent are estimated.

The inversion spectra derived from the analytical model qualitatively match the results found in actual experiments. The short-T_2 relaxation peak represents the pore-confined solvent, and the steady increase in relaxation time of the long-T_2 peak seen in experiments represents the effect of diffusional exchange between the two phases; a simulation conducted with zero diffusion merely exhibited a peak at T_2 = 300 ms with increasing intensities.

Furthermore, this model supports the hypothesis that exchanging interfacial solvent produces intermediate relaxation peaks. Figure 2.9 shows the inversion spectra in the limiting case that the pore structure does not restrict diffusion.

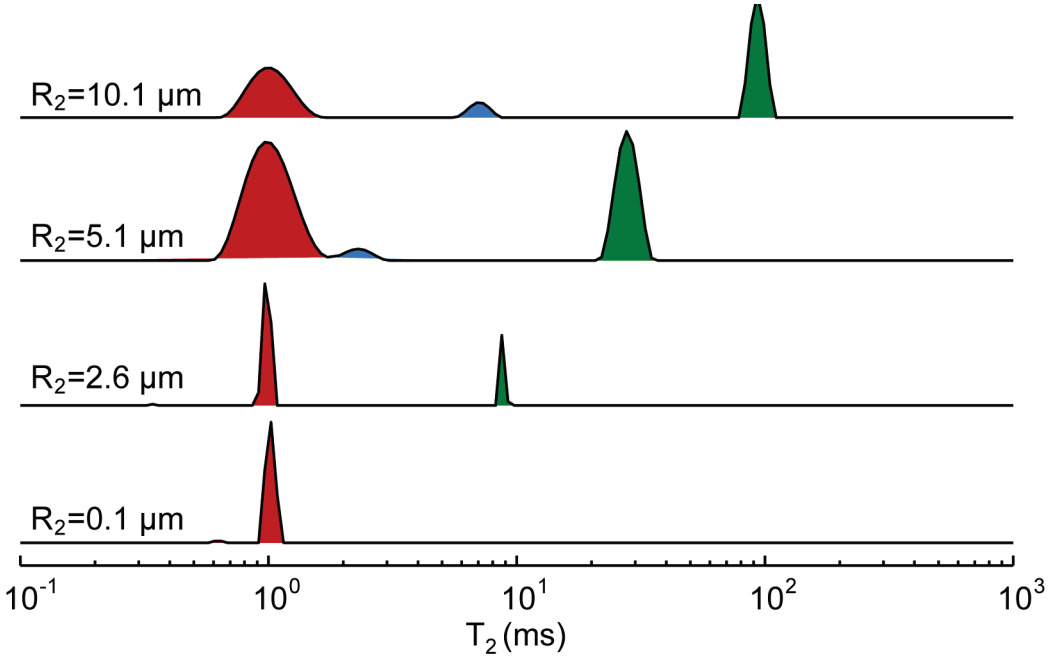

Figure 2.9. Relaxation distributions in the limiting case of unrestricted diffusion within the framework (D_{pore} = 7 x 10^{-10} m^2/s). All other parameters are kept similar to those shown in Figure 2.8.

The larger diffusion coefficient causes the long-T_2 peak position to increase more quickly with increasing R_2. This exchange also mixes the pore and bulk solvent on the timescale of the decay, resulting in intermediate relaxation conditions that are the likely origin of the intermediate relaxation peaks. Figure 2.10 compares the relaxation distributions of interfacial solvent with solvent away from the interface and the pore-confined solvent (R_2 = 10.1 μm). The large intermediate peak in the spectra for interfacial solvent suggests that the interface is indeed an intermediate relaxation environment. Both of these analyses strongly suggest the presence of diffusional exchange between pore and bulk-solvent and that such exchange generates intermediate relaxation populations at the particle interface.

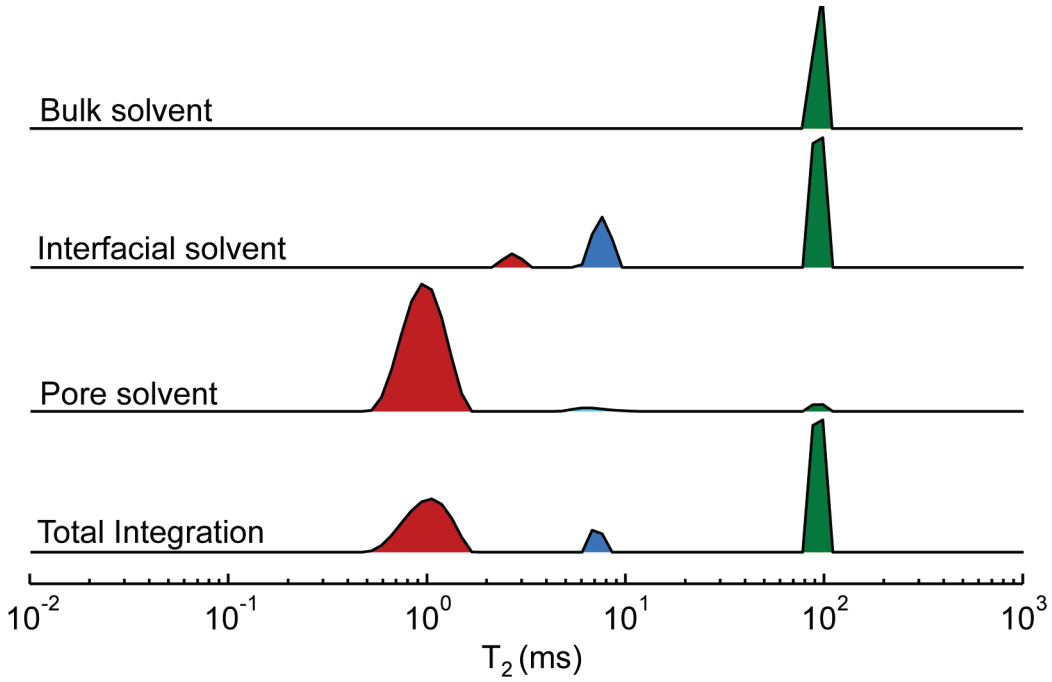

Figure 2.10. Laplace inversion of T_2 relaxation curves generated by the mathematical model based upon appropriate Bloch-Torrey equations. Inversions were performed on the separate relaxation signals from the pore solvent, the interfacial solvent, and the bulk solvent, as well as the total signal from all three. The interface is arbitrarily defined as the region spanned by $[R_1,R_1+5\ \mu m]$.

Increasing the rate of diffusional exchange affects the accuracy of peak integration in representing their respective solvent quantities. Changes in other parameters, such as a reduction in particle size or increase of $T_{2,pore}$, can also produce errors. The relevant dimensionless parameter is the ratio of the particle size to the diffusion length. Since exchange is most likely limited by diffusion in the framework, and since magnetization from the pore-confined solvent decays to zero with a timescale of $T_{2,pore}$, the relevant diffusion length would be $\langle r^2 \rangle = D_{pore} T_{2,pore}$. Additionally, experimental noise serves to broaden the peaks via increased regularization, further reducing the resolution of the relaxation spectra, creating scatter in the intensity fraction, and increasing the error of the analysis.[65]

2.5 Conclusions

The foregoing study has described a robust correlation relating the surface area of a wide variety of microporous media to the proton relaxation behavior of imbibed solvent, demonstrating the potential for NMR relaxometry as a high-throughput screening technique. The results were obtained on a portable NMR instrument that interfaces easily with combinatorial synthesis methods. Simulations using the Bloch-Torrey equations qualitatively confirm the observed behavior and allow the effects of solvent transport processes to be explored. Further optimization of sample preparation, measurement methodology, and NMR hardware should yield considerable reductions in error and measurement time. The inclusion of this technique in a high-throughput screening workflow is expected to expedite the discovery of new candidate materials.

2.6 Acknowledgements

The material herein was previously published[66] with coauthors Xueqian Kong, Kenji Sumida, Mary Anne Manumpil, Jeffrey R. Long, and Jeffrey A. Reimer. This work was supported by the U.S. Department of Energy, Advanced Research Projects Agency - Energy (ARPA-E) under Grant No. DE- AR0000103. Joseph Chen acknowledges a graduate fellowship through the National Science Foundation Graduate Research Fellowship Program. The authors acknowledge Mr. J. A. Mason and Mr. A. Milner for assistance with the sample preparation and Fulbright New Zealand for partial support of Kenji Sumida. The Laplace inversion software is used courtesy of Victoria University of Wellington.

Chapter 3
NMR Relaxation and Exchange in High-Porosity Metal-Organic Frameworks for Surface Area Screening

3.1 Abstract

We describe a robust screening technique that correlates the surface area of metal-organic frameworks to the proton T_2 relaxation behavior of imbibed solvent at low field (13 MHz). In frameworks with small pore sizes (<1 nm) or strong solvent-framework interactions, diffusional exchange between the pore-confined and inter-particle solvent populations remains slow compared to the T_2 of the pore-confined solvent, allowing for a direct porosity analysis of the T_2 spectrum obtained from Laplace inversions. Increases in framework pore-size (>1 nm) lead to corresponding increases in the rate of solvent exchange, as confirmed by T_2 relaxation exchange (REXSY) experiments; increases in the pore size also increases the T_2 of the pore-confined solvent. The combination of these two effects results in comparable rates of relaxation and exchange, which precludes the direct analysis of Laplace inversions. Thus, two- and three-site kinetic models were applied to extract porosity from relaxation decays, thereby improving the utility of the porosity screening tool.

3.2 Introduction

In the previous chapter we described a porosity-screening technique using nuclear magnetic resonance (NMR) relaxometry. This technique greatly simplified the necessary sample preparation for porosity analysis and reduced the measurement time, thus allowing for faster porosity characterization compared to a typical Brunauer-Emmett-Teller (BET) adsorption

experiment.[67] The rate of transverse (T_2) relaxation in a variety of solvent-imbibed metal-organic frameworks and zeolites correlated directly to the two pore-size regimes formed by packed porous particles: nanometer-sized pores belonging to the inherent structure of the framework (pore-confined) and micron-sized voids between the individual crystallites (inter-particle). The clear delineation between the relaxation times of the pore-confined molecules (~10^{-2} to 10^{0} ms) and the inter-particle molecules (~10^{0} to 10^{3} ms) indicated that exchange between the two populations occurred slowly compared to the timescale of relaxation. Thus, the corresponding peak areas for each population, which are proportional to the number of molecules in each population, were directly analyzed to yield an NMR-derived porosity that strongly correlated to the BET surface area.

Direct analysis of the relaxation distributions analysis hinges upon the ability to distinguish clearly the relaxation times of the pore-confined and inter-particle solvent. Diffusional exchange between the two results in relaxation distributions that no longer reflect the size of each population, and in the limiting case of fast exchange, the observed relaxation time is a weighted average of each population's relaxation rates.[43, 68-70] Thus, the limitations of direct analysis depend on the relative magnitudes of the diffusion length and the particle size since solvent molecules that remain within the porous particle during the timescale of the experiment do not exchange with the inter-particle molecules. This direct analysis is also limited by the inherent difference in relaxation times between the pore and inter-particle populations, as well as by the resolution limits of the Laplace inversion algorithm used to deconvolute multi-exponential signals.[65] Given that the relaxation time of pore-confined molecules scales roughly with the pore radius, frameworks with larger pores (>1 nm) would likely exhibit longer pore relaxation times. Furthermore, larger pores would decrease the restrictions on diffusion within the framework, resulting in faster exchange. Because of these limitations, the "direct analysis" method was constrained to frameworks with BET surface areas of approximately 1700 m^2/g or less (< 1 nm pore sizes). Many important frameworks possess pore sizes greater than 1 nm, since in microporous media (<2 nm pore size), pore volume, porosity, and surface area are proportional to pore size. Thus, the constraint on pore-size greatly limits the utility of the technique. Notably, the M_2(dobdc) (MOF-74, $dobdc^{4-}$ = 2,5-dioxido-1,4-benzenedicarboxylate, M = Mg, Ni, Co, Zn) family of frameworks tested in the previous study were also analyzed using the direct analysis method, though they possess pore sizes of ~1.4 nm.[13-14] In these frameworks, strong binding to the high-density of open metal sites would strongly hinder diffusion, and thus, the relaxation signals would also exhibit a clear distinction between pore-confined and interparticle solvent.

Here, we describe a second analysis method that allows for the analysis of high-porosity, large-pore metal-organic frameworks and therefore expands the utility of the porosity screening

tool. This method accounts for simultaneous relaxation and exchange by using kinetic models to fit the multi-exponential relaxation decays. The fitting results reveal that large-pore frameworks exhibit longer pore relaxation times and faster exchange compared to the frameworks previously tested. Pore volumes derived from these fits correlate strongly with the Langmuir surface area for frameworks up to ~5000 m^2/g, thus allowing for a significant increase in the testing range of the NMR porosity screening tool.

3.3 Experimental Details

All reagents were obtained from commercial vendors and used without further purification. Infrared spectra were obtained on a Perkin-Elmer Spectrum 100 Optica FTIR spectrometer furnished with an attenuated total reflectance accessory. Diffraction data were collected with 0.02˚ steps using a Bruker AXS D8 Advance diffractometer equipped with Cu-Kα radiation (λ = 1.5418 Å), a Göbel mirror, a Lynxeye linear position-sensitive detector, and mounting the following optics: fixed divergence slit (0.6 mm), receiving slit (3 mm), and secondary beam Soller slits (2.5°). The generator was set at 40 kV and 40 mA.

Gas adsorption isotherms were measured using a Micromeritics ASAP 2020 instrument. For standard measurements in ASAP low-pressure glass sample holders, activated samples were transferred under a N_2 atmosphere to preweighed analysis tubes, which were capped with a Transeal. The samples were evacuated on the ASAP until the outgas rate was less than 3 μbar/min. The evacuated analysis tubes containing degassed samples were then carefully transferred to an electronic balance and weighed to determine the mass of sample (typically 100-200 mg). The tube was fitted with an isothermal jacket and transferred back to the analysis port of the gas adsorption instrument. The outgas rate was again confirmed to be less than 3 μbar/min. Langmuir surface areas were determined by measuring N_2 adsorption isotherms in a 77 K liquid N_2 bath and calculated using the Micromeritics software, assuming a value of 16.2 $Å^2$ for the molecular cross-sectional area of N_2.

3.3.1 Synthesis of Sc-MIL-100, Fe-MIL-100, and Al(OH)(bpdc)

The compounds Sc-MIL-100,[71] Fe-MIL-100,[72] and Al(OH)(bpdc)[73] were synthesized by following the published procedures. The successful synthesis and activation of the framework was confirmed by comparing the X-ray powder diffraction pattern and Langmuir surface areas to those previously reported.

3.3.2 Synthesis of MOF-5

The compound MOF-5 was synthesized and activated using a strategy adopted from a previous report.[29] Specifically, H_2bdc (0.66 g, 4.0 mmol), $Zn(NO_3)_2{\cdot}6H_2O$ (3.6 g, 12 mmol), and N,N-diethylformamide (DEF, 100 mL) were combined in a 250-mL Schlenk flask sealed with a rubber septum. The Schlenk flask was heated at 90°C for 24 h, then placed under N_2, and the reaction solvent was removed via cannula and replaced with anhydrous N,N-dimethylformamide (DMF) at room temperature. The DMF was exchanged with fresh, anhydrous DMF two further times. The DMF was then exchanged with anhydrous dichloromethane (DCM) at room temperature. The DCM was exchanged with fresh, anhydrous DCM two further times, then the majority of the DCM was removed via cannula. The resulting clear, cubic crystals were activated by heating at 150°C under vacuum for 24 h. The successful synthesis and activation of the framework was confirmed by comparing the X-ray powder diffraction pattern and Langmuir surface areas to those previously reported.

3.3.3 Synthesis of Co_2(dotpdc)

The compounds 4,4"-dihydroxy(1,1':4',1"-terphenyl)-3,3"-dicarboxylic acid (H_4dotpdc) and Co2(dotpdc) were synthesized by following the published procedure.[74] The successful synthesis and activation of the framework was confirmed by comparing the X-ray powder diffraction pattern and Langmuir surface areas to those previously reported.

3.3.4 Framework Solvent Exchange

Evacuated metal-organic framework samples were imbibed by soaking the framework in DMF overnight. The MOFs were then filtered and dried in a N_2 atmosphere to evaporate excess solvent. Subsequent thermogravimetric analysis (TGA Q50, TA Instruments, New Castle, DE) was used to quantify solvent content of the solvent-filled MOF. Solvent content was determined from the mass loss prior to degradation temperatures for each material. Solvent content was normalized to the dry weight of the MOF sample, and was systematically varied by micropipette addition or thermal evaporation.

3.3.5 NMR Experiments

^{1}H-NMR relaxation was measured using a 13 MHz Aster Enterprises permanent magnet equipped with a homebuilt probe. This probe consisted of a simple solenoid coil with a diameter of ~8 mm wired to tuning and matching capacitors. A Kea II spectrometer was used for pulse generation and signal acquisition, and all pulse programs were written using a Prospa v3.11

software package. Carr-Purcell-Meiboom-Gill (CPMG) pulse sequences were used to measure the T_2 relaxation, while T_2-T_2 relaxation exchange experiments (REXSY) were used to qualitatively identify the presence of exchange.[43, 68-70] All samples were measured at room temperature.

A fast Laplace inversion numerical algorithm from Magritek was used to generate 1D and 2D relaxation distributions,[64] and the kinetic model fits were conducted using a nonlinear least-squares fitting program. To verify the quality of the fit, the p-value of the residuals was calculated, and a criterion of $p<0.01$ was used to reject the fit. In order to overcome local minima randomly selected starting points were used to fit the data, though all starting points eventually converged to the same fitting values. The fits were also rejected if the fitted values, especially the pore-confined relaxation time, exhibited an especially large deviation, indicating that the fit was no longer sensitive to the pore-confined solvent. This situation often occurred at high solvent contents where the signal from the pore-confined solvent was small.

3.4 Results and Discussion

3.4.1 Relaxation Behavior of Large-Pore Frameworks

The relaxation distributions are shown in Figure 3.1 for Al(OH)(bpydc) (MOF-253; $bpydc^{2-}$ = 2,2'-bipyridine-5,5'-dicarboxylate), a high porosity framework (Langmuir surface area = 2250 m^2/g), imbibed with DMF at various solvent contents V_{total}.

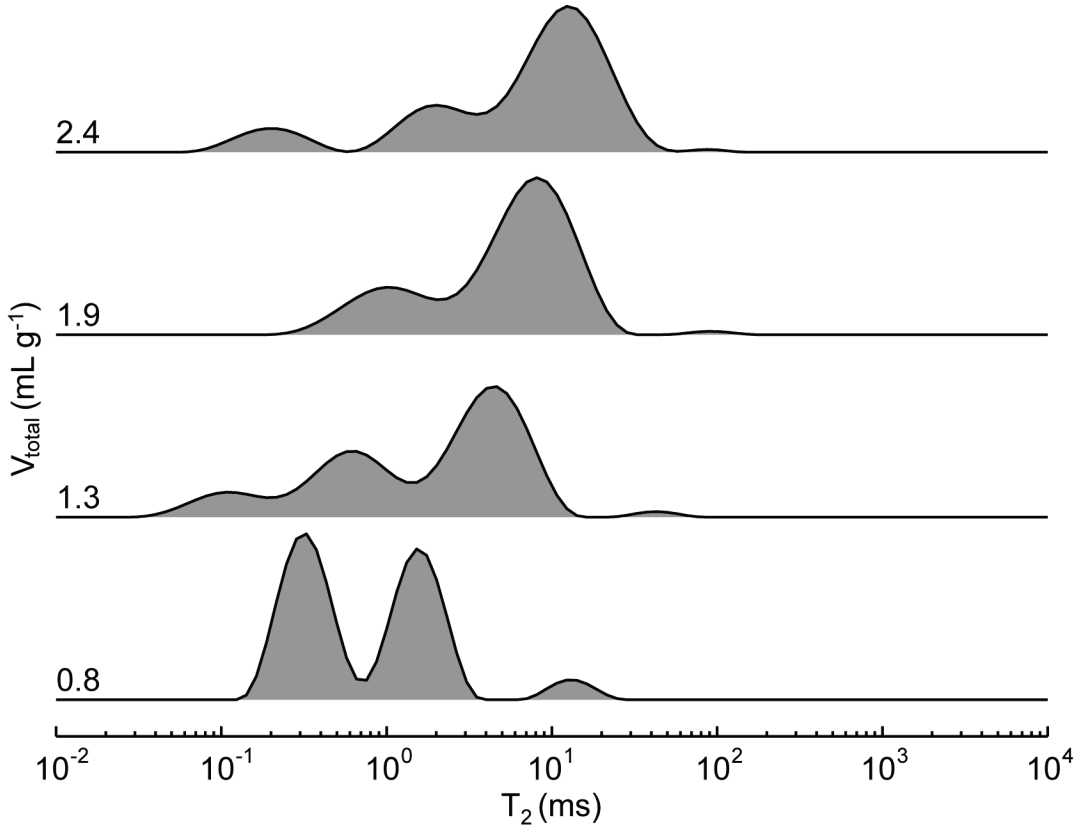

Figure 3.1. Transverse (T_2) relaxation distributions of Al(OH)(bpydc) with various amounts of DMF added. The total intensity at each solvent content is normalized to unity.

These relaxation distributions qualitatively differ from those seen in Chapter 2, with no clear indication of pore-confined and bulk-solvent, especially considering the changes in the relaxation distribution with increasing solvent content. Given the pore volume of Al(OH)(bpydc) (0.89 cm^3/g), full loading of the pore volume with DMF (0.948 g/cm^3) should occur at approximately 0.8 mL/g. Assuming that solvent molecules would preferentially adsorb into the pores first, a single relaxation population representing pore-confined solvent should be observed at these loadings. However, at the lowest solvent loading (0.8 mL/g), three distinct peaks are observed at ~0.3 ms, ~1.5 ms, and ~12 ms, indicating that there are multiple relaxation populations present. As solvent is added, all of the peak areas change, some of the peaks appear to coalesce, and there is a general shift to longer relaxation times. This behavior again contrasts with that seen in small-pore frameworks, where addition of solvent would cause a clearly-separated second relaxation population to appear. This population corresponded to the inter-particle solvent, allowing for

direct porosity analysis. Thus, the divergent relaxation behavior of large-pore frameworks, which is seen in a variety of other tested frameworks (i.e. Sc-MIL-100, Fe-MIL-100, MOF-5, and Co_2(dotpdc), a terphenyl based expanded analogue of Mg_2(dobpdc) featuring coordinatively unsaturated Co^{2+} cation sites[17]), precludes the direct interpretation of the distributions.

3.4.2 T_2-T_2 Relaxation Exchange (REXSY) Experiments and Kinetic Modeling

We performed 2D T_2-T_2 relaxation exchange (REXSY) experiments to investigate the origin of this divergent relaxation behavior, as exchange between relaxation populations can create effects very similar to those seen in Figure 3.1. The relaxation maps produced from the 2D Laplace inversion of the data can help identify the presence of exchange. Although the populations shown in these maps are subject to many of the same effects as those seen in the 1D relaxation distributions, any populations appearing off the diagonal are strong indicators of exchange processes. The T_2-T_2 map for MOF-253 measured at high solvent content (2.8 mL/g) for an exchange time of 10 ms is shown in Figure 3.2.

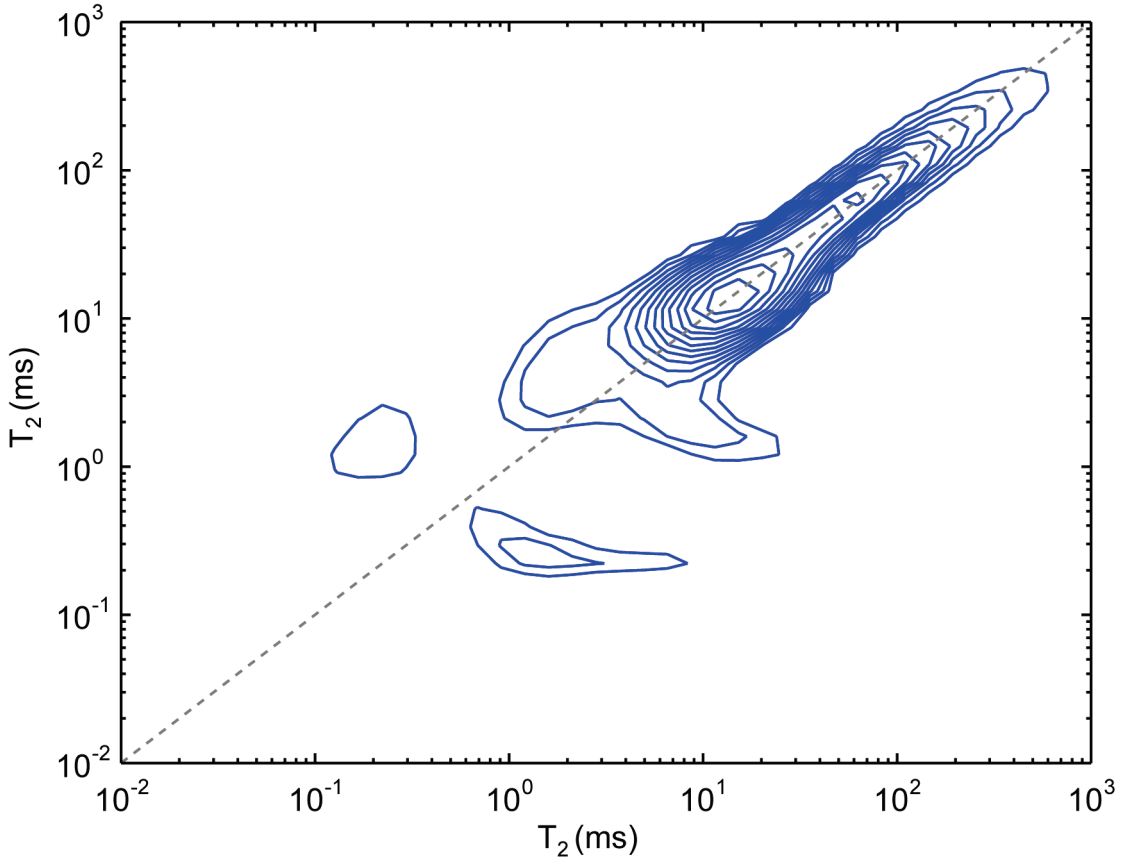

Figure 3.2. Contour plot of the T_2-T_2 relaxation map for Al(OH)(bpydc) at high loading (2.8 mL/g) with an exchange time of 10 ms. The dashed line indicates the parity line ($T_2 = T_2$).

The exchange map qualitatively indicates that exchange is indeed happening at a timescale of $1/k$~10 ms, where k is the exchange rate, as indicated by the presence of populations off the diagonal line. This implies that the exchange processes occur at a rate comparable to the relaxation rate, a situation where the relaxation distributions are strongly affected by the exchange processes. Though exchange processes would skew the peak areas and positions, the exchange peaks suggest the presence of three populations at roughly distinguishable relaxation times: short (~0.4 ms), intermediate (~4 ms), and long (>10 ms). Furthermore, exchange peaks appear for exchange between the short and intermediate relaxation populations as well as between the intermediate and long relaxation populations, but not between the short and long relaxation populations. In our previous work, we identified the short, intermediate, and long relaxation populations as the pore-confined, interfacial, and inter-particle solvent, respectively.

Since the pore-confined solvent and the inter-particle solvent must exchange through the interfacial layer outside the porous particles, the exchange peaks suggest that the three populations seen in the T_2-T_2 map can also be assigned as before. Finally, these exchange experiments allow us to speculate on the pore diffusion coefficient. The solvent diffusion coefficient within the framework pores should be greatly decreased from the neat solvent due to the effect of pore confinement, and thus, the exchange between pore-confined and interfacial solvent would be governed by the rate-limiting pore diffusion process. As a first assumption we assume that the diffusion length must be roughly on the order of the particle size, which results in significant mixing of populations and in skewed relaxation distributions. Given a particle size on the order of 1 μm and an exchange time of 1-10 ms, the pore diffusion coefficient would be on the order of 10^{-10} to 10^{-11} m^2/s. Though self-diffusion coefficient measurements for large, polar molecules, such as DMF, in microporous media are largely unavailable, the diffusion coefficients estimated here are not unreasonable given the literature available for alcohol diffusion in faujasite-type zeolites and zeolitic imidazolate frameworks (ZIFs).[75-76]

In order to quantify the relaxation and exchange processes between the pore-confined (A), interfacial (B), and inter-particle (C) populations, we used a three-site kinetic model to fit the 1D relaxation data.

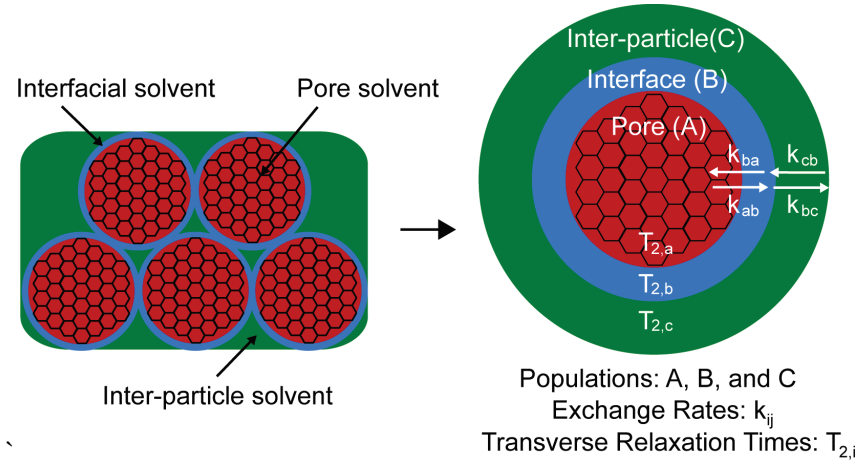

Figure 3.3. Schematic of three-site kinetic model indicating simultaneous relaxation and exchange between pore, interfacial, and inter-particle solvent.

$$\frac{\partial M_a}{\partial t} = -r_a M_a - k_{ab} M_a + k_{ba} M_b \tag{3.1}$$

$$\frac{\partial M_b}{\partial t} = -r_b M_b - k_{ba} M_b - k_{bc} M_b + k_{ab} M_a + k_{cb} M_c \quad 3.2$$

$$\frac{\partial M_c}{\partial t} = -r_c M_c - k_{cb} M_c + k_{bc} M_b \quad 3.3$$

$$M_{a,b,c}(t=0) = M^0_{a,b,c} \quad 3.4$$

Here, M_i represents the magnetization of each population, r_a is the inherent relaxation rate of each population, and k_{ij} is the exchange rate of population i to population j. Note that $k_{ac}=k_{ca}= 0$, indicating that the pore-confined and inter-particle populations do not exchange directly. Due to mass balance, only two independent exchange coefficients remain, and the rates of A-B exchange and B-C exchange can be described by a single variable each. Also, though the 2D relaxation data could also be fitted using this model, the 1D fit yielded nearly identical results, rendering the 2D fits superfluous. The pore volume was taken as the initial magnetization of the pore-confined solvent (M_a^0). The model fits for Al(OH)(bpydc) are shown below.

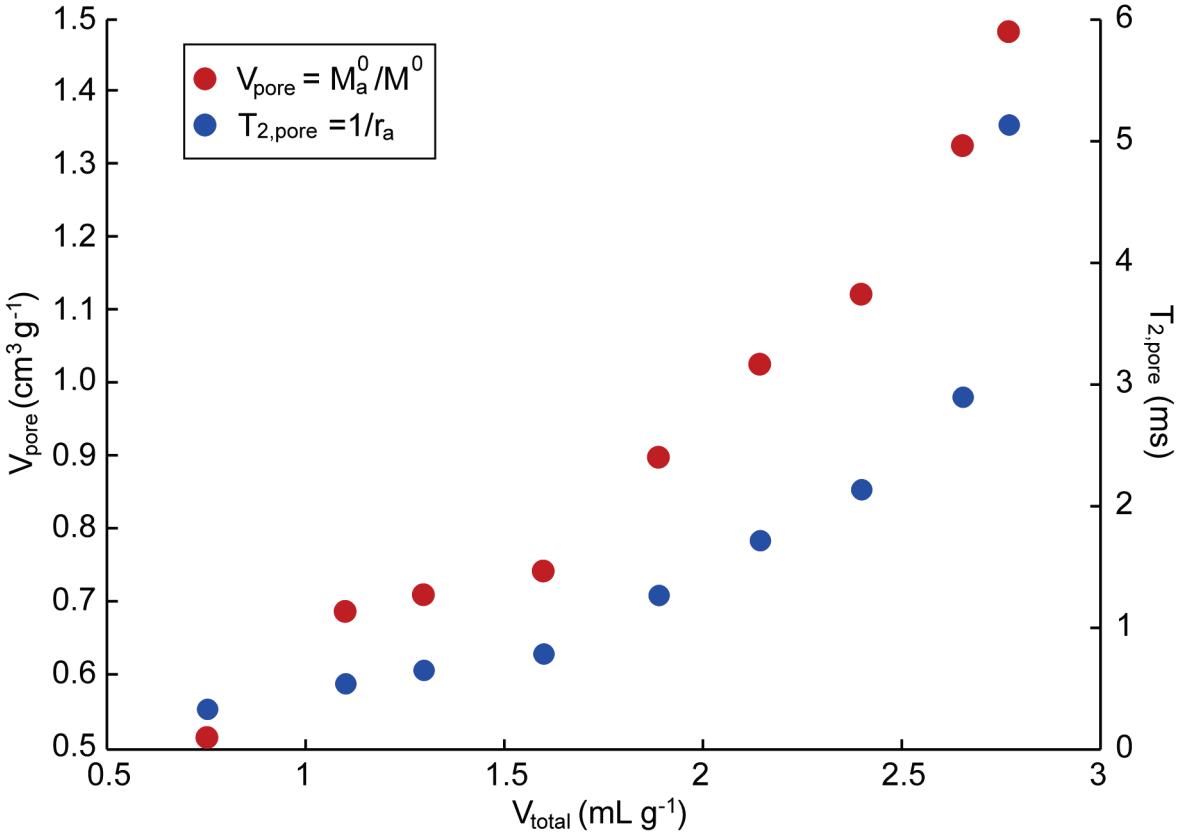

Figure 3.4. Pore volume (M_a^0) and $T_{2,pore}$ ($1/r_a$) resulting from the fits of the three-site kinetic model to the relaxation data for Al(OH)(bpydc). Note that the points at the highest solvent content were disregarded due to poor fitting ($p < 0.01$) and an incommensurate increase in both values.

Figure 3.4 indicates that the pore volume and pore relaxation time $T_{2,pore} = 1/r_a$ increase with increasing solvent content, which suggests that the pores are filling as solvent is added. In frameworks with pore sizes much larger than the solvent molecule diameter, the framework walls are fully covered by solvent molecules at high adsorbate loadings, and adsorption of any additional solvent molecules would be akin to a condensation process. In this case, adsorption in the inter-particle space and in the framework pores would exhibit similar heats of adsorption (i.e. BET-like adsorption), resulting in growth of both the pore-confined and inter-particle solvent population with increasing solvent content. This effect was unanticipated and would also result in differing relaxation distributions when compared to that for small-pore frameworks. Also, for

all solvent contents, the exchange time between the pore-confined and interfacial solvent ($1/k_a$) is on the order of 1-10 ms, with the exchange time increasing for increasing solvent contents. These values agree with those estimated from the qualitative analysis of the T_2-T_2 map. Note that at the highest solvent content, both values display an incommensurately large increase in values, an artifact indicating that the least-squares algorithm is no longer sensitive to the proportionally small signal stemming from the pore-confined solvent. The resulting fits from these data were disregarded. Since sensitivity to the pore-confined solvent population is lost at higher solvent contents, the pore volume at the highest solvent content with an acceptable fit was taken as an estimate of the actual pore volume. This algorithm was applied to the relaxation data for four additional large-pore, high-porosity frameworks (Sc-MIL-100, Fe-MIL-100, Co_2(dotpdc), and MOF-5). The relaxation data from Chapter 2 was also analyzed using a two-site kinetics model for comparison; the choice of a two-site model rather than a three-site model stemmed from the relaxation data exhibiting largely bimodal behavior. The model-derived pore volume (see Figure 3.5) agrees well with the Langmuir surface areas for both the two- and three-site model fits, indicating that the model is largely accounting for the physics of relaxation and exchange in large-pore frameworks. Also, the pore volumes derived from the two-site kinetics model fit to the previously obtained relaxation data are nearly equal to those calculated from the original analysis of the relaxation distributions, further confirming the validity of this new analysis method. By using this method, frameworks with higher surface-areas can be characterized, thereby improving the utility of an NMR relaxometry-based porosity screening tool.

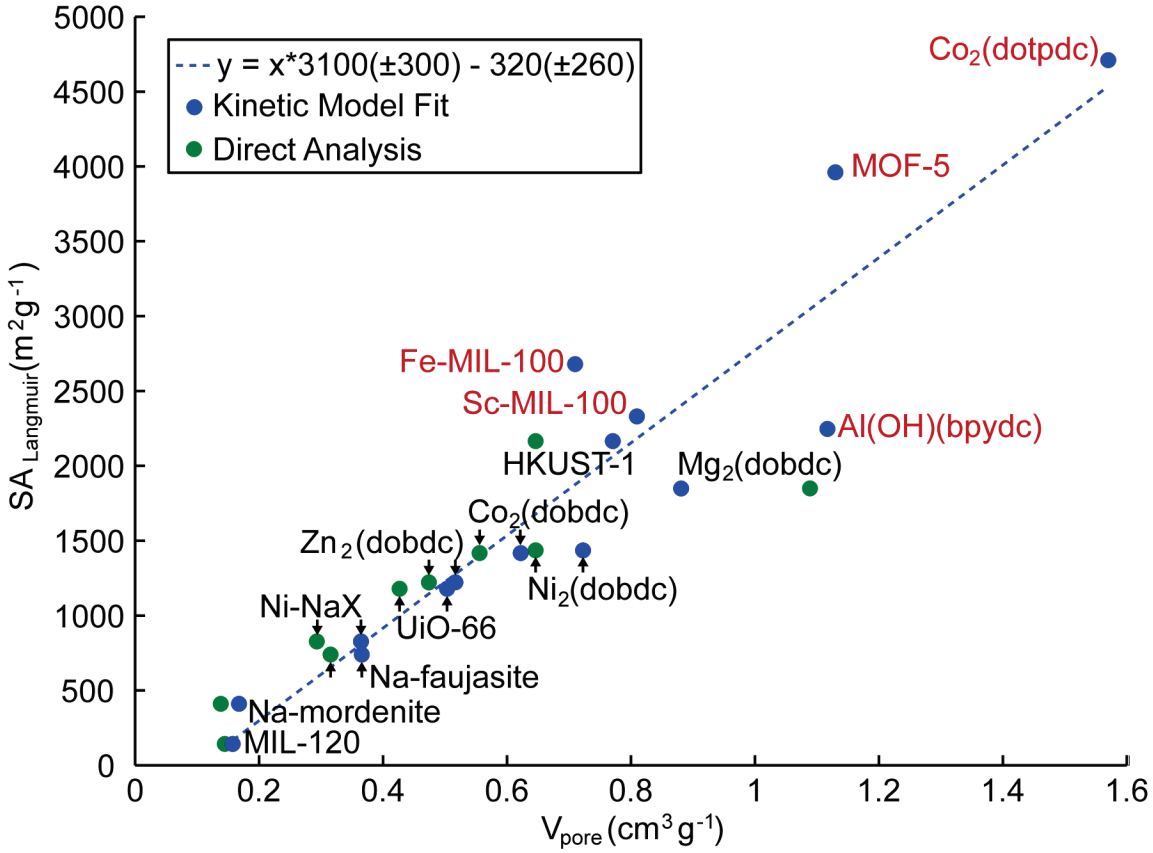

Figure 3.5. Correlation of Langmuir surface area ($SA_{Langmuir}$) to the model-derived pore volume (V_{pore}). Dashed lines indicate the linear fit to the kinetic model data. Note that the labels in red indicate the three-site model fits for data obtained on the homogeneous-field permanent magnet, and the labels in black indicate the two-site model fits for previously obtained data from the single-sided NMR-MOUSE. The pore volumes derived from the direct analysis method of the NMR-MOUSE data are shown in green. The Langmuir surface areas for the frameworks used in the three-site model fits were determined from 77 K N_2 adsorption isotherms.

3.5 Conclusions

In this study, we describe a new analysis method to measure the surface area of high-porosity, large-pore metal-organic frameworks using NMR relaxometry. In these frameworks, the relaxation distributions do not reflect the actual porosity due to the diffusional exchange occurring on the timescale of relaxation. We applied kinetic models to account for simultaneous relaxation an exchange and derived a pore volume that correlates well the surface area, though

further work is needed to investigate the behavior of the model fits with increasing solvent content. Nevertheless, the ability to characterize frameworks with large surface areas greatly improves the utility of the relaxometry-based screening tool.

3.6 Acknowledgements

The material herein was previously published[77] with coauthors Jarad A. Mason, Eric D. Bloch, David Gygi, Jeffrey R. Long, and Jeffrey A. Reimer. This work was supported by the U.S. Department of Energy, Advanced Research Projects Agency - Energy (ARPA-E) under Grant No. DE- AR0000103. The authors acknowledge Dr. Kenji Sumida, and Ms. Mary Anne Manumpil for assistance with sample preparation. Jarad A. Mason acknowledges a graduate fellowship through the National Science Foundation.

Chapter 4

Vapor-Liquid Coexistence in a Microporous Metal-Organic Framework

4.1 Abstract

Here, we describe detailed Monte Carlo (MC) simulations and nuclear magnetic resonance (NMR) relaxation experiments that establish a novel type of vapor-liquid coexistence for benzene and xylenes in IRMOF-type structures. Droplets of a high-density, liquid-like phase form across multiple unit cells, and these droplets are surrounded by a low-density, vapor-like phase. This type of condensation is distinct from capillary condensation in a single pore, and we propose the term "framework-inhibited condensation" for this phenomenon. The tunability of metal-organic framework structures presents a unique opportunity to control phase equilibria in porous materials for fundamental studies and practical applications.

4.2 Introduction

The behavior of adsorbed molecules inside porous materials governs the material's utility, and thus, understanding guest behavior is of utmost importance for the development of useful industrial porous materials. Gas adsorption isotherms are frequently used to characterize guest behavior as a function of pressure or loading. These adsorption isotherms may signal phase transitions, which are essential in defining adsorbate behavior, by displaying steps or kinks that are often accompanied by hysteresis as well.[78] Phase transitions in microporous materials were once not thought possible because the molecular-sized pores caused adsorbates to behave like a one-dimensional fluid.[79] Instead, steps in the adsorption isotherms were usually attributed to capillary condensation in crystal defects until computer simulations found evidence for phase transitions of the solid-fluid type in the zeolite silicalite[80] and of the vapor-liquid type in the aluminophosphate $AlPO_4$-5[81-82] both of which explained the shapes of the experimental

adsorption isotherms. More recently, steps in the adsorption isotherms of metal-organic frameworks (MOFs) have been attributed to transitions in the framework structures themselves through mechanisms such as breathing[18] or gate-opening.[83] However, steps in the experimental[84-85] and simulated[84, 86-89] adsorption isotherms of the isoreticular MOF (IRMOF) series cannot be explained by changes in the host structure because the framework is considered rigid.[8] In addition to these anomalous isotherms, thermodesorption profiles have been observed in IRMOF-1 (MOF-5) that also demonstrate adsorption-desorption hysteresis.[90] Previous nuclear magnetic resonance (NMR) experiments and molecular dynamics (MD) simulations suggested that aggregation or clustering of the benzene molecules may occur between IRMOF-1 pores, a phenomenon that would explain these anomalous behaviors.[91-92] Further exploration of such a phenomenon remains absent from the literature. Here, we describe detailed Monte Carlo (MC) simulations and nuclear magnetic resonance (NMR) relaxation experiments that establish a novel type of vapor-liquid coexistence that explains the behavior reported in the IRMOF series. The ability to precisely tune the pore structure and chemistry affords a unique opportunity to control the phase behavior in this new class of porous materials. Such control not only enables more fundamental explorations of confined systems but also allows for more effective utilization of phase behavior in application.

4.3 Experimental and Computational Details

4.3.1 Canonical MC

The liquid-vapor interface was minimized by choosing a high aspect ratio simulation box in which a single liquid slab of a density found from an earlier simulation was placed. This caused the two phases to form only two interfaces, each orthogonal to the elongated dimension. It was verified that this method did not disrupt the density measurements by comparing the obtained density profiles to simulations started without an initial configuration of adsorbate molecules. Time-averaged density profiles were calculated using 10 bins per cage in the elongated dimension and 1 bin per cage in each of the cross-sectional dimensions in order to examine the effects of the two different types of cages. By integrating the liquid or vapor parts of the averaged density profiles (away from the interface) over an integer number of unit cells in the elongated dimension, densities of the two phases were obtained at various temperatures and arranged into phase diagrams. Critical temperatures and densities were obtained by fitting to the density scaling law (with $\beta = 0.32$) and the law of rectilinear diameters.[93] Data were collected every 10 cycles over at least 200,000 cycles following at least 200,000 equilibration cycles. During the data collection cycles it was verified that while the phase interfaces sometimes moved in the

elongated direction, the length over which the bulk densities were sampled remained in a single phase. Drifting interfaces in these simulations were accommodated by shifting the simulation box to keep the center of the liquid phase in the center of the simulation box. The framework was assumed to be rigid and the experimental structures were used.[3] IRMOF-1 and IRMOF-7 simulations used a simulation box of 2 by 2 by 10 unit cells. IRMOF-10 simulations used a simulation box of 1 by 1 by 8 unit cells. IRMOF-14 simulations used a simulation box of 1 by 1 by 7 unit cells. IRMOF-16 simulations used a simulation box of 1 by 1 by 10 unit cells. It was ensured that homogeneous bulk behavior of both liquid and vapor phases were observed to span at least 2 unit cells in the elongated dimension before using those unit cells for bulk density data.

4.3.2 Grand Canonical MC

Data were collected every 100 cycles over at least 50,000 cycles following at least 50,000 equilibration cycles. The IRMOF-1 simulation box consisted of 2 by 2 by 2 unit cells.

4.3.3 Force Field

The Lennard-Jones potential was used to describe dispersive interactions with Universal Force Field[94-95] parameters used for the framework atoms and TraPPE[96] model parameters for the adsorbate molecules. Lorentz-Berthelot mixing rules were used with a 14.0 Å truncation and tail-corrections. As the TraPPE models do not have partial charges, Coulombic interactions were not used. Unlike what was found in past studies concerning carbon dioxide in IRMOF-1,[84] these Coulombic interactions were not necessary to observe stepped isotherms. The potentials were pretabulated and interpolated over a 0.1 Å grid.

4.3.4 Synthesis of MOF-5

All reagents were obtained from commercial vendors and used without further purification. The compound MOF-5 was synthesized and activated using a strategy adopted from a previous report.[29] Specifically, terephthalic acid (0.66 g, 4.0 mmol), $Zn(NO_3)_2 \cdot 6H_2O$ (3.6 g, 12 mmol), and N,N-diethylformamide (DEF, 100 mL) were combined in a 250-mL glass jar sealed with a Telfon-lined lid. The jar was heated at 90 °C for 24 h then placed under N_2, and the reaction solvent was decanted and replaced with anhydrous N,N-dimethylformamide (DMF) at room temperature. The DMF was exchanged with fresh, anhydrous DMF seven further times. The DMF was decanted from the glass jar containing the MOF-5 crystals, and the residual DMF transferred along with the crystals was then exchanged with anhydrous dichloromethane (DCM) at room temperature. The DCM was exchanged with fresh, anhydrous

DCM seven further times, and then the majority of the DCM was removed via cannula. The resulting clear, cubic crystals with diameters of >100 μm were activated by heating at 150°C under vacuum for 24 h. The successful synthesis and activation of the framework was confirmed by comparing the X-ray powder diffraction pattern and Langmuir surface areas to those previously reported.[27] The measured Langmuir surface area was 5370 m^2/g, indicating a pristine MOF-5 framework.

4.3.5 Preparation of Benzene and *p*-Xylene-loaded MOF-5

Approximately 10-15 mg of MOF-5 crystals containing residual DCM were transferred to a flame-dried 5 mm NMR tube. The tube was then affixed to a Sigma-Aldrich NMR tube filling manifold, and the MOF-5 was activated by heating at 130°C under high vacuum (<1 x 10^{-5} torr) for 8 hours. To determine the exact mass of MOF-5, the sample was backfilled with dry N_2, capped, and weighed. The MOF-5 was then re-evacuated under high vacuum for an hour to remove adsorbed N_2. After this final evacuation, the NMR tube was isolated from vacuum with the manifold valve, and the portion of the tube containing the MOF-5 crystals was placed in liquid nitrogen.

Separately, *p*-xylene and benzene in a flame-dried round-bottom flask with a valve and septa were purified by 3-5 freeze-pump-thaw cycles to <5 x 10^{-3} Torr to remove any dissolved gases. A 10 μL syringe was used to transfer the degassed solvent into the NMR tube, and the solvent was condensed into the tube using liquid N_2. The sample containing MOF-5 and solvent was then flame-sealed. To quantify the amount of solvent added, a careful calibration between proton number and signal intensity was conducted using known quantities of dimethyl sulfoxide. The signal intensity of the solvent-loaded MOF-5 samples was then used to calculate the solvent content. This solvent content was verified by subsequent thermogravimetric analysis. All samples were equilibrated at room temperature for at least 24 hours before testing, which was necessary to stabilize NMR behavior.

4.3.6 NMR Experiments

^{1}H-NMR relaxation measurements were performed on a Bruker 7.05 Tesla magnet with a Tecmag Discovery spectrometer and a Doty Scientific 5-mm triple-resonance XC MAS probe. Carr-Purcell-Meiboom-Gill (CPMG) pulse sequences[60-61] modified with DEPTH background-cancelling excitation pulses[97] were used to measure the T_2 relaxation, while T_2-T_2 relaxation exchange experiments (REXSY) were used to qualitatively identify the presence of multiple phases (see Appendix A for more details).[43, 46-47, 98] For the latter experiments, the

number of echoes in the first CPMG sections was varied while keeping the echo time constant (0.2 ms). The number of echoes of the first CPMG was varied logarithmically with 20-25 2D points. For both the CPMG and the T_2-T_2 experiments, the π pulse lengths were ~20 μs. The temperatures of the NMR experiments were modulated by a Doty Scientific temperature controller designed for use with the XC probe. The amount of benzene and *p*-xylene desorbed when varying the temperature was estimated using the simulated adsorption isotherms, and in all cases, the proportion of adsorbed molecules greatly exceeds the proportion found in the head space of the sample (>97% even at 115°C). Finally, a fast Laplace inversion numerical algorithm (Magritek, New Zealand) was used to generate 1D and 2D relaxation distributions.[64] An optimal smoothing parameter was chosen using the method of the L-curve.[99]

4.4 Results and Discussion

4.4.1 Monte Carlo Simulation of Benzene in IRMOF-1

We conducted Canonical MC simulations[93] of benzene in IRMOF-1 starting with a random initial configuration of adsorbate molecules, and we observed the formation of a high-density liquid-like droplet spanning multiple cages, surrounded by a low-density vapor-like phase (see Figure 4.1).

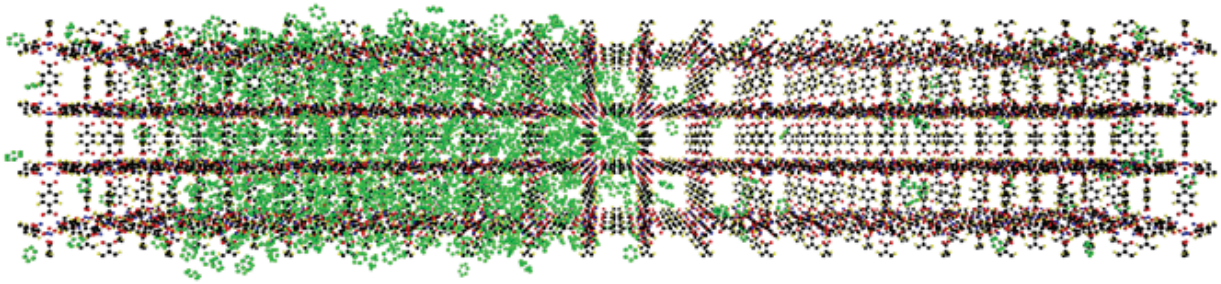

Figure 4.1. Snapshot of benzene in IRMOF-1 with a loading of 26.8 molecules per unit cell at 300 K. Note the condensation of benzene molecules over multiple unit cells.

By selecting a high aspect ratio simulation box, the liquid-vapor interface was minimized, which allowed us to calculate bulk densities of the two phases away from the interface. From this, we constructed a phase diagram in the temperature-density plane that demonstrates a decrease in the critical temperature from benzene's bulk value (see Figure 4.2). The densities on the phase envelope are consistent with the hysteretic loadings found from simulated adsorption isotherms (see Appendix I.1).

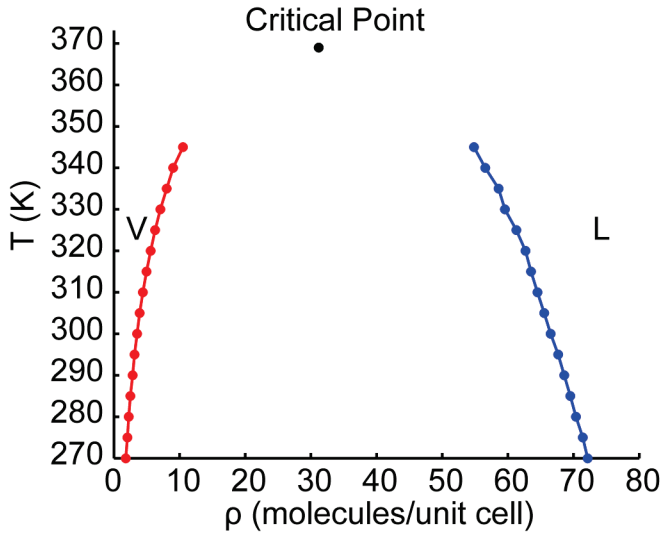

Figure 4.2. Density-temperature phase diagram for benzene in IRMOF-1. Coexistence densities for the vapor (red) and liquid (blue) as well as the extrapolated critical point are shown. The critical temperature of neat benzene is 562K.

This newly observed condensation phenomenon is distinct from capillary condensation in that capillary condensation occurs within a single pore of a material and results in the formation of a meniscus. Clearly, the concept of a meniscus becomes irrelevant at the molecular scale, but more importantly, the phase behavior of benzene in IRMOF-1 extends throughout many unit cells in the microporous framework and is more similar to the bulk vapor-liquid coexistence that occurs in the absence of a porous material. As the framework lowers the coordination number of the fluid molecules[100] and decreases the critical temperature as predicted by mean field theory,[101] we propose the term "framework-inhibited condensation" for this phenomenon.

4.4.2 Variable Temperature Relaxation Experiments of Benzene in IRMOF-1

Vapor-liquid coexistence in IRMOF-1 creates distinct magnetic environments that are distinguishable using NMR relaxation measurements. We measured the distribution of T_2 relaxation times using Carr Purcell Meiboom Gill (CPMG) pulse experiments[60-61] combined with a Laplace inversion numerical analysis algorithm.[64] Figure 4.3 illustrates the distribution of T_2 components obtained from benzene in IRMOF-1 (9 ± 1 molecules of benzene per unit cell) for three temperatures: 295K, 343K, and 388 K. The relaxation distribution at room temperature

(295K) displays a dominant peak at intermediate relaxation times (~120 ms) as well as a small peak at long relaxation times (~870 ms). (The small peak at ~5 ms is discussed later in this section).

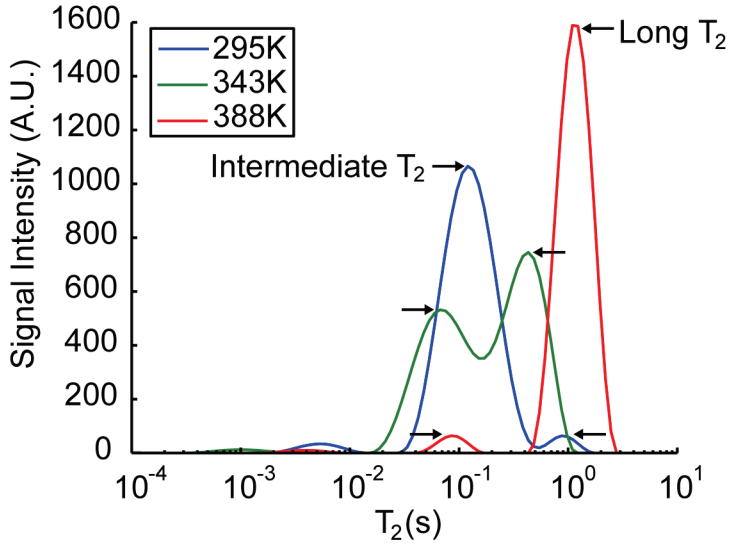

Figure 4.3. T_2 relaxation distributions of benzene in IRMOF-1 at a loading of 9 ± 1 molecules of benzene per unit cell. Distributions are shown temperatures of 295K, 343K, and 388K, with right- and left-facing arrows indicating the intermediate and long T_2 populations, respectively.

When IRMOF-1 is loaded with 9 molecules of benzene per unit cell, the simulated vapor-liquid coexistence curve (Figure 4.2) indicates that at room temperature, the majority of benzene molecules (~70%) reside in the liquid-like phase while the majority of the crystal volume (~90%) will be occupied by the vapor-like phase. We therefore conclude that the dominant relaxation peak at ~120 ms represents benzene molecules in the liquid phase. As the temperature increases, this peak decreases in size while the peak centered at long-T_2 values increases in size. At 343K, the number of molecules associated with each relaxation peak is roughly equal, whereas at 388K the long-T_2 peak dominates. We therefore conclude that the long-T_2 signal emanates from benzene molecules in the vapor-like phase, and at 343K the intermediate and long T_2 peaks represent the liquid and vapor phases, respectively. It is worth noting that both peaks at 343K exhibit decreased relaxation times relative to those observed at 295K, a phenomenon that is still not fully understood (see Appendix I.3). Nevertheless, the changes in peak intensity are

commensurate with the qualitative trend of increasing vapor density and decreasing liquid density with increasing temperature as predicted by our MC simulations.

4.4.3 T_2-T_2 Relaxation Exchange Experiments of Benzene in IRMOF-1

Two-dimensional T_2-T_2 relaxation exchange experiments were performed to further confirm that the peaks in the relaxation distributions in Figure 4.3 represent different phases. These experiments can detect molecules that diffuse between spatially distinct regions characterized by differing T_2 relaxation times during a prescribed exchange time (t_{exch}). Figure 4.4 shows the T_2-T_2 exchange plots for t_{exch} = 500 ms at 295, 343K, and 388K.

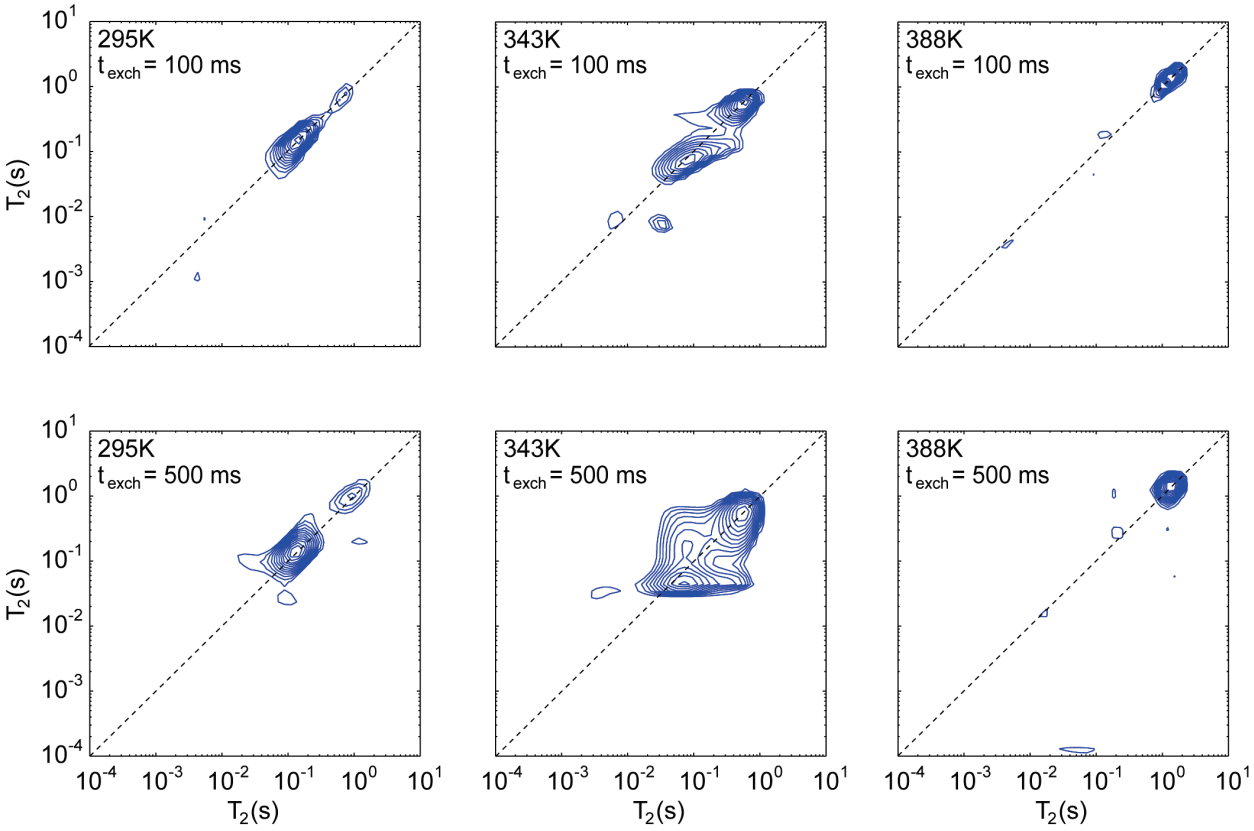

Figure 4.4. T_2-T_2 relaxation exchange distributions of benzene in IRMOF-1 at a loading of 9 ± 1 molecules of benzene per unit cell. Distributions are shown for t_{exch} = 100 and 500 ms at 295K, 343K, and 388K. All distributions are obtained using t_{echo} = 0.2 ms. Peaks that are centered symmetrically on either side of the diagonal represent exchanging liquid molecules.

Peaks centered on the diagonal represent benzene molecules that have not exchanged during t_{exch}, whereas peaks that are centered symmetrically on either side of the diagonal are associated with molecules that have exchanged. At all temperatures, exchange peaks are observed, though exchange is most prominent at 343K. This confirms that the molecules belonging to the intermediate and long-T_2 populations are exchanging within a timescale of t_{exch}~100 ms. Given the diffusion coefficient of benzene in IRMOF-1 at 343K (D_{self} ~ 1 x 10^{-8} m^2/s),[91] we estimate a diffusion length $(D_{self}\ t_{exch})^{1/2}$ consistent with an exchange length scale of ~10^{-5} m. Exchange between different relaxation populations on this micron length scale strongly suggests that the peaks in our relaxation distribution are distinct phases.

4.4.4 Internal Field Gradients Induced by Vapor-Liquid Interfaces

Vapor-liquid coexistence creates interfaces over approximately micron length scales that should result in magnetic field gradients that also contribute to T_2.[45, 49] These field gradients (i.e. internal field gradients) arise from the contrast in the volume magnetic susceptibility (χ) between the vapor-like and the liquid-like phases. Samples possessing vapor-liquid equilibria placed in an external magnetic field therefore experience a field gradient at the vapor-liquid interface. The CPMG experiment, which measures the gradient-modulated T_2, consists of an excitation pulse followed by a series of refocusing pulses. The refocusing pulses are separated by a time period (t_{echo}) generally on the order of 0.1-1 ms that modulates the effect of field gradients on T_2. Molecular self-diffusion (D_{self}) through the field gradient will decrease T_2, and the T_2 in the presence of a gradient decreases with increasing t_{echo} and increasing gradient strength (g) (see Equation 4.3 below). Though it is difficult to rigorously characterize the internal field gradient, an upper limit on the strength of the internal field gradient can be estimated.[49]

$$g_{max} = \left(\frac{\gamma}{D_{self}}\right)^{1/2} (\Delta\chi B_0)^{3/2} \qquad 4.1$$

The maximum gradient strength (g_{max}) increases as the difference in volume magnetic susceptibility ($\Delta\chi$) and the applied static magnetic field (B_0) increase. Note that g_{max} also depends on the self-diffusion coefficient of the guest molecules (D_{self}). This dependence results from diffusional averaging of magnetic field inhomogeneities. The critical length scale (l_g) for observing the effect of field gradients, called the dephasing length, can be estimated from g_{max}[49]

$$l_g = \frac{\Delta\chi B_0}{g_{max}} = \left(\frac{D_{self}}{\gamma \Delta\chi B_0}\right)^{1/2} \quad 4.2$$

where γ is the nuclear gyromagnetic ratio. Thus, any spatial variations in the magnetic field occurring on a length scale smaller than l_g will be averaged by diffusion, resulting in a weak effective gradient that does not greatly affect T_2. Though the internal gradient strength, and therefore the dephasing length, is obviously spatially variant, Equations 4.1 and 4.2 allow for general analysis without requiring detailed knowledge of the internal field gradient. In general, the gradient strength increases with proximity to the interface.[102]

The length scale for molecular diffusion during the CPMG pulse sequence ($l_D = (D_{self}\, t_{echo})^{1/2}$) also plays a key role in determining the relaxation behavior. If $l_D << l_g$, then the T_2 induced by diffusion through field gradients ($T_{2,g}$) can be calculated.[49]

$$\frac{1}{T_{2,g}} = \frac{D_{self}\gamma^2 g^2 t_{echo}^2}{12} \quad 4.3$$

In the presence of strong gradients and long diffusion lengths ($l_D >> l_g$), $T_{2,g}$ does not depend on t_{echo}, though this situation is rarely achieved experimentally.[45] Note also that spatial variations in the field gradient larger than l_D would result in multiple relaxation times corresponding to areas with different gradient strengths.[45]

By modulating a time period parameter (t_{echo}) in the CPMG experiment we assess the effect of internal gradients on T_2. Figure 4.5 below illustrates the T_2 distributions with varying t_{echo} for 295K and 388K. As t_{echo} increases, the entire distribution shifts to shorter relaxation times, indicating the presence of strong internal field gradients. A further indication of the presence of these gradients is the decrease in total signal intensity with increasing t_{echo}. This decrease indicates that some proportion of benzene molecules experience such strong gradients that they become undetectable due to substantially shortened T_2; thus at long t_{echo} a proportion of the signal attenuates before it can be detected. Notably, the small short T_2 component at ~5 ms does not appear to change position with t_{echo}, and at long t_{echo} this component is obscured by the shift in the relaxation distribution. This peak is likely signal from benzene molecules that experience very strong gradients ($l_g << l_D$), and thus, T_2 does not depend on t_{echo}. Since this peak is small and does not affect the conclusions of our analysis, it will not be discussed further.

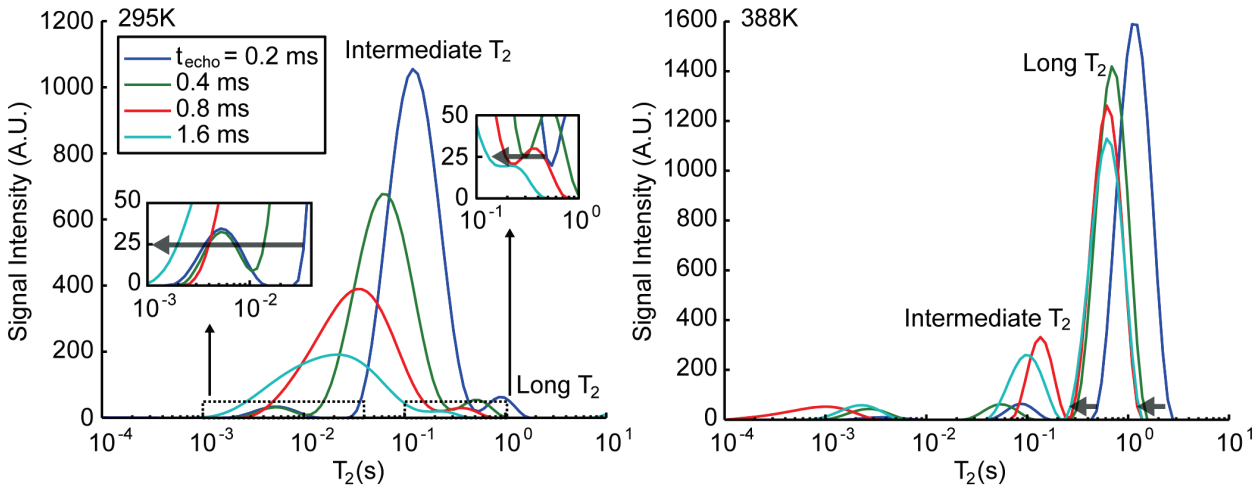

Figure 4.5. T_2 relaxation distributions of benzene in MOF-5 at a loading of 9 ± 1 molecules of benzene per unit cell of MOF-5. Distributions were obtained via Laplace inversion of CPMG experiments with varying t_{echo} at 295K (left) and 388K (right). The insets highlight the shifts in the edges of the relaxation distribution, while grey arrows in the both plots indicate the magnitude of these shifts. For relaxation distributions at 70°C, see Figure I.8.

The presence of internal field gradients provides additional evidence for vapor-liquid coexistence and that these field gradients arise from the vapor-liquid interface rather than the framework-guest interface. Given an estimate of the volume magnetic susceptibility of liquid benzene ($\Delta\chi \approx \chi_{liquid}$ = 6.4 x 10^{-7}), the dephasing length l_g is on the order of 10^{-6} m, about three orders of magnitude larger than the MOF pore size (1.4 nm). This eliminates the guest-framework interface as a source of field gradients because gradients induced by this interface would be averaged by diffusion. Thus, the presence of a vapor-liquid interface provides the most logical source of internal field gradients.

The relaxation distribution at 295K also broadens asymmetrically as it shifts to shorter relaxation times. The short-T_2 edge of the intermediate peak (~120 ms) representing liquid benzene molecules shifts more (~30 ms to 1 ms, a factor of 30) between t_{echo} = 0.2 ms and t_{echo} = 1.6 ms than the long-T_2 edge (~550 ms to ~170 s, a factor of 5), indicating that the gradient is not homogeneous. The benzene molecules at shorter T_2 are subject to stronger gradients, suggesting proximity of these components to the droplet interface. Conversely the molecules exhibiting longer T_2 are farther from the interface; this population likely represents liquid-phase

benzene molecules located near the center of a liquid droplet (the "bulk") that experiences the weaker gradients. Note that the small, long T_2 peak at ~870 ms (t_{echo} = 0.2 ms) representing the vapor phase also exhibits a weak shift with varying t_{echo}. Since the majority of the vapor phase would, on average, be located away from an interface due to its large volume fraction, the vapor phase would experience weaker gradients as well. Interestingly, the relaxation rates ($1/T_2$) of the long and intermediate peaks appear to vary linearly with t_{echo}, a situation that deviates from the normal quadratic dependence found for CPMG experiments (Equation 1). This linear dependence has been previously observed[103] and indicates that l_D and l_g are of comparable orders of magnitude,[104] which agrees with the length scales for our system.

The behavior of T_2 with respect to t_{echo} at 388K also supports the presence of vapor-liquid coexistence. Figure 4.5 shows the relaxation distributions at 388K, a temperature that is above the vapor-liquid critical temperature (T_c) predicted from the MC simulations. The relaxation distribution again shifts to shorter T_2 with increasing t_{echo}, but now the long-T_2 peak position shifts less strongly, as can be seen from the grey arrows. Furthermore, the total signal intensity of the relaxation distributions remains relatively constant as a function of t_{echo}. Both of these observations indicate that the internal gradient strength has decreased. A weaker gradient likely results from an increase in D_{self} as well as a decrease in $\Delta\chi$. Since the liquid and vapor densities converge with increasing temperature, $\Delta\chi$ would be expected to decrease with increasing temperature, and at temperature above the critical point, $\Delta\chi$ should equal zero due to the presence of a single phase. Thus, the presence of a field gradient at 388K indicates that sample is likely below the estimated critical point, indicating an underestimation of the T_c by MC simulations. An alternate explanation would be that density fluctuations associated with a state near the critical point could also create internal field gradients. Finally, the long-T_2 peak shifts symmetrically with increasing t_{echo}, indicating greater spatial homogeneity of the internal field gradient. A small intermediate T_2 peak observed at 388K (~80 ms for t_{echo} = 0.2 ms) also increases in size as t_{echo} increases. The position of this peak does not exhibit any consistent trend, however. We surmise that this peak is likely to be benzene molecules near the interfaces, and that increasing t_{echo} increases l_D, and thus, increases the number of molecules interacting with the interface, explaining the increase in the peak amplitude.

4.4.5 Critical Behavior of Benzene and Xylenes in IRMOF-type Frameworks

Similar NMR relaxation measurements were obtained with *p*-xylene, and similar simulation results were obtained for all three isomers of xylene (Appendix I.1), indicating that vapor-liquid coexistence is general for at least benzene and xylenes. In addition, theoretical phase diagrams were obtained for several IRMOF frameworks, demonstrating control over the vapor-

liquid coexistence via framework modification. As the IRMOF series increases in pore size from IRMOF-1 to IRMOF-10 to IRMOF-16, the critical temperature of benzene approaches its bulk value (Table I.1). This trend agrees with Walton et al., which reports that the pore-filling pressure shifts toward the bulk condensation pressure with increasing pore size in the IRMOF series.[84] For IRMOFs with the same linker length, such as IRMOF-1 and IRMOF-7 or IRMOF-10 and IRMOF-14, the addition of a side group lowers the critical temperature since the window size is lowered, which effectively decreases guest-guest interactions. Conversely, we expect that micropore topologies more constrictive than that of IRMOF-1 may lower the critical temperature below the triple point, at which point vapor-liquid coexistence would not be observed. It is also expected that the strengths of the guest-guest and guest-host interactions play a key role, as relatively stronger guest-host interactions would decrease the enthalpic benefit of the liquid phase and thus lower the critical temperature.

4.5 Conclusions

Our MC simulations and NMR relaxation experiments have uncovered a novel type of condensation in a microporous metal-organic framework IRMOF-1 that occurs over multiple unit cells, a phenomenon which we call "framework-inhibited condensation." Framework-inhibited condensation plays a crucial role in determining adsorbate behavior and motion. Our simulations also predict that changes in the pore structure and chemistry would modulate the phase behavior, and thus, precise control could be obtained via framework modification. This control could be exploited in applications that depend on adsorption and diffusion behavior, such as in separations and catalysis. For example, condensation of a guest inside a membrane blocks permeation of other components, thereby enhancing the selectivity for the condensed component.[105] As the pressure decreases across the membrane, the component would then vaporize, resulting in higher permeation rates. Condensation could also be leveraged in catalytic applications, as the local density and diffusion of reactants and products, and therefore the reaction rates and selectivities, would be greatly affected.[106]

4.6 Acknowledgements

This research was conducted with Efrem Braun, Sondre Schnell, Li-Chiang Lin, Berend Smit, and Jeffrey A. Reimer. This work was supported as part of the Center for Gas Separations Relevant to Clean Energy Technologies, an Energy Frontier Research Center funded by the

U.S. Department of Energy, Office of Science, Basic Energy Sciences under Award No. DE-SC0001015.

Chapter 5

Effects of Adsorbate-Framework Interaction Strength on the Diffusion of Condensable Guests in Metal-Organic Frameworks

5.1 Abstract

We explore the effects of guest-framework interaction strength on diffusion mechanisms in porous media by investigating the self-diffusion of liquids in model metal-organic frameworks. This interaction strength was varied by varying the chemical functionality of the guest from *p*-xylene to anisole and of the framework from MOF-5 to IRMOF-3. Both guests would exhibit weak guest-framework interactions in MOF-5 due to the lack of any strong interactions. Conversely, the interaction strength between anisole and IRMOF-3 would be strong due to the interaction and possible hydrogen bonding of the methoxy and amine functional groups on the adsorbate and framework, respectively. The diffusion behavior of both *p*-xylene and anisole in MOF-5, as measured by nuclear magnetic resonance (NMR) diffusometry, suggests an isotropic diffusion process modulated by vapor-liquid coexistence. Both observations are consistent with weak guest-framework interactions. Upon addition of an amine side group to the framework in IRMOF-3, the diffusion behavior changes drastically, suggesting the suppression of condensation and an increase in the diffusion activation energy due to increased guest-framework interaction strength. Further investigations are necessary with the IRMOF-3 framework, as the mechanism of diffusion still eludes our understanding, especially at lower guest loadings.

5.2 Introduction

The diffusion of adsorbed molecules (i.e. guests) in porous media plays a critical role in determining the material's performance in a wide variety of applications, such as in separations and catalysis. Metal-organic frameworks possess modular structures that allow for the characteristics of the porous material, such as the pore shape, pore size, and the pore chemistry, to be tuned independently from one another. This tunability, which has led to the development of materials with outstanding properties, also makes metal-organic frameworks a near-ideal platform for studying the effects of pore structure and chemistry on diffusion phenomena. Current efforts to understand adsorbate motion in MOFs commonly include combinations of molecular dynamics (MD)[107] and experimental techniques such as NMR diffusometry,[76, 108-110] infrared microscopy,[111] interference microscopy,[112-113] and quasi-elastic neutron scattering (QENS).[114-118] These studies primarily focus on measuring the self-diffusion or transport diffusion of small gas molecules (i.e. H_2, CO_2, and CH_4) in a limited number of frameworks. Fewer studies address the diffusion of liquid molecules, such as benzene, xylenes, large alkanes,[109, 111, 117-120] and alcohols.[76, 121] The motion of larger liquid molecules tends to exhibit more complex behavior than small gas molecules due to stronger guest-guest and guest-framework interactions. Indeed, in Chapter 4 we describe a novel condensation phenomenon that results in vapor-liquid coexistence of benzene and xylenes in IRMOF-type structures, a complex behavior that does not exist for small gas molecules, and the presence of condensation would undoubtedly affect the diffusion behavior. Furthermore, separation and catalysis applications in the liquid phase would be of particular relevance due to the limited thermal stability of metal-organic frameworks.[122-123]

To facilitate a deeper understanding of liquid motion in porous media, we investigate the effects of modulating guest-framework interactions on diffusion processes in model systems. We adsorb two liquid aromatic molecules (*p*-xylene and anisole) into two isoreticular MOFs (MOF-5 and IRMOF-3) to create systems with disparate interaction strength while maintaining nearly-identical pore structures. The guest-framework interaction strength between *p*-xylene and MOF-5 is weak due to the nonpolar nature of both constituents, a classification that is supported by diffusion and MD simulations of benzene in MOF-5.[92, 110] Conversely, the interaction strength between anisole and IRMOF-3 would be strong due to the interaction and possible hydrogen bonding of the methoxy and amine functional groups on the adsorbate and framework, respectively. Vapor-liquid coexistence as a result of framework-inhibited condensation would likely exist for both liquid molecules in MOF-5 given our simulations results in Chapter 4, though it remains unknown whether condensation occurs in IRMOF-3. Regardless,

condensation effects must be considered along with variations in guest-framework interaction strength. The motion of *p*-xylene and anisole through MOF-5 and IRMOF-3 was probed using nuclear magnetic resonance (NMR) diffusometry. This technique uses magnetic field gradients to encode position with the variations in the resonance frequency, allowing for the measurement self-diffusion coefficients. These diffusion coefficients reveal the intricacies of translational motion, and by varying temperature the thermodynamics of these motions can be analyzed using transition state theory.

Our studies reveal that the diffusion of *p*-xylene and anisole in MOF-5 remains isotropic and is loading-invariant, a finding consistent with previous studies of benzene diffusion in MOF-5. This suggests the presence of framework-inhibited condensation, which is promoted by stronger guest-guest interactions and weaker guest-framework interactions. The activation energy for diffusion also exhibits a minimal dependence on adsorbate loading, which may also result from condensation. Both molecules exhibit time-dependent self-diffusion coefficients, a phenomenon that may stem from diffusion restrictions from crystal defects. In stark comparison, the activation energies of *p*-xylene and anisole in IRMOF-3 appear to increase significantly with decreased loading, suggesting the lack of vapor-liquid coexistence perhaps due to much stronger adsorbate-framework interactions. Notably, at the lowest loadings tested, anisole in IRMOF-3 exhibits signs of multiple diffusion coefficients that may arise from the coexistence of strongly bound molecules and weakly bound molecules. Our understanding of anisole motion in IRMOF-3 is incomplete, and additional studies are required to develop a clearer picture of the effects of strong adsorbate-framework interactions on diffusion in MOFs.

5.3 Experimental Details

5.3.1 Synthesis of MOF-5

Please see section 4.3.4 for details concerning the synthesis of MOF-5.

5.3.2 Synthesis of IRMOF-3

All reagents were obtained from commercial vendors and used without further purification. The compound MOF-5 was synthesized and activated using a strategy adopted from previous reports.[29, 124] Specifically, 2-aminoterephthalic acid (0.72 g, 4.0 mmol), $Zn(NO_3)_2 \cdot 6H_2O$ (3.6 g, 12 mmol), and N,N-diethylformamide (DEF, 100 mL) were combined in a 250-mL glass jar sealed with a Telfon-lined lid. The jar was heated at 100 °C for 24 h then placed under N_2, and the reaction solvent was decanted and replaced with anhydrous N,N-dimethylformamide (DMF) at room temperature. The DMF was exchanged with fresh,

anhydrous DMF seven further times. The DMF was decanted from the glass jar containing the IRMOF-3 crystals, and the residual DMF transferred along with the crystals was then exchanged with anhydrous dichloromethane (DCM) at room temperature. The DCM was exchanged with fresh, anhydrous DCM seven further times, and then the majority of the DCM was removed via cannula. The resulting brown, cubic crystals with diameters of >100 μm were activated by heating at 150°C under vacuum for 24 h. The successful synthesis and activation of the framework was confirmed by comparing the X-ray powder diffraction pattern and Langmuir surface areas to those previously reported. The Langmuir surface area was >3500 m^2/g, indicating a near-ideal IRMOF-3 framework.[125]

5.3.3 Preparation of *p*-Xylene- and Anisole-exchanged MOF-5 and IRMOF-3

The residual DMF remaining along with the MOF crystals (either MOF-5 or IRMOF-3) in the glass jar was exchanged with anhydrous solvent (either *p*-xylene or anisole) at room temperature. The solvent was exchanged with fresh, anhydrous solvent seven further times. The solvent-exchanged crystals were filtered under N_2 to remove excess solvent and sieved to a size >500 μm. Subsequent thermogravimetric analysis (TGA Q50, TA Instruments, New Castle, DE) was used to quantify solvent content of the solvent-filled MOF. Samples were held at room temperature for 10 minutes then heated to 500°C at 1°C/min under a nitrogen purge. Solvent loading was determined from the mass loss prior to degradation temperatures for each material. Solvent loading was systematically varied by micropipette addition or thermal evaporation in a N_2 purged vacuum oven. After any variation, the solvent loading was verified with by TGA.

In order to verify the quality of the crystals after solvent exchange, a portion of the solvent-exchanged MOF-5 crystals was transferred to a 20 mL vial. The residual solvent transferred along with the crystals was then exchanged with anhydrous dichloromethane (DCM) at room temperature. The DCM was exchanged with fresh, anhydrous DCM seven further times, and then the majority of the DCM was removed via cannula. The crystals were activated by heating at 150 °C under vacuum for 24 h, and the quality of the crystals was verified by comparing the X-ray powder diffraction pattern and Langmuir surface areas to those previously reported. All samples were equilibrated at room temperature for at least 24 hours before testing, which was necessary to stabilize NMR behavior, though samples of anisole in IRMOF-3 required even longer equilibration times on the order of a week.

5.3.4 NMR Experiments

Samples of solvent-exchanged MOF were placed in 5 mm NMR tubes equipped with high-pressure sealing caps to minimize any solvent evaporation. ^{1}H-NMR relaxation measurements were performed with a single-sided 13.1 MHz Profile NMR-MOUSE (**MO**bile **U**niversal **S**urface **E**xplorer) with a linear gradient of 7 T·m^{-1}. The magnet was equipped with a homebuilt variable-temperature (VT) probe, and the temperature of the sample was controlled with a constant N_2 flow for heating and cooling. The temperature was held at each set point for at least an hour to ensure thermal equilibrium. A Kea II spectrometer was used for pulse generation and signal acquisition. Stimulated echo (STE) experiments with CPMG acquisition were used to measure the diffusion coefficient in the stray field gradient of the NMR-MOUSE (see Figure 2.1), while saturation recovery experiments were used to measure T_1. Though most samples tested possessed long T_2 times, and thus, did not require T_2 correction for the STE experiments, a select few samples possessed short enough T_2 times for correction to be necessary. To correct for T_2 effects during the STE experiments, the $T_{2,eff}$ (i.e. the T_2 with gradient effects) was measured on the NMR-MOUSE using CPMG experiments. The diffusion rates in samples requiring T_2 correction were slow, and thus, $T_{2,eff} \sim T_2$, allowing for the use of $T_{2,eff}$ instead of T_2 for normalization.

5.4 Results and Discussion

5.4.1 Stimulated Echo Diffusion Measurements in MOF-5

Stimulated echo (STE) experiments in the presence of a constant field gradient can be used to measure the self-diffusion coefficient (D_{self}) of molecules confined in porous media.[62, 126] The pulse experiment (see Appendix A.4) measures the signal decay (S/S_0) caused by diffusion of molecules through the gradient during a diffusion time Δ by varying δ, a time period in the pulse experiment. If self-diffusion is isotropic in three dimensions, the self-diffusion coefficient can be extracted from exponential fits of S/S_0 using the following equations.[57]

$$\ln\left(\frac{S}{S_0}\right) = -bD_{self}(\gamma g\delta)^2\left(\Delta + \frac{2}{3}\delta\right) - \frac{\Delta}{T_1} - \frac{2\delta}{T_2} \qquad 5.1$$

$$b = (\gamma g\delta)^2\left(\Delta + \frac{2}{3}\delta\right) \qquad 5.2$$

In these expressions, g is the gradient strength, γ is the nuclear gyromagnetic ratio, and $T_{1,2}$ are the longitudinal and transverse relaxation times, respectively. The terms associated with the diffusion modulated decay can be summarized as a parameter (b) with units of inverse diffusion (sm^{-2}). Figure 5.1 displays the diffusion decays for *p*-xylene (PX) and anisole (AN) adsorbed in MOF-5 at various loadings and temperatures. All decays are exponential, indicating that the diffusion processes for both molecules are indeed isotropic. Previous studies of benzene diffusion MOF-5 also conclude that the diffusion is isotropic, but notably, they observe biexponential diffusion decays, an observation they attribute to the assumed presence of defects as well as the confirmed presence of trace amounts of large, bulky, synthetic solvent molecules (N,N-diethyl formamide, DEF).[91, 110] Given the quality of the framework crystals in our studies compared to those in previous studies (>5000 m^2/g surface area in this work versus 3400 m^2/g in previous studies), the single exponential diffusion decays indicate that our measurements are free of any confounding factors, and therefore, more accurately capture the diffusion process.

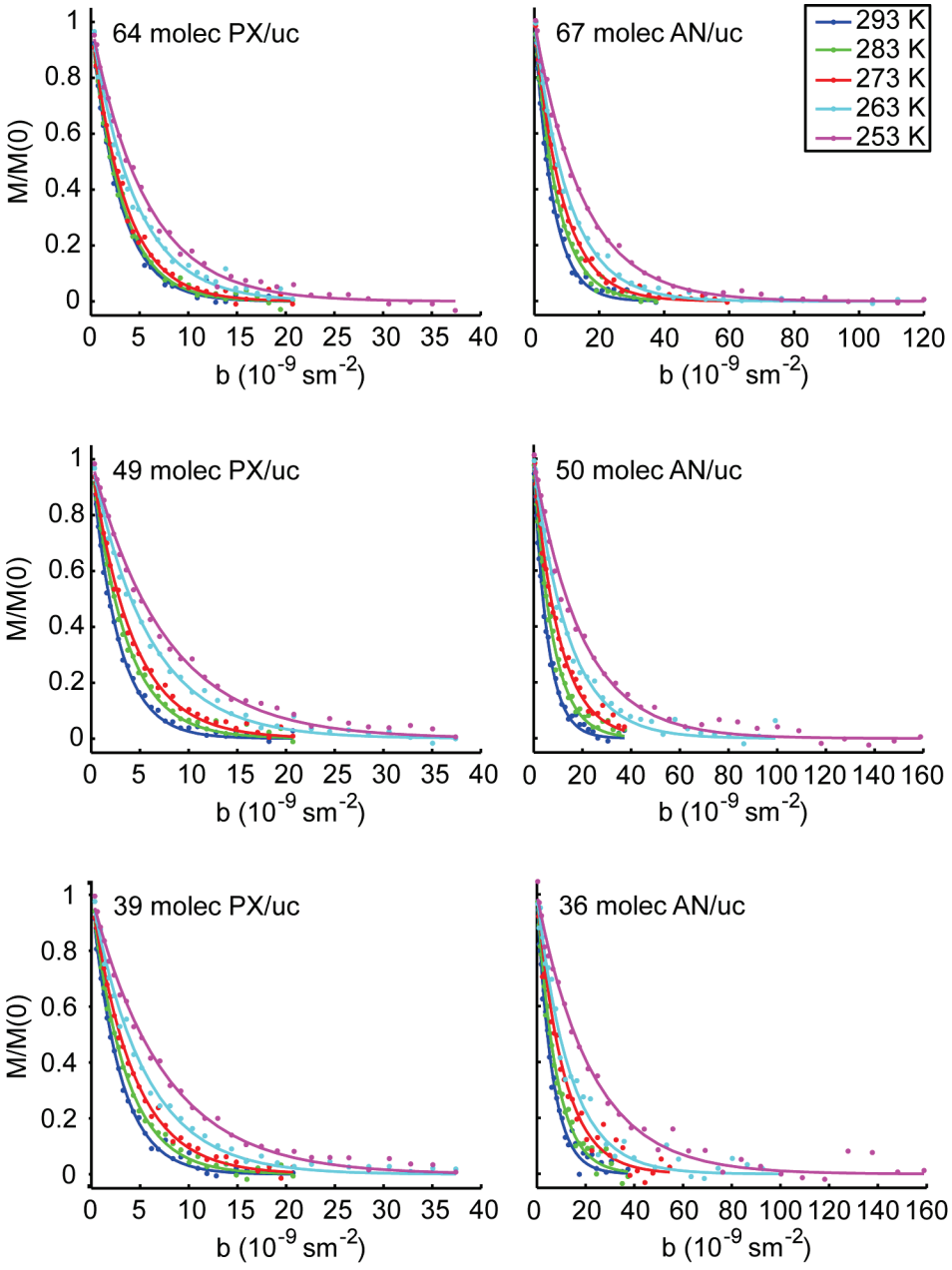

Figure 5.1. Diffusion decays (dots) and associated exponential fits (lines) for *p*-xylene (PX) and anisole (AN) in MOF-5 with a diffusion time Δ of 10 ms at temperatures of 293-253K. For PX, loadings of 64, 49, and 39 molecules per unit cell were tested. For AN, loadings of 67, 50, and 36 molecules per unit cell were tested.

The diffusion coefficients for *p*-xylene (3.4-3.7 x 10^{-10} m^2/s) and anisole (1.6-1.8 x 10^{-10} m^2/s) at room temperature were nearly invariant with respect to loading (see Figure 5.2 for D_{self} values), an observation that agrees with the behavior measured for benzene in MOF-5, though the D_{self} values are approximately a factor of two and four smaller than that for benzene. The loading-invariance of D_{self}, as well as the deviation from predicted D_{self} values from molecular dynamics (MD), was hypothesized to be the resul;t of benzene clustering, a phenomena that was assumed to occur at a threshold loading between 10-20 molecules per unit cell.[91] The condensation behavior established in Chapter 4 closely mimics the proposed clustering behavior, and thus, the observed loading-invariance is likely a product of framework-inhibited condensation. Since the measured diffusion would be dominated by the liquid-like phase at the loadings and temperatures tested (i.e. high loadings, low temperature), variations in the loading would only change the amount of liquid-like phase. In other words, the density of the liquid-like phase remains constant at a given temperature, and a constant density would result in a loading-invariant diffusion environment. Small changes in the diffusion coefficient may result in the effects of exchange between the liquid-like phase and vapor-like phase. This is especially the case at longer diffusion times where a molecule diffuses farther and thus possesses a higher probability of exchanging between the two phases, as described in Section 4.4.3.

Notably, D_{self} values for *p*-xylene and anisole in MOF-5 are smaller than those for benzene in MOF-5 (~7 x 10^{-10} at 298K) by a factor of ~2 and ~3.5, respectively. This difference is larger than expected given that the similarity of the neat liquid diffusion coefficients. The measured diffusion values of neat *p*-xylene, and anisole (~1.9 and 1.1 x 10^{-9} m^2/s at 293K, see Appendix H.4) are nearly the same as the literature value for the diffusion coefficient of neat benzene (2.2 x 10^{-9} m^2/s at 298K).[127] We hypothesize that the difference in the diffusion coefficients of *p*-xylene, anisole, and benzene upon adsorption in MOF-5 may result from differences in condensation behavior for each molecule, but further work is needed to explore the origins of this observation.

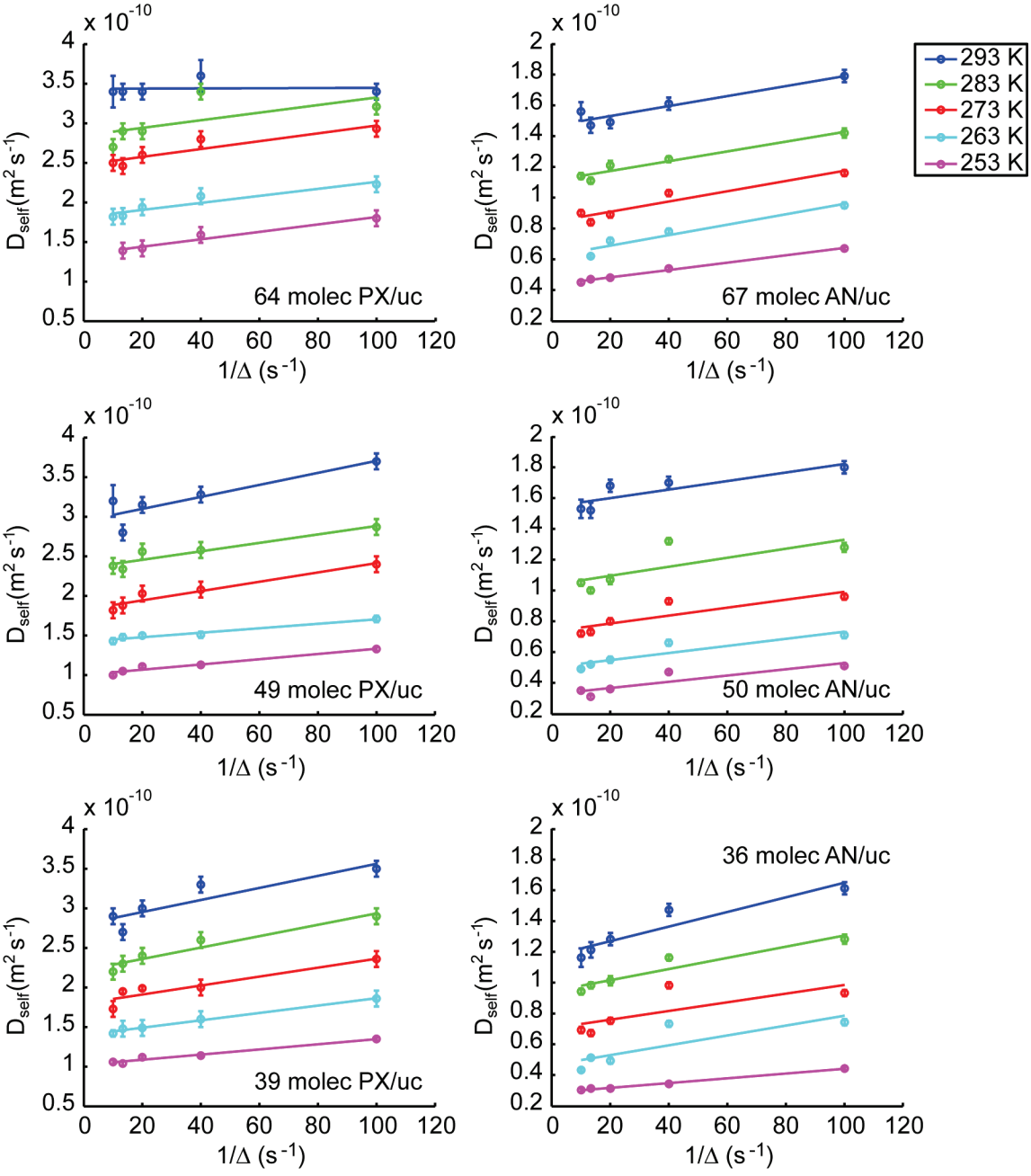

Figure 5.2. The self-diffusion coefficients (D_{self}) of *p*-xylene (PX) and anisole (AN) plotted versus Δ^{-1}. The dependence of D_{self} with Δ~ms indicates restrictions to diffusion occurring on the ~μm length scale. The lines indicate the linear fits used to extract the asymptotic diffusion coefficient (D_∞). The error bars indicate the standard error of the exponential fits to obtain D_{self}.

5.4.2 Dependence of Diffusion Coefficient on Diffusion Time in MOF-5

D_{self} also appears to decrease (see Figure 5.2) as Δ increases from 10 ms to 100 ms. A time-dependent diffusion coefficient strongly indicates the presence of restricted diffusion[22] and is common when considering the diffusion of molecules in porous media. However, the measured D_{self} varies as Δ changes on the millisecond timescale, indicating that the diffusion restriction must be on the order of the diffusion length $(D_{self}\,\Delta)^{1/2}$ ~ μm, thereby eliminating the windows between MOF-5 cages as the source of restricted diffusion. The time-dependence is seen even at high loadings, where the framework would be almost entirely filled with the liquid-like phase, and the behavior of the time dependence appears to be relatively invariant with loading. Both of these observations suggest that confinement in a liquid droplet is not the source of the diffusion restriction. The presence of crystal defects on the μm length scale (see Appendix H.5) suggests that these defects may restrict diffusion and result in a time dependent diffusion coefficient. Further work is needed to investigate the origins of this time dependent diffusion coefficient.

5.4.3 Transition-State Theory Analysis of Diffusion in MOF-5

The presence of a time-dependent D_{self} complicates the transition-state theory analysis that would yield insight into the thermodynamics of the diffusion process; to compare between different guests and loadings, a consistent metric must be established. We e apply a linear fit (see Figure 5.2) to the time-dependent D_{self} with respect to Δ^{-1} to extract the asymptotic diffusion coefficient (D_∞), or the diffusion coefficient at infinite time, from the extrapolated intercept.[128] We choose this metric due to the importance of long-range diffusion in actual applications. Though this asymptotic limit would also include the possible effects of grain boundaries, we suspect that the general diffusion behavior still reflects the interactions between the guest and the framework due to the high quality of our MOF crystals. The dependence of D_∞ as a function of inverse temperature follows an Arrhenius relationship (see Figure 5.3).

$$D_\infty = D_0 e^{-E_{a,diff}/RT} \tag{5.3}$$

This expression allows for the extraction of the diffusion activation energies ($E_{a,diff}$) and pre-exponential factors (D_0) as shown in Figure 5.4. A table summarizing all of the results from the Arrhenius fits can be found in Table H.5. We limit our analysis to the activation energies due to the large error bounds for the pre-exponential factors.

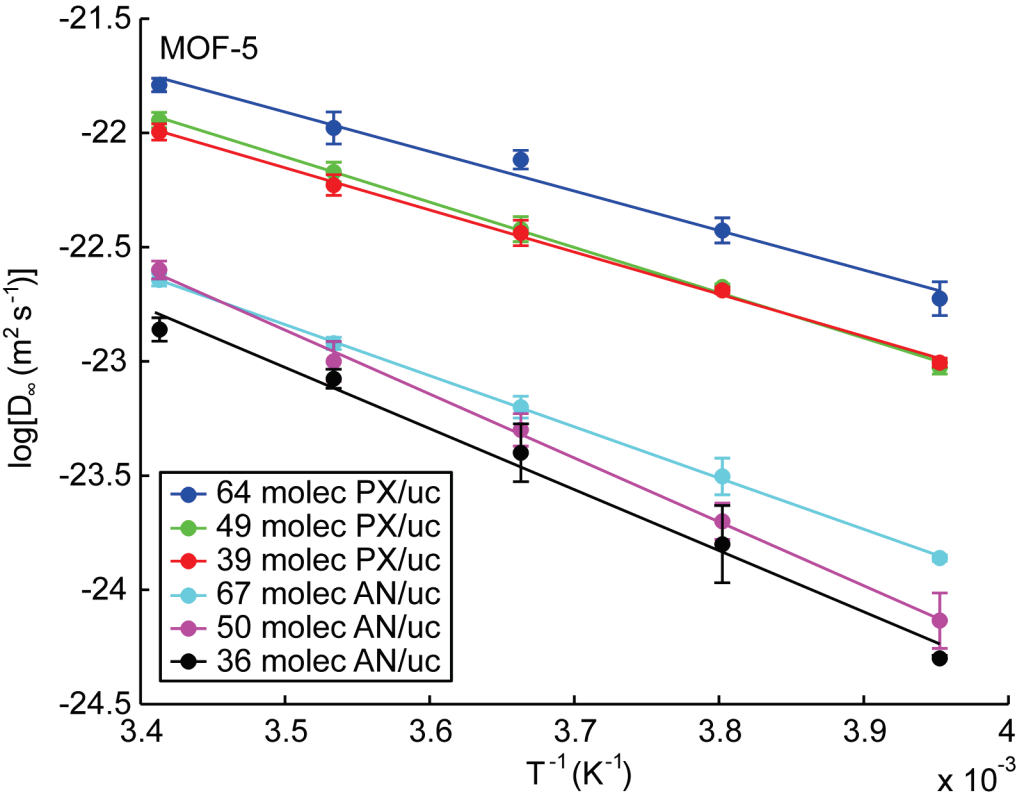

Figure 5.3. The asymptotic diffusion coefficient D_∞ as a function of inverse temperature for *p*-xylene and anisole in MOF-5 at all loadings. The lines indicate the Arrhenius fits used to extract the activation energy and pre-exponential factors for diffusion. The error bars represent the standard error of the fits to obtain D_∞.

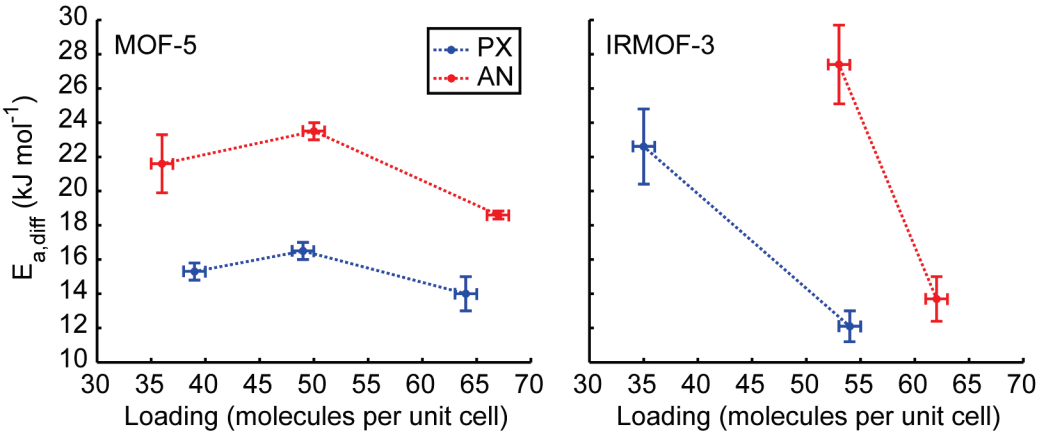

Figure 5.4. The activation energy for diffusion ($E_{a,diff}$) of *p*-xylene (PX) and anisole (AN) obtained from the Arrhenius fits of D_∞. Results are shown for both MOF-5 (left) and IRMOF-3 (right). The error bars for $E_{a,diff}$ indicate the standard error from the fit, while the error bars for the loading are ±1 molecule per unit cell, as estimated from errors in the TGA analysis. The dotted lines are guides for the eye.

Both liquid molecules exhibit activation energies and pre-exponential factors that are relatively invariant with respect to loading, consistent with the presence of vapor-liquid coexistence. Further measurements at additional loadings would bolster this hypothesis. The $E_{a,diff}$ for *p*-xylene (~14-16 kJ/mol) is similar to that found for benzene at high loadings[91] while the $E_{a,diff}$ for anisole (~19-24 kJ/mol) is higher than that for *p*-xylene. The difference between the two liquid molecules is expected given the activation energies for the neat liquids (see Appendix H.4).

5.4.4 Discussion of Diffusion Mechanisms in IRMOF-3

Our preliminary data indicates that the diffusion behavior of *p*-xylene and anisole differs dramatically upon functionalization of the framework with amine groups. Though the diffusion of *p*-xylene and anisole in IRMOF-3 exhibits similar activation energies at high loadings, $E_{a,diff}$ now appears to increase sharply as loading decreases, which is difficult to rationalize in the context of vapor-liquid coexistence and constant phase densities. Indeed, MD simulations indicate that increasing the strength of guest-framework interactions and decreasing the window size with functional groups would reduce the critical temperature for vapor-liquid coexistence. Since IRMOF-3 would possess both effects (see Figure 5.5), and since $E_{a,diff}$ depends so strongly on loading, vapor-liquid coexistence of *p*-xylene and anisole may not occur within this framework. At high loadings, a uniform adsorbed phase in IRMOF-3 would resemble the

liquid-like phase in MOF-5, resulting in similar diffusion environments. As the loading decreases, the adsorbed phase in IRMOF-3 would decrease in density and associate more strongly with the framework, since stronger adsorption sites would necessarily be near the cage corners and linkers.[129] Uniform adsorption would explain the large increase in $E_{a,diff}$ for *p*-xylene, which exhibits no specific interactions with the amine side group. This would also explain why $E_{a,diff}$ for anisole is higher than *p*-xylene at lower loadings, due to the possible presence of hydrogen bonding, and thus, stronger adsorption. Note that the diffusion coefficient remains dependent on Δ and that the $E_{a,diff}$ values obtained are for D_∞. This Δ dependence likely remains due to the continued presence of crystal defects in IRMOF-3. All of these hypotheses remain speculative, and further experimentation must be performed.

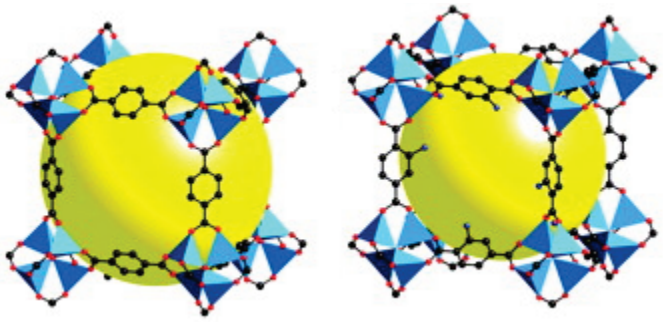

Figure 5.5. Comparison of MOF-5 structure (left) and IRMOF-3 structure (right). Color scheme is as follows: Zn (blue polyhedra), O (red spheres), C (black spheres), and N (grey spheres), with hydrogen atoms omitted. Note that the presence of amine groups would narrow the pore windows.

Interestingly, when decreasing the loading of anisole in IRMOF-3 to 35 molecules per unit cell, the diffusion decay exhibits multi-exponential behavior (see Figure H.13) at longer diffusion times (Δ = 75 ms and 100 ms). Furthermore, the rate of decay slows drastically between Δ = 50 ms and 75 ms. This highly unexpected and puzzling behavior could result from multiple diffusion populations or even anisotropic diffusion.[22] Given the isotropic nature of IRMOF-3, the former is a more plausible explanation. Each unit cell of IRMOF-3 possesses 8 cages and 24 linkers; therefore, each cage possesses three amine groups on average. Thus, it is possible that the two populations with differing diffusion characteristics may arise from anisole associated and unassociated with the amine groups that are strongly and weakly bound, respectively. Regardless,

these hypotheses remain speculative, and further work is needed to uncover the mechanism of diffusion for anisole in IRMOF-3.

5.5 Conclusions and Future Work

In this study, we investigated the effects of modulating the guest-framework interaction strength on the mechanisms of diffusion in metal-organic frameworks. The NMR diffusometry measurements of *p*-xylene and anisole in MOF-5 suggest an isotropic diffusion process modulated by vapor-liquid coexistence caused by framework-inhibited condensation. Upon the addition of an amine side group, the diffusion behavior changes drastically, which suggests the suppression of condensation and the presence of stronger guest-framework interactions. For anisole in IRMOF-3 at a loading of 35 molecules per unit cell, multiple populations with differing diffusion characteristics may arise due to possible hydrogen-bonding with the framework, though additional work is necessary to understand this phenomenon.

Further investigations into the diffusion of anisole through IRMOF-3 should begin with molecular dynamics and Monte Carlo simulations in order to gain molecular insight and guide further NMR experimentation. These simulations may reveal the presence of multiple populations or perhaps signal some other cause for multi-exponential diffusion decays.

Degradation was not expected to be an issue due to the relatively low temperatures used for loading modulation (~100°C), and subsequent XRD analysis confirmed the crystallinity of the heated samples. However, removal of guests from IRMOF-3 required many hours of heating, and therefore, confirmation of the diffusion results with replicate samples prepared using high vacuum in the absence of heating would be a useful control measurement. Also, the time necessary to equilibrate the NMR measurements in the IRMOF-3 samples is very long (up to weeks), and thus, the diffusion measurements of IRMOF-3 samples may require longer equilibration times at each temperature. It is unknown why this equilibration is so slow.

Additional diffusion experiments should begin by testing additional loadings to confirm the trends in $E_{a,diff}$ for IRMOF-3. Though Goldman-Shen[130] experiments of *p*-xylene in MOF-5 indicated negligible cross relaxation, additional experiments should be performed in the IRMOF-3 samples to exclude effects of cross relaxation on the diffusion measurements.[131] Also, the T_2 relaxation distributions obtained at 13 MHz for lower loadings of *p*-xylene and anisole in IRMOF-3 exhibit significant multi-exponential behavior, suggesting the presence of multiple solvent populations (see Appendix H.3). The origin of this behavior remains unknown. Experiments could also be conducted with a wider range of diffusion times for both frameworks to investigate the origin of the time-dependent diffusion coefficient.

The interaction of anisole with IRMOF-3 can be investigated using infrared (IR) spectroscopy to verify the presence of hydrogen bonding, and the interaction strength could be tuned by using a multivariate (MTV) MOF consisting of a mixture of the MOF-5 and IRMOF-3 linkers in different proportions.[9, 132]

5.6 Acknowledgements

This research was conducted with Lucy Meng Yu, Denise Kleinschmidt, and Jeffrey A. Reimer. This work was supported as part of the Center for Gas Separations Relevant to Clean Energy Technologies, an Energy Frontier Research Center funded by the U.S. Department of Energy, Office of Science, Basic Energy Sciences under Award No. DE-SC0001015. Denise Kleinschmidt acknowledges a research fellowship through the Aachen-California Network of Academic Exchange.

Bibliography

[1] H. Furukawa, K. E. Cordova, M. O'Keeffe, O. M. Yaghi, *Science* **2013**, *341*, 1230444.

[2] H. Furukawa, N. Ko, Y. B. Go, N. Aratani, S. B. Choi, E. Choi, A. O. Yazaydin, R. Q. Snurr, M. O'Keeffe, J. Kim, O. M. Yaghi, *Science* **2010**, *329*, 424-428.

[3] M. Eddaoudi, J. Kim, N. Rosi, D. Vodak, J. Wachter, M. O'Keeffe, O. M. Yaghi, *Science* **2002**, *295*, 469-472.

[4] R. Banerjee, A. Phan, B. Wang, C. Knobler, H. Furukawa, M. O'Keeffe, O. M. Yaghi, *Science* **2008**, *319*, 939-943.

[5] N. Stock, T. Bein, *Angew. Chem. Int. Ed.* **2004**, *43*, 749-752.

[6] K. Sumida, S. Horike, S. S. Kaye, Z. R. Herm, W. L. Queen, C. M. Brown, F. Grandjean, G. J. Long, A. Dailly, J. R. Long, *Chem. Sci.* **2010**, *1*, 184-191.

[7] N. Stock, S. Biswas, *Chem. Rev.* **2012**, *112*, 933-969.

[8] H. Li, M. Eddaoudi, M. O'Keeffe, O. M. Yaghi, **1999**, *402*, 276-279.

[9] H. Deng, C. J. Doonan, H. Furukawa, R. B. Ferreira, J. Towne, C. B. Knobler, B. Wang, O. M. Yaghi, *Science* **2010**, *327*, 846-850.

[10] M. M. Chui, R. J. Phillips, M. J. McCarthy, *J. Colloid Interface Sci.* **1995**, *174*, 336-344.

[11] O. M. Yaghi, H. Li, T. L. Groy, *J. Am. Chem. Soc.* **1996**, *118*, 9096-9101.

[12] P. D. Dietzel, R. E. Johnsen, R. Blom, H. Fjellvag, *Chemistry* **2008**, *14*, 2389-2397.

[13] P. D. Dietzel, B. Panella, M. Hirscher, R. Blom, H. Fjellvag, *Chem. Commun.* **2006**, 959-961.

[14] S. R. Caskey, A. G. Wong-Foy, A. J. Matzger, *J. Am. Chem. Soc.* **2008**, *130*, 10870-10871.

[15] J. A. Mason, K. Sumida, Z. R. Herm, R. Krishna, J. R. Long, *Energy & Environmental Science* **2011**, *4*, 3030-3040.

[16] H. Deng, et al., *Science* **2012**, *336*, 1018-1023.

[17] T. M. McDonald, W. R. Lee, J. A. Mason, B. M. Wiers, C. S. Hong, J. R. Long, *J. Am. Chem. Soc.* **2012**, *134*, 7056-7065.

[18] C. Serre, F. Millange, C. Thouvenot, M. Noguès, G. Marsolier, D. Louër, G. Férey, *J. Am. Chem. Soc.* **2002**, *124*, 13519-13526.

[19] J. H. Cavka, S. Jakobsen, U. Olsbye, N. Guillou, C. Lamberti, S. Bordiga, K. P. Lillerud, *J. Am. Chem. Soc.* **2008**, *130*, 13850-13851.

[20] M. H. Levitt, *Spin dynamics*, Wiley Chichester, UK, **2001**.

[21] H. C. Torrey, *Phys. Rev.* **1956**, *104*, 563.

[22] P. T. Callaghan, *Translational dynamics and magnetic resonance: principles of pulsed gradient spin echo NMR*, Oxford University Press, **2011**.

[23] T. M. McDonald, D. M. D'Alessandro, R. Krishna, J. R. Long, *Chem. Sci.* **2011**, *2*, 2022-2028.

[24] A. R. Millward, O. M. Yaghi, *J. Am. Chem. Soc.* **2005**, *127*, 17998-17999.

[25] A. O. Yazaydın, A. I. Benin, S. A. Faheem, P. Jakubczak, J. J. Low, R. R. Willis, R. Q. Snurr, *Chem. Mater.* **2009**, *21*, 1425-1430.

[26] A. O. Yazaydın, R. Q. Snurr, T. H. Park, K. Koh, J. Liu, M. D. LeVan, A. I. Benin, P. Jakubczak, M. Lanuza, D. B. Galloway, *J. Am. Chem. Soc.* **2009**, *131*, 18198-18199.

[27] J.-R. Li, Y. Ma, M. C. McCarthy, J. Sculley, J. Yu, H.-K. Jeong, P. B. Balbuena, H.-C. Zhou, *Coord. Chem. Rev.* **2011**, *255*, 1791-1823.

[28] K. Sumida, D. L. Rogow, J. A. Mason, T. M. McDonald, E. D. Bloch, Z. R. Herm, T. H. Bae, J. R. Long, *Chem. Rev.* **2012**, *112*, 724-781.

[29] S. S. Kaye, A. Dailly, O. M. Yaghi, J. R. Long, *J. Am. Chem. Soc.* **2007**, *129*, 14176-14177.

[30] E. Biemmi, S. Christian, N. Stock, T. Bein, *Micropor. Mesopor. Mat.* **2009**, *117*, 111-117.

[31] R. Kleinberg, W. Kenyon, P. Mitra, *J. Magn. Reson.* **1994**, *108*, 206-214.

[32] P. J. Barrie, *Annu. Rep. NMR Spectrosc.* **2000**, *41*, 265-316.

[33] R. Brown, P. Fantazzini, *Phys. Rev. B* **1993**, *47*, 14823-14834.

[34] F. D'Orazio, S. Bhattacharja, W. Halperin, K. Eguchi, T. Mizusaki, *Phys. Rev. B* **1990**, *42*, 9810-9818.

[35] S. Davies, K. Packer, *J. Appl. Phys.* **1990**, *67*, 3163-3170.

[36] W. P. Halperin, J. Y. Jehng, Y. Q. Song, *Magn. Reson. Imaging* **1994**, *12*, 169-173.

[37] F. Jaeger, S. Bowe, H. Van As, G. E. Schaumann, *Eur. J. Soil. Sci.* **2009**, *60*, 1052-1064.

[38] W. Kenyon, J. Howard, A. Sezginer, C. Straley, A. Matteson, K. Horkowitz, R. Ehrlich, in *Trans. SPWLA Ann. Logging Symp., Vol. 30*, **1989**.

[39] J. P. Korb, *New Journal of Physics* **2011**, *13*, 035016.

[40] H. A. Resing, *Advances in Molecular Relaxation Processes* **1972**, *3*, 199-226.

[41] L. R. Stingaciu, L. Weihermüller, S. Haber-Pohlmeier, S. Stapf, H. Vereecken, A. Pohlmeier, *Water Resour. Res.* **2010**, *46*, W11510.

[42] R. Valckenborg, L. Pel, K. Kopinga, *J. Phys. D: Appl. Phys.* **2002**, *35*, 249-256.

[43] K. Washburn, P. Callaghan, *Phys. Rev. Lett.* **2006**, *97*, 175502

[44] J. Kärger, R. Valiullin, *eMagRes* **2011**.

[45] J. Mitchell, T. C. Chandrasekera, M. L. Johns, L. F. Gladden, E. J. Fordham, *Phys. Rev. E* **2010**, *81*.

[46] P. J. McDonald, J. P. Korb, J. Mitchell, L. Monteilhet, *Phys. Rev. E* **2005**, *72*, 011409.

[47] L. Monteilhet, J.-P. Korb, J. Mitchell, P. McDonald, *Phys. Rev. E* **2006**, *74*, 061404.

[48] K. R. Brownstein, C. Tarr, *Phys. Rev. A* **1979**, *19*, 2446-2453.

[49] M. D. Hürlimann, *J. Magn. Reson.* **1998**, *131*, 232-240.

[50] D. I. Kolokolov, H. Jobic, A. G. Stepanov, J. Ollivier, S. Rives, G. Maurin, T. Devic, C. Serre, G. Férey, *J. Phys. Chem. C* **2012**, *116*, 15093-15098.

[51] T. Ueda, K. Kurokawa, Y. Kawamura, K. Miyakubo, T. Eguchi, *J. Phys. Chem. C* **2012**, *116*, 1012-1019.

[52] M. Wehring, J. Gascon, D. Dubbeldam, F. Kapteijn, R. Snurr, F. Stallmach, *J. Phys. Chem. C* **2010**, *114*, 10527-10534.

[53] A. N. Mlinar, G. B. Baur, G. G. Bong, A. Getsoian, A. T. Bell, *J. Catal.* **2012**.

[54] K. Sumida, C. M. Brown, Z. R. Herm, S. Chavan, S. Bordiga, J. R. Long, *Chem. Commun. (Cambridge, U. K.)* **2011**, *47*, 1157-1159.

[55] S. S. Chui, *Science* **1999**, *283*, 1148-1150.

[56] A. Schaate, P. Roy, A. Godt, J. Lippke, F. Waltz, M. Wiebcke, P. Behrens, *Chemistry* **2011**, *17*, 6643-6651.

[57] B. Blümich, J. Perlo, F. Casanova, *Prog. Nucl. Magn. Reson. Spectrosc.* **2008**, *52*, 197-269.

[58] G. Eidmann, R. Savelsberg, P. Blümler, B. Blümich, *J. Magn. Reson.* **1996**, *122*, 104-109.

[59] J. Perlo, F. Casanova, B. Blumich, *J. Magn. Reson.* **2005**, *176*, 64-70.

[60] H. Carr, E. Purcell, *Phys. Rev.* **1954**, *94*, 630-638.

[61] S. Meiboom, D. Gill, *Rev. Sci. Instrum.* **1958**, *29*, 688-691.

[62] F. Casanova, J. Perlo, B. Blümich, *Single-sided NMR*, Springer, **2011**.

[63] S. W. Provencher, *Comput. Phys. Commun.* **1982**, *27*, 213-227.

[64] L. Venkataramanan, Y. Q. Song, M. D. Hurlimann, *IEEE T. Signal Proces.* **2002**, *50*, 1017-1026.

[65] Y. Q. Song, L. Venkataramanan, L. Burcaw, *J. Chem. Phys.* **2005**, *122*, 104104.

[66] J. J. Chen, X. Kong, K. Sumida, M. A. Manumpil, J. R. Long, J. A. Reimer, *Angew Chem Int Ed Engl* **2013**, *52*, 12043-12046.

[67] J. J. Chen, X. Kong, K. Sumida, M. A. Manumpil, J. R. Long, J. A. Reimer, *Angew. Chem. Int. Ed.* **2013**, *52*, 12043-12046.

[68] P. McDonald, J. P. Korb, J. Mitchell, L. Monteilhet, *Phys. Rev. E* **2005**, *72*.

[69] L. Monteilhet, J. P. Korb, J. Mitchell, P. McDonald, *Phys. Rev. E* **2006**, *74*.

[70] M. Van Landeghem, A. Haber, J.-B. D'Espinose De Lacaillerie, B. Blümich, *Concept. Magn. Reson. A* **2010**, *36A*, 153-169.

[71] Y. T. Li, K. H. Cui, J. Li, J.-Q. Zhu, X. Wang, Y.-Q. Tian, *Chinese Journal of Inorganic Chemistry* **2011**, *5*, 951-956.

[72] P. Horcajada, S. Surblé, C. Serre, D.-Y. Hong, Y.-K. Seo, J.-S. Chang, J.-M. Greneche, I. Margiolaki, G. Férey, *Chem. Commun. (Cambridge, U. K.)* **2007**, 2820-2822.

[73] E. D. Bloch, D. Britt, C. Lee, C. J. Doonan, F. J. Uribe-Romo, H. Furukawa, J. R. Long, O. M. Yaghi, *J. Am. Chem. Soc.* **2010**, *132*, 14382-14384.

[74] D. Gygi, E. D. Bloch, J. A. Mason, W. L. Queen, M. R. Hudson, A. Dailly, M. Beckner, C. M. Brown, J. R. Long, *In Preparation*.

[75] J. Kärger, D. M. Ruthven, D. N. Theodorou, *Diffusion in Nanoporous Materials*, Wiley-VCH, Weinheim, Germany, **2012**.

[76] J. A. Gee, J. Chung, S. Nair, D. S. Sholl, *J. Phys. Chem. C* **2013**, *117*, 3169-3176.

[77] J. J. Chen, J. A. Mason, E. D. Bloch, D. Gygi, J. R. Long, J. A. Reimer, *Micropor. Mesopor. Mater.* **2014**.

[78] J. Rouquerol, F. Rouquerol, P. Llewellyn, G. Maurin, K. Sing, *Adsorption by Powders and Porous Solids: Principles, Methodology and Applications*, Academic Press, **2014**.

[79] R. Evans, U. M. B. Marconi, P. Tarazona, *J. Chem. Phys.* **1986**, *84*, 2376-2399.

[80] B. Smit, T. L. M. Maesen, *Nature* **1995**, *374*, 42-44.

[81] R. Radhakrishnan, K. Gubbins, *Phys. Rev. Lett.* **1997**, *79*, 2847-2850.

[82] T. Maris, T. J. H. Vlugt, B. Smit, *J. Phys. Chem. B* **1998**, *102*, 7183-7189.

[83] D. Li, K. Kaneko, *Chem. Phys. Lett.* **2001**, *335*, 50-56.

[84] K. S. Walton, A. R. Millward, D. Dubbeldam, H. Frost, J. J. Low, O. M. Yaghi, R. Q. Snurr, *J. Am. Chem. Soc.* **2008**, *130*, 406-407.

[85] W. Shim, K. Hwang, J. Chung, Y. Baek, S. Yoo, S. Kim, H. Moon, J. Lee, *Adv. Powder Technol.* **2012**, *23*, 615-619.

[86] T. Düren, R. Q. Snurr, *J. Phys. Chem. B* **2004**, *108*, 15703-15708.

[87] L. Sarkisov, T. Düren, R. Q. Snurr, *Mol. Phys.* **2004**, *102*, 211-221.

[88] J. Jiang, S. I. Sandler, *Langmuir* **2006**, *22*, 5702-5707.

[89] J. A. Greathouse, N. W. Ockwig, L. J. Criscenti, T. R. Guilinger, P. Pohl, M. D. Allendorf, *Phys. Chem. Chem. Phys.* **2010**, *12*, 12621-12629.

[90] W. Makowski, M. Mańko, P. Zabierowski, K. Mlekodaj, D. Majda, J. Szklarzewicz, W. Lasocha, *Thermochim. Acta* **2014**, *587*, 1-10.

[91] S. Hertel, M. Wehring, S. Amirjalayer, M. Gratz, J. Lincke, H. Krautscheid, R. Schmid, F. Stallmach, *The European Physical Journal Applied Physics* **2011**, *55*, 20702.

[92] K. Takakura, T. Ueda, K. Miyakubo, T. Eguchi, *Phys. Chem. Chem. Phys.* **2013**, *15*, 279-290.

[93] D. Frenkel, B. Smit, *Understanding Molecular Simulation: From Algorithms to Applications*, Elsevier Science, **2001**.

[94] A. K. Rappe, C. J. Casewit, K. S. Colwell, W. A. Goddard, W. M. Skiff, *J. Am. Chem. Soc.* **1992**, *114*, 10024-10035.

[95] M. A. Addicoat, N. Vankova, I. F. Akter, T. Heine, *J. Chem. Theory Comput.* **2014**, *10*, 880-891.

[96] C. D. Wick, M. G. Martin, J. I. Siepmann, *J. Phys. Chem. B* **2000**, *104*, 8008-8016.

[97] J. Feng, J. A. Reimer, *J. Magn. Reson.* **2011**, *209*, 300-305.

[98] M. Van Landeghem, A. Haber, J. B. D'espinose De Lacaillerie, B. Blümich, *Concept. Magn. Reson. A* **2010**, *36*, 153-169.

[99] P. C. Hansen, *SIAM Review* **1992**, *34*, 561-580.

[100] L. D. Gelb, K. E. Gubbins, R. Radhakrishnan, M. Sliwinska-Bartkowiak, *Rep. Prog. Phys.* **1999**, *62*, 1573-1659.

[101] D. Chandler, *Introduction to Modern Statistical Mechanics*, Oxford University Press, **1987**.

[102] M. Winkler, M. Zhou, M. Bernardo, B. Endeward, H. Thomann, *Magn. Reson. Imaging* **2003**, *21*, 311-315.

[103] R. Brown, P. Fantazzini, *Phys. Rev. B* **1993**, *47*, 14823-14834.

[104] G. Q. Zhang, G. J. Hirasaki, *J. Magn. Reson.* **2003**, *163*, 81-91.

[105] R. J. R. Uhlhorn, K. Keizer, A. J. Burggraaf, *J. Membr. Sci.* **1992**, *66*, 259-269.

[106] N. M. Ostrovskii, N. M. Bukhavtsova, V. K. Duplyakin, *React. Kinet. Catal. Lett.* **1994**, *53*, 253-259.

[107] Q. Yang, C. Zhong, *J. Phys. Chem. B* **2005**, *109*, 11862-11864.

[108] C. Chmelik, D. Freude, H. Bux, J. Haase, *Micropor. Mesopor. Mater.* **2012**, *147*, 135-141.

[109] D. C. Ford, D. Dubbeldam, R. Q. Snurr, V. Kunzel, M. Wehring, F. Stallmach, J. Kärger, U. Muller, *J. Phys. Chem. Lett.* **2012**, *3*, 930-933.

[110] F. Stallmach, S. Groger, V. Kunzel, J. Karger, O. M. Yaghi, M. Hesse, U. Muller, *Angew. Chem. Int. Ed.* **2006**, *45*, 2123-2126.

[111] C. Chmelik, J. Kärger, M. Wiebcke, J. Caro, J. M. van Baten, R. Krishna, *Micropor. Mesopor. Mater.* **2009**, *117*, 22-32.

[112] M. Arnold, P. Kortunov, D. J. Jones, Y. Nedellec, J. Kärger, J. Caro, *Eur. J. Inorg. Chem.* **2007**, *2007*, 60-64.

[113] P. Kortunov, Z. Ni, C. Paur, S. Reyes, J. Zengel, *AIP Conf. Proc.* **2011**, *1330*, 57-60.

[114] N. Rosenbach, H. Jobic, A. Ghoufi, F. Salles, G. Maurin, S. Bourrelly, P. L. Llewellyn, T. Devic, C. Serre, G. Férey, *Angew. Chem. Int. Ed.* **2008**, *47*, 6611-6615.

[115] F. Salles, H. Jobic, G. Maurin, M. Koza, P. Llewellyn, T. Devic, C. Serre, G. Ferey, *Phys. Rev. Lett.* **2008**, *100*, 245901.

[116] Q. Yang, H. Jobic, F. Salles, D. Kolokolov, V. Guillerm, C. Serre, G. Maurin, *Chem. Eur. J.* **2011**, *17*, 8882-8889.

[117] H. Jobic, N. Rosenbach, Jr., A. Ghoufi, D. I. Kolokolov, P. G. Yot, T. Devic, C. Serre, G. Ferey, G. Maurin, *Chemistry* **2010**, *16*, 10337-10341.

[118] S. Rives, H. Jobic, D. I. Kolokolov, A. A. Gabrienko, A. G. Stepanov, Y. Ke, B. Frick, T. Devic, G. Férey, G. Maurin, *J. Phys. Chem. C* **2013**, *117*, 6293-6302.

[119] F. Stallmach, S. Groger, V. Kunzel, J. Karger, O. M. Yaghi, M. Hesse, U. Muller, *Angew Chem Int Ed Engl* **2006**, *45*, 2123-2126.

[120] S. Rives, H. Jobic, F. Ragon, T. Devic, C. Serre, G. Férey, J. Ollivier, G. Maurin, *Micropor. Mesopor. Mater.* **2012**, *164*, 259-265.

[121] C. Chmelik, H. Bux, J. Caro, L. Heinke, F. Hibbe, T. Titze, J. Kärger, *Phys. Rev. Lett.* **2010**, *104*, 085902.

[122] J.-R. Li, J. Sculley, H.-C. Zhou, *Chem. Rev.* **2011**, *112*, 869-932.

[123] J. Lee, O. K. Farha, J. Roberts, K. A. Scheidt, S. T. Nguyen, J. T. Hupp, *Chem. Soc. Rev.* **2009**, *38*, 1450-1459.

[124] J. Gascon, U. Aktay, M. D. Hernandez-Alonso, G. P. M. van Klink, F. Kapteijn, *J. Catal.* **2009**, *261*, 75-87.

[125] J. L. C. Rowsell, O. M. Yaghi, *J. Am. Chem. Soc.* **2006**, *128*, 1304-1315.

[126] M. D. Hürlimann, L. Venkataramanan, *J. Magn. Reson.* **2002**, *157*, 31-42.

[127] M. Holz, H. Weingartner, *Journal of Magnetic Resonance (1969)* **1991**, *92*, 115-125.

[128] R. Valiullin, V. Skirda, *J. Chem. Phys.* **2001**, *114*, 452-458.

[129] S. Amirjalayer, R. Schmid, *Microporous Mesoporous Mater.* **2009**, *125*, 90-96.

[130] M. Goldman, L. Shen, *Phys. Rev.* **1966**, *144*, 321.

[131] L. Peschier, J. Bouwstra, J. De Bleyser, H. Junginger, J. Leyte, *J. Magn. Reson.* **1996**, *110*, 150-157.

[132] K. Koh, A. G. Wong-Foy, A. J. Matzger, *Chem. Commun. (Cambridge, U. K.)* **2009**, 6162-6164.

[133] G. Borgia, R. Brown, P. Fantazzini, *J. Magn. Reson.* **1998**, *132*, 65-77.

[134] M. D. Hurlimann, D. D. Griffin, *J. Magn. Reson.* **2000**, *143*, 120-135.

[135] *Robotics,* J-KEM Scientific, **2014**, http://www.jkem.com/robotics

[136] *Prospa Software,* Magritek, **2014**, http://www.magritek.com/products/prospa/

Appendix A
Selected Pulse Sequences and Phase Tables

A.1 Carr-Purcell Meiboom-Gill (CPMG) Pulse Sequence

Note that at low field (13 MHz), the pulses are amplitude modulated, while at high field (300 MHz), the pulses are time modulated.

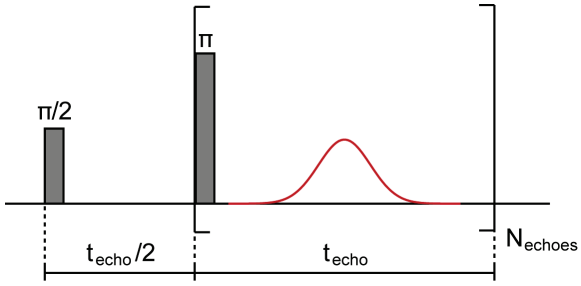

Figure A.1. CPMG pulse sequence, where t_{echo} is the echo time, and N_{echoes} is the number of echoes.

A.2 T_2-T_2 Relaxation Exchange Pulse Sequence

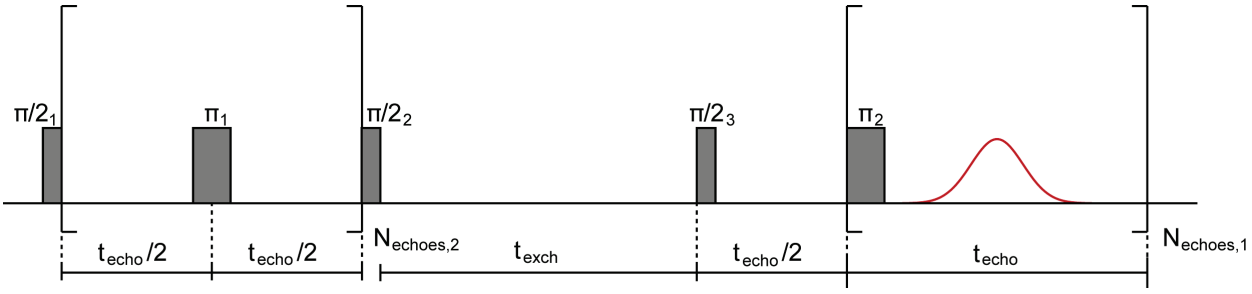

Figure A.2. T_2-T_2 pulse sequence, where t_{echo} is the echo time, t_{exch} is the exchange time and $N_{echoes,1}$ is the number of echoes for the acquisition, and $N_{echoes,2}$ is the number of echoes in the second dimension.

Table A.1. Phase table for T_2-T_2 pulse sequence

$\pi/2_1$	π_1	$\pi/2_2$	$\pi/2_3$	π_2	Acq.
0	1	0	2	1	0
2	1	2	0	1	2
0	1	2	2	1	2
2	1	0	0	1	0
2	3	2	0	3	2
0	3	0	2	3	0
2	3	0	0	3	0
0	3	2	2	3	2
1	0	1	3	0	1
3	0	3	1	0	3
1	0	3	3	0	3
3	0	1	1	0	1
3	2	3	1	2	3
1	2	1	3	2	1
3	2	1	1	2	1
1	2	3	3	2	3

A.3 DEPTH-CPMG

This pulse sequence includes a DEPTH excitation pulse to eliminate background signals.

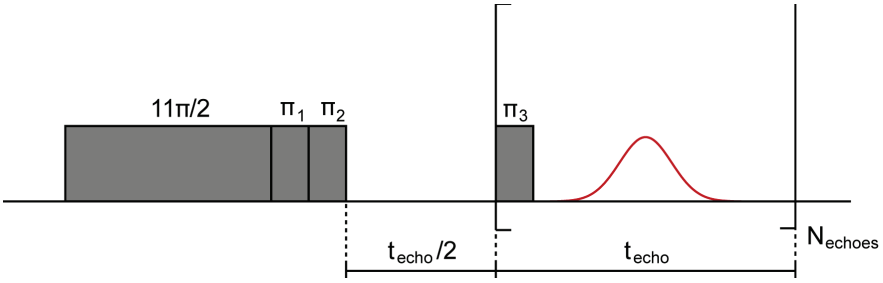

Figure A.3. DEPTH-CPMG pulse sequence, where t_{echo} is the echo time, and N_{echoes} is the number of echoes.

Table A.2. Phase table for DEPTH-CPMG pulse sequence

11π/2	**π1**	**π2**	**π3**	**Acq.**
0	0	3	1	0
0	0	3	3	0
0	1	3	3	2
0	1	3	1	2
0	2	3	1	0
0	2	3	3	0
0	3	3	3	2
0	3	3	1	2

A.4 Stimulated Echo (STE) with CPMG Acquisition

The phase table for this pulse sequence can be obtained in this reference.[126]

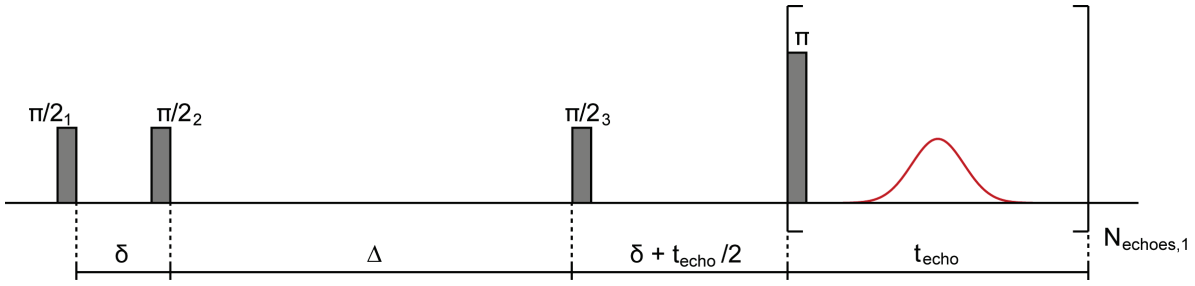

Figure A.4. STE-CPMG pulse sequence, where δ is the time period varied in the second dimension, Δ is the diffusion time, t_{echo} is the echo time, and N_{echoes} is the number of echoes.

Appendix B

Sample Characterization Data for Ex-Situ Relaxometry Study

B.1 X-ray Diffraction Data

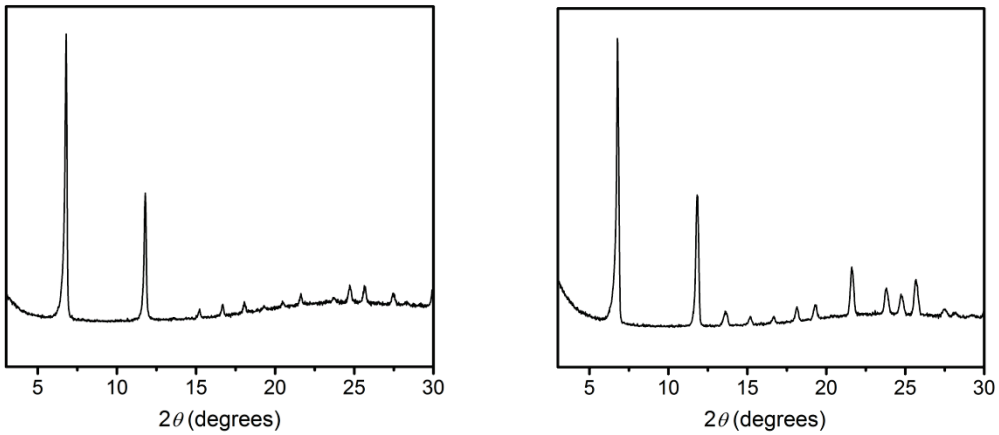

Figure B.1. Powder X-ray diffraction pattern of as-synthesized Mg_2(dobdc) (left) and Zn_2(dobdc) (right).

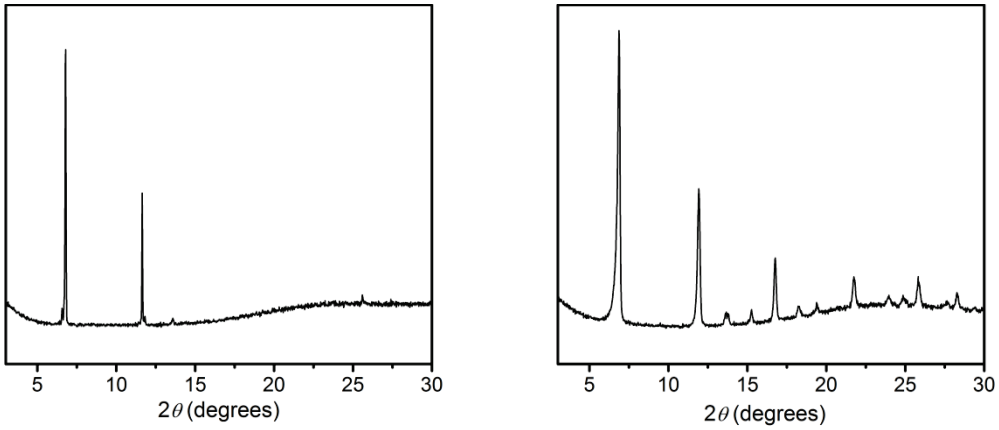

Figure B.2. Powder X-ray diffraction pattern of as-synthesized Co_2(dobdc) (left) and Ni_2(dobdc) (right).

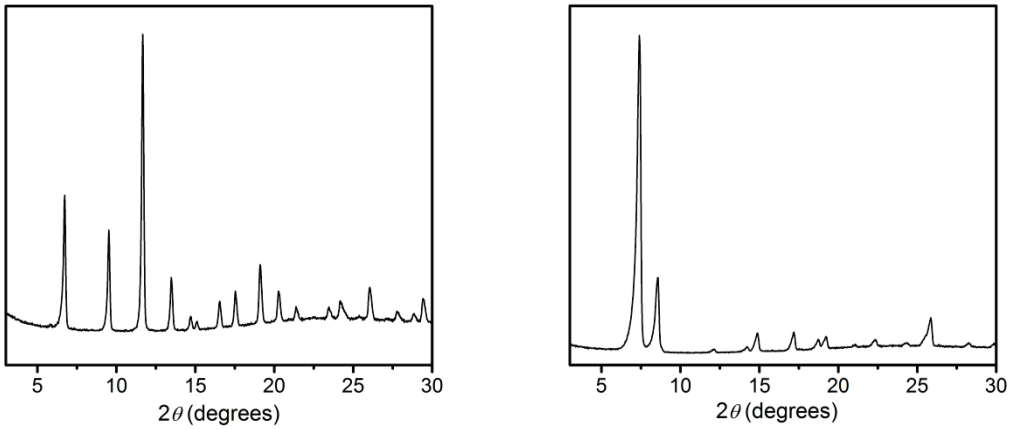

Figure B.3. Powder X-ray diffraction pattern of as-synthesized Cu-HKUST-1 (left) and UiO-66 (right)

B.2 N_2 Adsorption Data

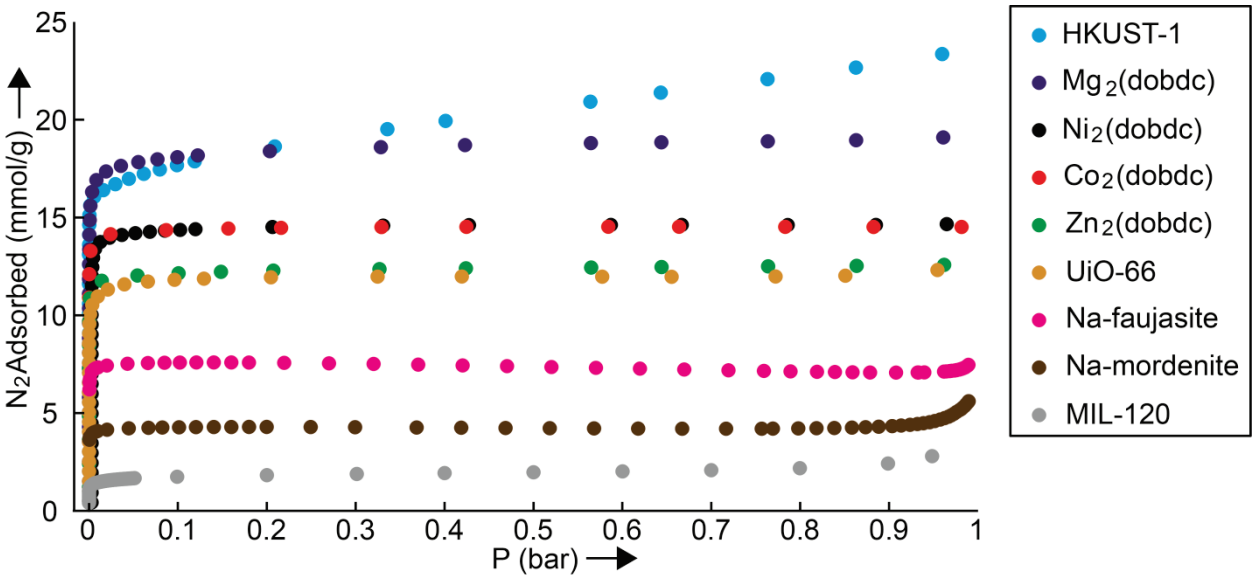

Figure B.4. N_2 adsorption curves taken at 77K for materials tested Chapter 2.

B.3 Thermogravimetric Analysis Data

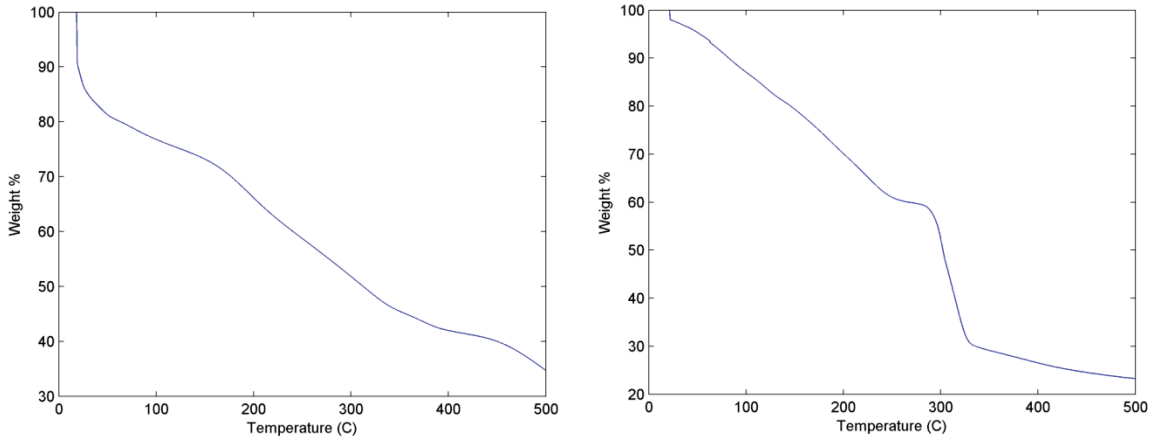

Figure B.5. TGA curve of Mg_2(dobdc) (left) and HKUST-1 (right) loaded with DMF.

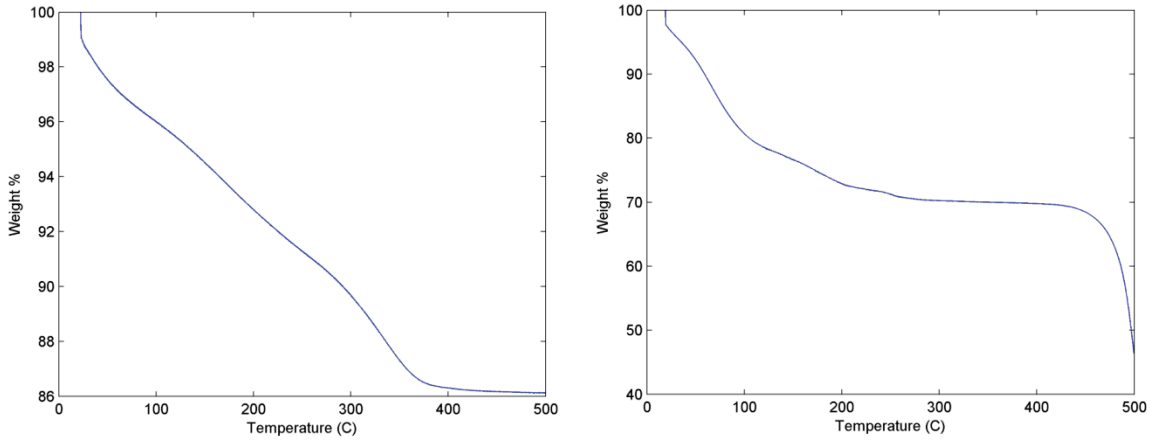

Figure B.6. TGA curve of Na-mordenite (left) and UiO-66 (right) loaded with DMF.

Appendix C

Selected NMR Data and Diffusion Fit Results for Ex-Situ Relaxometry Study

C.1 Selected NMR-MOUSE Data

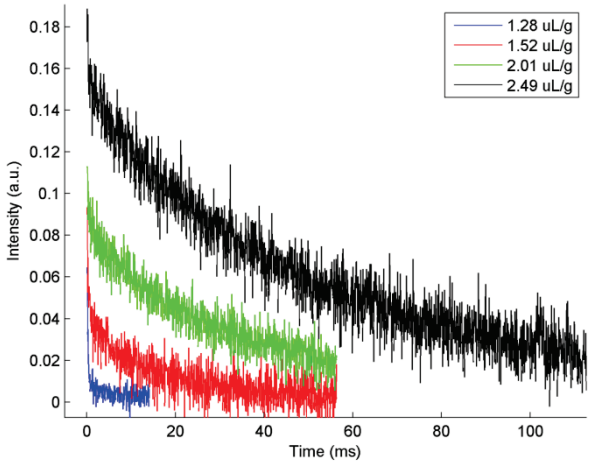

Figure C.1. Raw relaxation data for Mg_2(dobdc) (left).

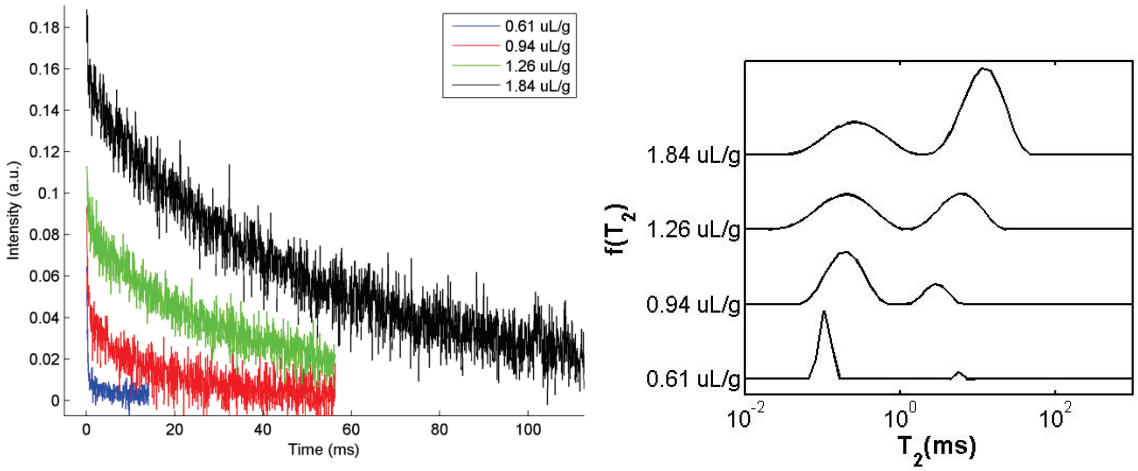

Figure C.2. Raw relaxation data for HKUST-1 loaded with DMF (left) and corresponding relaxation distributions obtained from Laplace inversion (right).

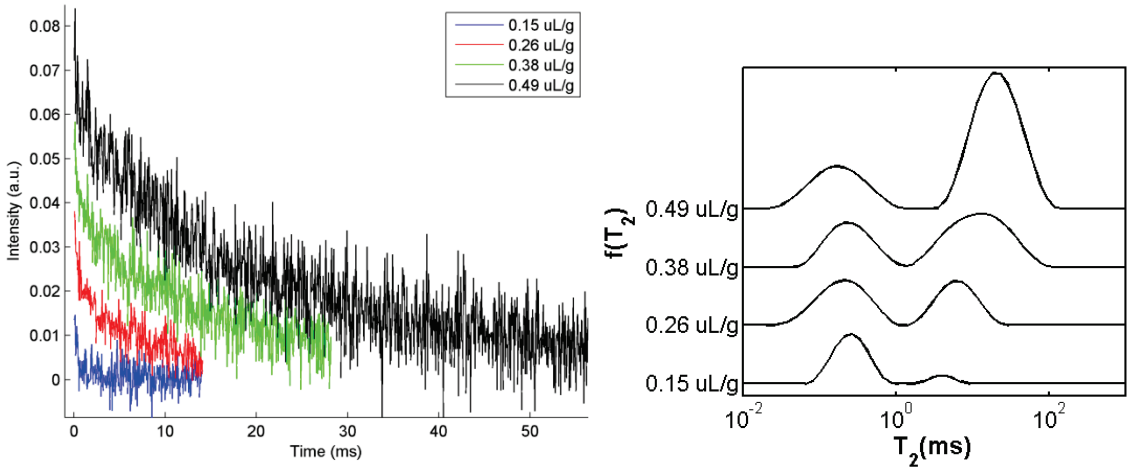

Figure C.3. Raw relaxation data for Na-mordenite loaded with DMF (left) and corresponding relaxation distributions obtained from Laplace inversion (right).

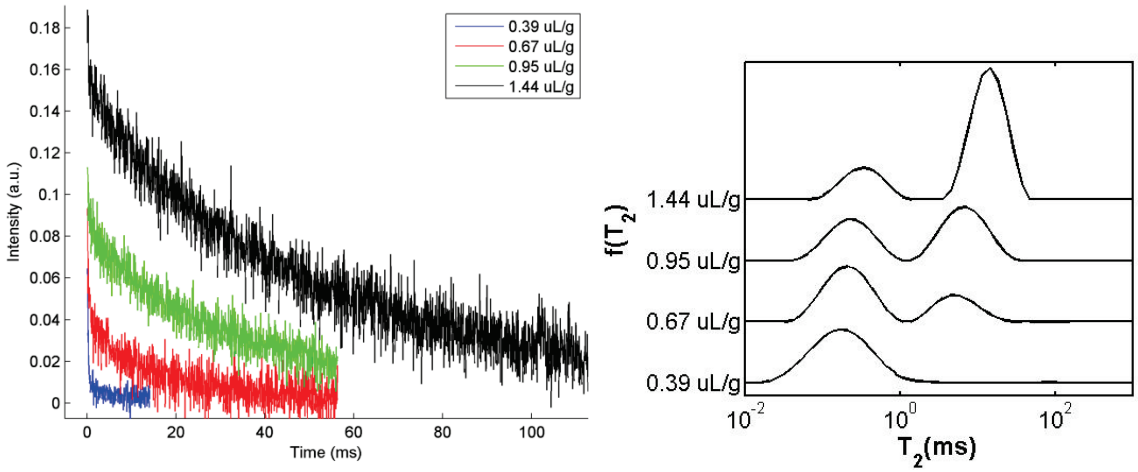

Figure C.4. Raw relaxation data for UiO-66 loaded with DMF (left) and corresponding relaxation distributions obtained from Laplace inversion (right).

C.2 Selected Relaxation Data for Large-Pore Frameworks

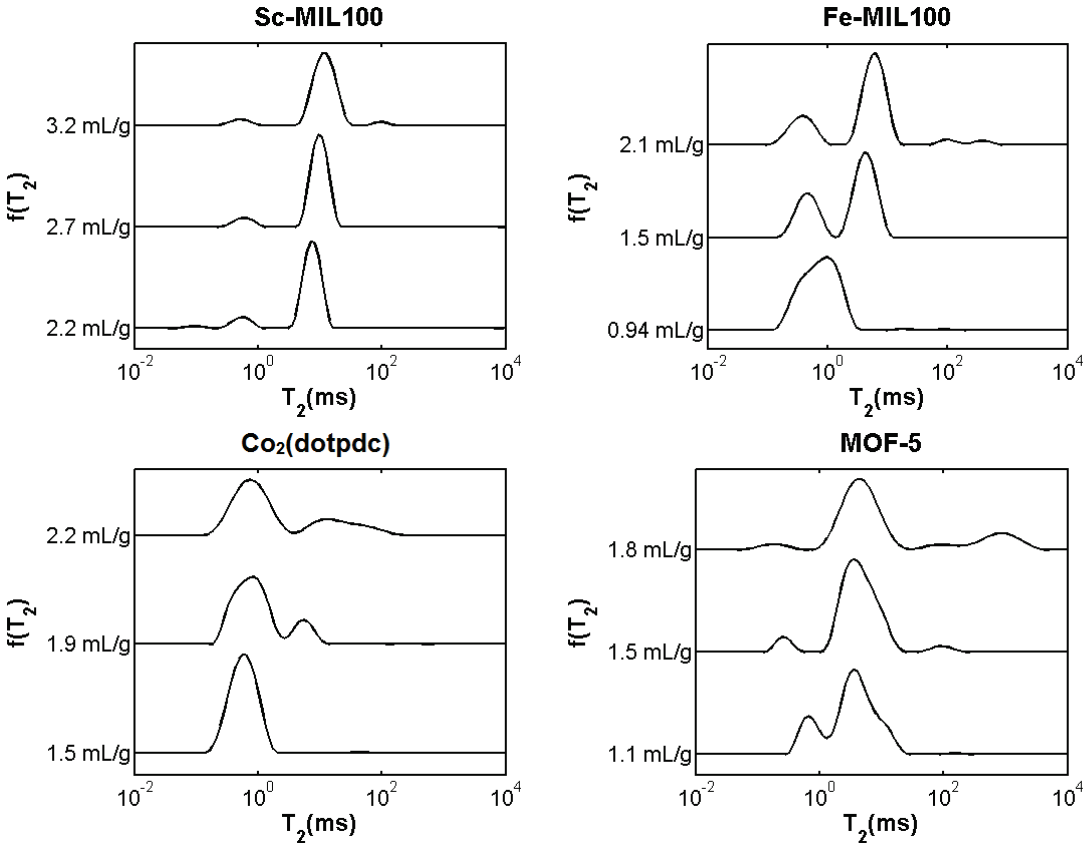

Figure C.5. Relaxation distributions for Sc-MIL100 (top left), Fe-MIL100 (top right), Co_2(dotpdc) (bottom left), and MOF-5 (bottom right).

Appendix D
Model Fitting Results

D.1 NMR-MOUSE Surface Area Correlation

Table D.1. Surface areas from direct analysis of relaxation distributions.

Sample name	BET surface area (m^2g^{-1})	NMR-DMSO surface area (m^2 g^{-1})	NMR-DMSO surface area % error	NMR-DMF surface area (m^2 g^{-1})	NMR-DMF surface area % error
Mg_2(dobdc)	1662	1780 ± 166	+7	1921 ± 152	+16
Zn_2(dobdc)	1133	1297 ± 163	+14	1066 ± 149	-6
Co_2(dobdc)	1347	1240 ± 164	-8	1180 ± 152	-12
Ni_2(dobdc)	1341	962 ± 180	-28	1306 ± 151	-3
HKUST-1	1583	1391 ± 163	-12	1305 ± 150	-18
UiO-66	1084	1132 ± 163	+4	1000 ± 149	-8
Ni-NaX zeolite	774	806 ± 163	+4	814 ± 151	+5
Na-faujasite	714	946 ± 163	+33	845 ± 151	+18
Na-mordenite	398	481 ± 166	+21	600 ± 150	+50

D.2 Kinetic Model Fits for Large-Pore Frameworks

The results of the three-site model fits are shown below in Table D.2. Note that discarded fits, due to $p<0.01$ or due to inconsistent changes in fit values, are highlighted in light grey, while the pore volumes shown in Figure 3.5 are highlighted in dark grey.

Table D.2. Model Fits and predicted NMR pore volumes

Sample Name	Solvent Content (mL/g)	k_{ba} (ms^{-1})	k_{bc} (ms^{-1})	M_a^0	M_b^0	M_c^0	$T_{2,a}$ (ms)	$T_{2,b}$ (ms)	$T_{2,c}$ (ms)	P	Pore Volume [cm^3/g]
Al(OH)(bpydc)	0.75	6.65E-01	8.14E-03	0.83	0.35	0.04	0.33	1511	1802	0.36	0.51
	1.10	3.81E-01	9.15E-03	1.03	0.57	0.07	0.54	2758	2122	0.59	0.68
	1.30	2.74E-01	4.33E-03	1.15	0.89	0.07	0.65	1087	1724	0.04	0.71
	1.60	2.58E-01	1.13E-02	1.16	1.17	0.19	0.78	788	1226	0.02	0.74
	1.89	1.72E-01	5.11E-03	1.37	1.38	0.16	1.27	1251	825	0.02	0.89
	2.14	1.44E-01	5.04E-03	1.56	1.53	0.19	1.72	1678	794	0.03	1.02
	2.40	1.25E-01	6.36E-03	1.72	1.70	0.27	2.13	2825	1140	0.01	1.12
	2.65	9.39E-02	3.79E-03	2.00	1.72	0.30	2.90	2400	813	0.00	1.32
Sc-MIL100	2.21	2.01E-01	4.86E-04	1.13	2.03	0.03	1.23	2754	1003	0.11	0.78
	2.68	1.67E-01	9.89E-04	1.21	2.67	0.11	1.44	847	53	0.10	0.81
	3.16	1.47E-01	8.96E-04	1.63	2.86	0.23	2.56	230	161	0.00	1.09
Fe-MIL100	0.94	8.11E-01	1.11E-03	1.98	0.51	0.02	0.50	2679	3553	0.55	0.75
	1.17	3.82E-01	9.98E-04	2.14	1.26	0.03	0.54	2059	103	0.83	0.73
	1.48	2.91E-01	7.32E-03	2.13	1.93	0.12	0.59	2015	278	0.10	0.75
	1.77	2.54E-01	1.76E-02	2.03	2.68	0.37	0.52	2477	428	0.02	0.71
	2.06	1.73E-01	3.50E-04	2.65	3.03	0.27	0.98	3900	3880	0.00	0.92
Co_2(dotpdc)	1.53	1.23E+00	1.04E-03	3.15	0.63	0.02	0.45	5	3736	0.61	1.52
	1.88	3.14E-01	7.77E-03	3.58	0.80	0.10	0.67	1204	1293	0.03	1.51
	2.23	1.05E-01	9.86E-03	3.73	1.07	0.50	0.81	554	901	0.06	1.57
	2.57	4.71E-02	4.54E-03	3.75	1.58	0.70	0.94	3932	1929	0.00	1.60
MOF-5	1.10	2.68E-01	8.14E-03	1.25	0.78	0.10	1.26	2576	1058	0.04	0.64
	1.49	1.62E-01	2.07E-03	2.27	0.63	0.11	2.81	1954	836	0.45	1.13
	1.84	7.02E-03	9.84E-04	2.64	0.39	0.48	5.10	3845	3312	0.00	1.38

Appendix E
The Laplace Inversion

E.1 Introduction

The 1D Laplace inversion seeks to minimize the mismatch between the acquired data and the summation of prescribed exponential components, as shown below.

$$S_n(t) = \sum_k C_k e^{-t_n/T_k} + \varepsilon_n \tag{E.1}$$

$$\min \left[\sum_{n=1}^{N} \left(S_n(t) - \sum_{j=1}^{M} C_j e^{-t_n/T_j} \right)^2 + \alpha^{-2} f'' \right] \tag{E.2}$$

Equation E.1 describes S_n, the acquired NMR signal at time t_n composed of various exponential components with relaxation times T_k and weights C_k, added to any experimental noise ε. In Equation E.2, for N time points, the data are fitted with M exponential components with relaxation times T_j and weights C_j to minimize the least-squares error χ^2, generating a spectrum of relaxation components. Due to experimental error and the number of fitting parameters, this least-squares minimization is ill-posed.[99, 133] Regularization constrains the set of possible solutions such that the solution must be smooth. An additional constraint f'', a numerical estimation for the second derivative of the solution spectrum, is added and weighted by the smoothing parameter α. Thus, minimization of the magnitude of the second derivative produces smoothly-varying spectra. The parameter α exhibits a large effect on the resulting exponential spectra and is chosen by a process called the L-curve that balances the degree of smoothing with the squared error. In general, overly small values of α enforce the smoothing constraint at the

expense of fitting the data, while overly large values of α fit the data too closely, increasing the effect of noise. Thus, the proper selection of α extracts maximum information while rejecting the effects of experimental noise. Lower signal-to-noise necessitates smaller α (greater smoothing), coarsening the spectra and limiting the resolution of different relaxation populations.

Note that the choice of an exponential function containing the term $t/T_{2,j}$ in Equation E.2, called the "kernel," can be modified to yield an inversion of other parameters, such as T_1 or the diffusion coefficient D.

Two-dimensional Laplace inversions operate very similarly to those for a single dimension, though the computation of such inversions is typically very computationally intensive. These 2D inversions allow for correlation and exchange maps to be generated from T_1-T_2, T_2-T_2, and D-T_2 experiments, provided the appropriate kernels for the direct and indirect dimensions in each experiment.

E.2 Artifacts and Interpretation

The 1D and 2D distributions obtained from Laplace inversions must be treated with a high level of scrutiny and skepticism, as the maps present only one of many possible distributions that are completely equivalent with respect to the residual. In other words, the fine details of any distribution should not be overanalyzed. Only with repeated measurements can confidence be established in a given distribution; it is good practice to repeat the same experiment multiple times and compare the inversions to ensure that small features are repeatable. It is also good practice to investigate the behavior of the distribution as the smoothing parameter is changed, even when an optimal value can be obtained from an L-curve. Note that there are also many other ways to choose an optimal smoothing value; the L-curve method is merely an easily implemented choice.

The distributions are also extremely sensitive to initial amplitude fluctuations in a CPMG train as well as DC offsets. The latter often presents itself as a distribution that does not fall to zero at long time constants. In other words, the inversion accounts for the DC offset with an "infinite" decay time. Such artifacts are usually small, given a small DC offset. However, with fluctuations in CPMG intensity near $t = 0$, the artifacts generated can be enormous, as the inversion may sense a very short decay time. These distributions do not fall to zero at short time constants, and can dominate the distribution. Since fluctuations in the first few echoes of a CPMG are well established phenomena caused by a multitude of reasons (pulse length error, pulse shape error, offset error, inhomogeneous B_1, inhomogeneous B_0, to name a few),[134] omission of the first few echoes is common to allow for the elimination of artifacts. However, if

investigating fast decays that disappear within the first few echoes, this can be a major disadvantage.

Appendix F
NMR-MOUSE Automation

F.1 Eclipse Workstation

To realize the high-throughput aspect of the NMR porosity screening technique, the single sided NMR-MOUSE magnet was combined with a J-KEM Eclipse robotic workstation to provide sample handling.[135] The Eclipse includes a robot arm with high-fidelity x/y/z-axis motors and a fine pneumatic gripper at the end of the arm to pick and place vials on the NMR-MOUSE from a 96-well plate.

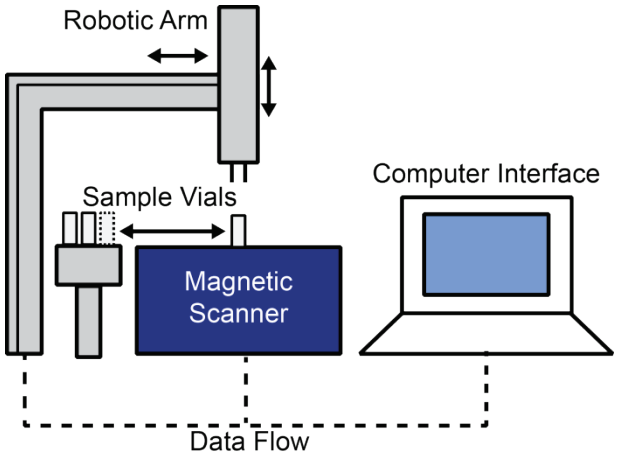

Figure F.1. Schematic of NMR-MOUSE equipped with automation hardware. The spectrometer is not picture, but communicates with the scanner and computer as well.

A software module provided by J-KEM interfaces with the workstation via a USB port. This program enables the loading of vials from the 96-well plate in any order specified by a spreadsheet of vial numbers and also allows for manual movement and position calibration. Additional command sequences can be programmed in by the user to enhance future flexibility.

The vial order is loaded from a "sequence file" that contains a column of vial numbers saved in CSV format. The row of the table indicates the experiment number while the value in the table indicates the vial to be tested. The vial number in the 96-well plate is ordered from left-to-right and top-to-bottom (i.e. top left is 1 and bottom right is 96). More information about the sequence file will be detailed in the next section.

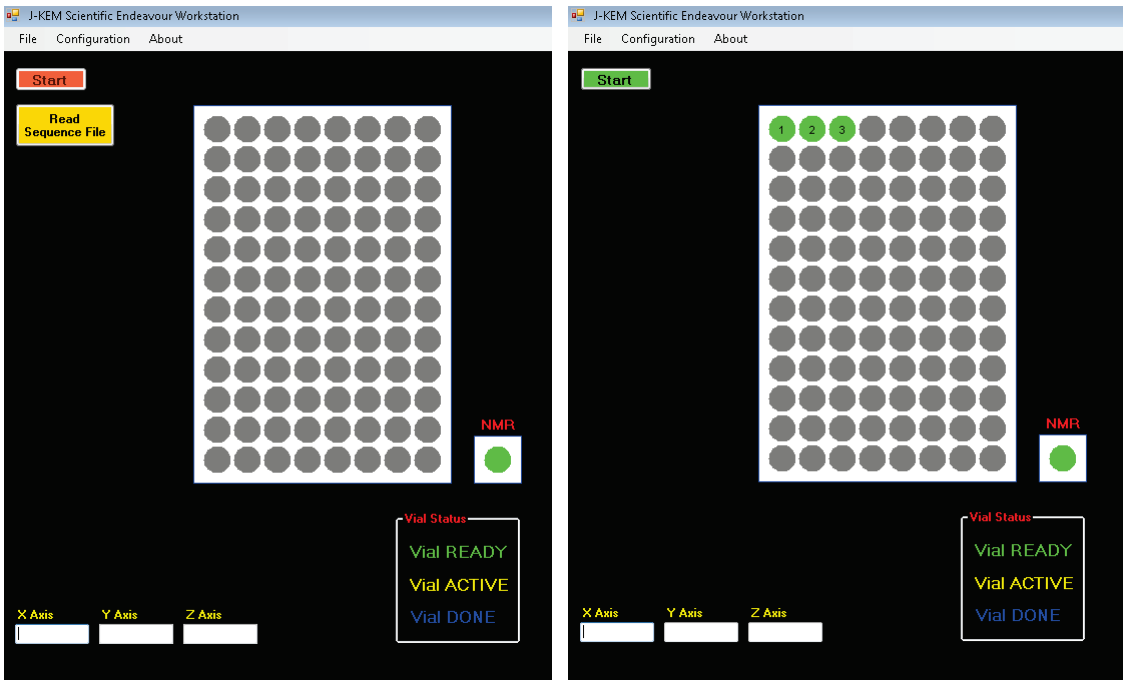

Figure F.2. Screenshots of software for Eclipse workstation. Upon opening the executable file with the name "J-KEM Robot," the user will be prompted to upload an experiment sequence file (left). After loading the sequence CSV file, the program will show the numbers for each vial position indicates the order that the vials will be placed on the NMR-MOUSE (right). The circle colors green, yellow, and blue indicate samples that have yet to be tested, that are currently being tested, and that have already been tested.

To minimize distortion of the magnetic field and experimental noise, the design includes a plastic base, and the robotic motors, which emit RF noise, are located as far away from the magnet as possible. Also, during NMR experiments, the motors in the robotic arm are turned off, further reducing the noise.

Note that the x/y/z positions of every well in the 96-well plate as well as the sample location on the NMR-MOUSE have been configured previously. To adjust these positions manually, the configuration drop down window contains a command to calibrate the positions. It is encouraged that the calibration be done with the support of J-KEM. Also, the gripper operates off of house air; loss of pressure will disable the gripper. Finally, the setup also includes an emergency stop button that will halt all robot motion. Contact J-KEM (http://www.jkem.com/contact/) if this button has been pressed to reactivate the workstation.

F.2 Automation Algorithm and Autosample Prospa Program

In addition to automated sample handling, software modules for automated NMR measurements have been created to measure proton relaxation in concert with automated sample handling. These programs have been written in Prospa v3.11, the software package that operates the Kea II spectrometer.[136] To integrate sample handling with the NMR experiments, TTL pulses are sent from the spectrometer to the control box of the Eclipse workstation via an RS-232 cable. To place a vial on the NMR-MOUSE, a 5V DC pulse is sent from pin 2 from the spectrometer to the workstation. To remove a vial, a similar DC pulse is sent from pin 3.

The TTL commands are incorporated into a Prospa program called Autosample. This program runs a T_1 saturation recovery with a CPMG acquisition followed by a T_2 CPMG pulse program with parameters optimized for the surface coil on the NMR-MOUSE. These parameters are coded into the program and thus, to change these parameters, the user must use the text editor in Prospa to change them.

Table F.1. Default parameters for the experiments by Autosample

Parameter	**Value**
B_1 Frequency	13.099 MHz
Dwell Time	0.5 μs
Echo Time	55 μs
Echo Shift	1 μs
Number of Acquisition Points per Echo	8
Pulse Length	2.4 μs
Number of Summed Echoes (T_1 only)	8
Repetition Time (T_1 only)	200 ms

However, the Autosample program does allow the user to adjust certain parameters for the T_1 and T_2 experiments that are sample-dependent. They are as follows: a guess for the T_1 value, the maximum T_1 delay time, the number of delays for the T_1 experiment, the number of scans in the

T_1 experiment the repetition or last delay time for the CPMG experiment, the number of echoes in the CPMG experiment, and the number of scans for the CPMG experiment. These values must be input in the same sequence file that is read by the Eclipse workstation.

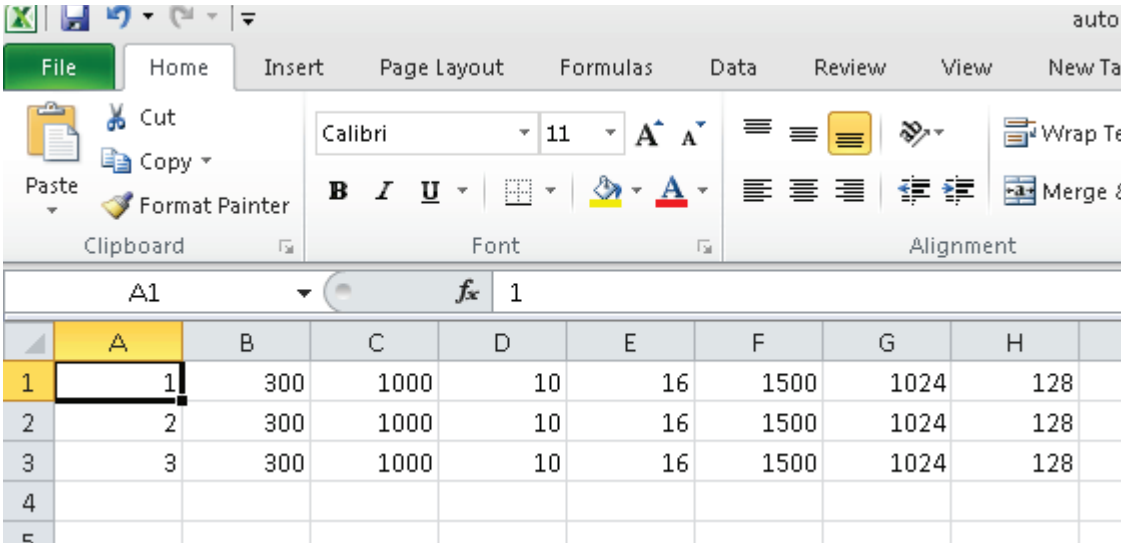

	A	B	C	D	E	F	G	H
1	1	300	1000	10	16	1500	1024	128
2	2	300	1000	10	16	1500	1024	128
3	3	300	1000	10	16	1500	1024	128
4								

Figure F.3. A sample sequence file. The file contains information about the vial number and NMR experimental parameters, but does not include a heading due to lack of compatibility with the programs reading the file. The data for each column is as follows from left to right: column A is the vial number, column B is the T_1 guess (ms), column C is the maximum T_1 delay time (ms), column D is the number of T_1 delays, column E is the number of scans for the T_1 experiment, column F is repetition time for the T_2 experiment (ms), column G is the number of echoes in the T_2 experiment, and column H is the number of scans for the T_2 experiment.

Autosample reads NMR experimental parameters from the sequence file automatically when the Autosample program is run. The user interface allows the user to choose the number of sample to run and the folder number to which the data will be saved (only the first number is shown, and consecutive experiments will be incremented accordingly). Changing the working directory will change where the experimental data will be saved, and the experiment name creates a dummy folder that is necessary for the program to function, but serves no other use. After the experiments are finished, the data is saved in the working directory under the folder names “T1” and “cpmg_fast.”

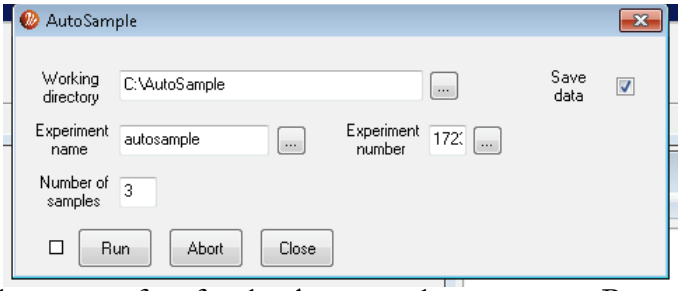

Figure F.4. Graphical user interface for the Autosample program in Prospa.

In summary, to run an automated series of T_1 and T_2 experiments, one must follow these steps (it is assumed that the spectrometer is turned on and ready):

1. Place samples in known positions in the 96-well plate.
2. Create a sequence file with desired vial numbers to be tested and NMR experimental parameters.
3. Turn on the robot control box.
4. Open the J-KEM Robot program and upload the sequence file.
5. After loading the sequence file, press start to ready the robot workstation. The robot will "click" and home the robot arm.
6. Open Prospa and open the Autosample program.
7. Input the total number of experiments to be run as well as the desired folder number to which the data will be saved.
8. Press run on the Autosample GUI to run all experiments.

To abort the experiment, both Autosample and J-KEM Robot programs must be stopped independently.

Appendix G
Kinetic Models and MATLAB Code

G.1 Bloch-Torrey Model for Investigating Relaxation Distributions

The conservation equation, boundary conditions, and initial conditions for the transverse magnetization ($M_{xy}= M_x + iM_y$) can be written according to equations below.

$$\frac{\partial M_{xy}}{\partial t} = \frac{D_{pore/bulk}}{r^2}\frac{\partial}{\partial r}\left(r^2 M_{xy}\right) - \frac{M_{xy}}{T_{2,pore/bulk}} \tag{G.1}$$

$$\left.\frac{\partial M_{xy}}{\partial r}\right|_{r=0} = 0 \tag{G.2}$$

$$\left. M_{xy}\right|_{r=0} < \infty \tag{G.3}$$

$$\left[\left. M_{xy}\right|_{r=R_1^-} - \left. M_{xy}\right|_{r=R_1^+}\right] = \left[\left(D_{pore}\frac{\partial M_{xy}}{\partial r}\right)\right|_{r=R_1^-} - \left.\left(D_{bulk}\frac{\partial M_{xy}}{\partial r}\right)\right|_{r=R_1^+}\Bigg] = 0 \tag{G.4}$$

$$M_{xy}(t=0) = M_{xy,0} \tag{G.5}$$

In these equations, M represents the density of magnetization, $D_{\text{pore/bulk}}$ represents the solvent diffusion coefficient inside the particle or in the inter-particle film, and $T_{2,pore/bulk}$ represents the volumetric relaxation time of either the particle or the inter-particle film.

G.2 Two-Site Kinetic Model

The equations below describe a two-site kinetic model for simultaneous relaxation and exchange.

$$\frac{\partial M_a}{\partial t} = -r_a M_a - k_{ab} M_a + k_{ba} M_b \quad \text{G.6}$$

$$\frac{\partial M_b}{\partial t} = -r_b M_b - k_{ba} M_b + k_{ab} M_a \quad \text{G.7}$$

$$M_{a,b}(t=0) = M_{a,b}^0 \quad \text{G.8}$$

Note that there exists only a single independent exchange coefficient due to mass balance at equilibrium in the absence of relaxation. The analytical solution for these equations given a time interval t = (0,t) can be easily obtained using Mathematica, which allows for implementation into MATLAB as function for data fitting. This solution will be described in the Appendix G.3. For T_2-T_2 experiments, which consist of three time intervals, an analytical solution is available in literature.[47]

G.3 MATLAB Code for Two-Site Kinetic Model Fits

The function for evaluating the decay due to simultaneous relaxation and decay for two sites is shown below. The input arguments are the relaxation times, the exchange rates, and the experimental intensity and time data.

```
function out = twosite1D(varin,decay,tspan)
%% Assign variables
kb = varin(1);
Ma0 = varin(2);
Mb0 = varin(3);
t2a = varin(4);
t2b = varin(5);
ra = 1/t2a;
rb = 1/t2b;
ka = kb*Mb0/Ma0;
```

```
b = (ka+kb+ra+rb);
c = (kb*ra+ka*rb+ra*rb);
det = sqrt(b^2-4*c);

%% Use exact solution and output cost function
M1out = (exp(1/2*(-b-det)*tspan)*ka*Ma0-...
    exp(1/2*(-b+det)*tspan)*ka*Ma0-...
    exp(1/2*(-b-det)*tspan)*kb*Ma0+...
    exp(1/2*(-b+det)*tspan)*kb*Ma0-...
    2*exp(1/2*(-b-det)*tspan)*kb*Mb0+...
    2*exp(1/2*(-b+det)*tspan)*kb*Mb0+...
    exp(1/2*(-b-det)*tspan)*Ma0*ra-...
    exp(1/2*(-b+det)*tspan)*Ma0*ra-...
    exp(1/2*(-b-det)*tspan)*Ma0*rb+...
    exp(1/2*(-b+det)*tspan)*Ma0*rb+...
    exp(1/2*(-b-det)*tspan)*Ma0*det+...
    exp(1/2*(-b+det)*tspan)*Ma0*det)/(2*det);
M2out = (-2*exp(1/2*(-b-det)*tspan)*ka*Ma0+...
    2*exp(1/2*(-b+det)*tspan)*ka*Ma0-...
    exp(1/2*(-b-det)*tspan)*ka*Mb0+...
    exp(1/2*(-b+det)*tspan)*ka*Mb0+...
    exp(1/2*(-b-det)*tspan)*kb*Mb0-...
    exp(1/2*(-b+det)*tspan)*kb*Mb0-...
    exp(1/2*(-b-det)*tspan)*Mb0*ra+...
    exp(1/2*(-b+det)*tspan)*Mb0*ra+...
    exp(1/2*(-b-det)*tspan)*Mb0*rb-...
    exp(1/2*(-b+det)*tspan)*Mb0*rb+...
    exp(1/2*(-b-det)*tspan)*Mb0*det+...
    exp(1/2*(-b+det)*tspan)*Mb0*det)/(2*det);
out = (M1out + M2out)-decay;
```

To fit this function to a CPMG decay, an argument for a vector of experimental data is included. The output of the function should then be the cost function relevant for the optimization function, which in this case is the vector of residuals. The function for optimizing the fit is shown below. The program imports data from any folder contained in another specified folder (C:\\mousedata). This data must have a specific format (data.csv) with time, real, and imaginary data in column form. The function is also run in debugging mode and not as a function call from the command window. The output is saved to the current directory as an Excel file.

```
clear
%% Scan directory for folder names

filedata = struct2cell(dir('C:\\mousedata'));
foldername = filedata(1,3:length(filedata(1,:)));
n = length(foldername);
```

```
%% Read data and store as variables

for j = 1:n
            fid1 =
            fopen(horzcat('C:\\mousedata\',char(foldername(j)),'\data.csv'));
            rawdata = textscan(fid1,'%n %n %n','Delimiter',',');

            data = cell2mat(rawdata);

            %Phase data
            exit = 0;
            ph = 1;
            realph = data(:,2);
            imagph = data(:,3);
            while abs(ph) > 0.01 && exit < 9
                cfun = fit(realph,imagph,'poly1');
                coeff = coeffvalues(cfun);
                if realph(1)<0
                    ph = -atan(coeff(1))+pi
                else
                    ph = -atan(coeff(1))
                end
                y = realph + 1i*imagph;
                y = y*exp(1i.*ph);
                realph = real(y);
                imagph = imag(y);
                exit = exit + 1;
            end
            Taudata{j} = data(:,1);
            Realdata{j} = realph;
            Imagdata{j} = imagph;

end
fclose('all');

%% Initialize fit parameters
kout = zeros(1,n);
kerr = zeros(1,n);
Maout = zeros(1,n);
Maerr = zeros(1,n);
Mbout = zeros(1,n);
Mberr = zeros(1,n);
t2pore = zeros(1,n);
t2poreerr = zeros(1,n);
t2bulk = zeros(1,n);
t2bulkerr = zeros(1,n);
pvalue = zeros(1,n);
resid = cell(1,n);
options = optimset;
options.MaxFunEvals = 1000;
```

```
options.TolFun = 1e-18;
m = 5;
var = cell(m,1);
J = cell(m,1);
resid = cell(m,1);
fval = zeros(1,m);
pvalmin = zeros(1,m);

%% Fit 2-site model (4 parameter fit)
for k = 1:n
    tic

    %Initialize starting point and bounds
    noiselevel(k) = std(Imagdata{k});
    SNR = max(Realdata{k})/noiselevel(k);
    time = Taudata{k};
    decay = Realdata{k};

    ub = [10,2*max(decay),2*max(decay),50,350]; %Assume time units of ms
    lb = [0,0,0,0,0];

    %Randomize starting points
    disp(['Now analyzing ',foldername(k)])

    %Fit using nonlinear least squares for each starting point
    for startpt = 1:m
        st = zeros(1,length(lb));
        st(1) = ub(1)*rand(1);
        st(2) = ub(2)*rand(1);
        st(3) = ub(3)*rand(1);
        st(4) = ub(4)*rand(1);
        st(5) = ub(5)*rand(1);

        [var{startpt}, fval(startpt),resid{startpt},~,~,~,J{startpt}] =
        lsqnonlin('twosite1D',st,lb,ub,options,decay',time');
    end

    %Find optimal solution based on minimum residual
    [~,I]=min(fval)
    varout = var{I};

    %Caculate confidence intervals
    ci = nlparci(varout,resid{I},'jacobian',J{I},'alpha',(1-0.683))';
    dev = ci(1,:)-varout;
    resid2{k} = resid{I};

    %Output
    [R,P] = corrcoef([time,resid{I}']);
    outvec{k} = [varout,dev,P(1,2)];
```

```
    toc
end
xlswrite('data.xls',foldername','fitparam','A2')
xlswrite('data.xls',cell2mat(outvec'),'fitparam','B2');
xlswrite('data.xls',{'Folder','k (1/ms)','Pore fraction','T2 pore','M
total',...
    'k err','x err','T2 err','M err','P value'},'fitparam','A1')
```

G.4 Three-Site Kinetic Model

The equations below describe a three-site kinetic model for simultaneous relaxation exchange. This model is the more general model from which the model in Chapter 3.4.2 is derived.

$$\frac{\partial M_a}{\partial t} = -r_a M_a - k_{ab} M_a - k_{ac} M_a + k_{ba} M_b + k_{ca} M_c \qquad \text{G.9}$$

$$\frac{\partial M_b}{\partial t} = -r_b M_b - k_{ba} M_b - k_{bc} M_b + k_{ab} M_a + k_{cb} M_c \qquad \text{G.10}$$

$$\frac{\partial M_c}{\partial t} = -r_c M_c - k_{ca} M_c - k_{cb} M_c + k_{ba} M_a + k_{bc} M_b \qquad \text{G.11}$$

$$M_{a,b,c}(t=0) = M^0_{a,b,c} \qquad \text{G.12}$$

Note that there exists only a four independent exchange coefficients due to mass balance at equilibrium in the absence of relaxation. No analytical solution exists for this set of equations. However, an algebraic solution can be obtained using Mathematica; this greatly increases the speed of numerical calculation compared to a differential equation solver. This algebraic solution for a single time interval t = (0,t) is included in Appendix G.5. The code can be modified to include the three time segments found in a T_2-T_2 exchange experiment.

G.5 MATLAB Code for 1-D Three-Site Kinetic Model Fits

The function for evaluating the decay due to simultaneous relaxation and decay for three sites is shown below. The input arguments are the relaxation times, the exchange rates, and the experimental intensity and time data. Note that the notation is changed from Appendix G.4 from a, b, and c to 1, 2, and 3, respectively. The program to optimize the fit to the data is similar to that shown in Appendix G.3.

```
function out = threesite1Dfit(varin,decay,tspan)

k12 = varin(1);
k23 = varin(2);
k31 = varin(3);
k13 = varin(4);
M1i = varin(5);
M2i = varin(6);
M3i = varin(7);
t2a = varin(8);
t2b = varin(9);
t2c = varin(10;

M1i = ma;          %define!
M2i = mb;
M3i = mc;
r1 = 1/t2a;      %define!
r2 = 1/t2b;
r3 = 1/t2c;       %define!

k21 = ((k12 + k13)*M1i-k31*M3i)/M2i;
k32 = ((k21 + k23)*M2i-k12*M1i)/M3i;

%%Algebraic Solution
Mfactors(4) = k21*((k31+k32)*r1+(k13+r1)*r3)+k23*(k31*r1+(k12+k13+r1)*r3)+...
    r2*(k31*r1+(k13+r1)*(k32+r3)+k12*(k31+k32+r3));
Mfactors(3) = k23*k31 + k23*r1 + k31*r1 + k32*r1 + k31*r2 + k32*r2 +...
    r1*r2 + (k23 + r1 + r2)*r3 + k21*(k31 + k32 + r1 + r3) + ...
    k13*(k21 + k23 + k32 + r2 + r3) + k12*(k23 + k31 + k32 + r2 + r3);
Mfactors(2) = k12+k13+k21+k23+k31+k32+r1+r2+r3;
Mfactors(1) = 1;
Mroots = (roots(Mfactors));
Mdenom = k23*k31 + k23*r1 + k31*r1 + k32*r1 + k31*r2 + k32*r2 + r1*r2 + ...
    k23*r3 + r1*r3 + r2*r3+...
    2*(k23+k31+k32+r1+r2+r3)*Mroots*ones(size(tspan))+...

3*Mroots.^2*ones(size(tspan))+k21*(k31+k32+r1+r3+2*Mroots*ones(size(tspan)))+
...
    k13*(k21+k23+k32+r2+r3+2*Mroots*ones(size(tspan)))+...
```

```
    k12*(k23+k31+k32+r2+r3+2*Mroots*ones(size(tspan)));

M1_M1i =
M1i*sum(exp(Mroots*tspan).*(k23*(k31+r3+Mroots*ones(size(tspan)))+...
 k21*(k31+k32+r3+Mroots*ones(size(tspan)))+(r2+Mroots*ones(size(tspan))).*...
    (k31+k32+r3+Mroots*ones(size(tspan))))./Mdenom);

M1_M2i =
M2i*sum(exp(Mroots*tspan).*(k23*k31+k21*(k31+k32+r3+Mroots*ones(size(tspan)))
)./Mdenom);

M1_M3i =
M3i*sum(exp(Mroots*tspan).*(k21*(k31+k32)+k31*(k23+r2+Mroots*ones(size(tspan)
))))./Mdenom);
M1out = M1_M1i+M1_M2i+M1_M3i;

M2_M1i =
M1i*sum(exp(Mroots*tspan).*(k13*k32+k12*(k31+k32+r3+Mroots*ones(size(tspan)))
)./Mdenom);

M2_M2i =
M2i*sum(exp(Mroots*tspan).*(k13*(k32+r3+Mroots*ones(size(tspan)))+...
k12*(k31+k32+r3+Mroots*ones(size(tspan)))+(r1+Mroots*ones(size(tspan))).*...
    (k31+k32+r3+Mroots*ones(size(tspan))))./Mdenom);

M2_M3i =
M3i*sum(exp(Mroots*tspan).*(k12*(k31+k32)+k32*(k13+r1+Mroots*ones(size(tspan)
))))./Mdenom);
M2out = M2_M1i+M2_M2i+M2_M3i;

M3_M1i =
M1i*sum(exp(Mroots*tspan).*(k12*k23+k13*(k21+k23+r2+Mroots*ones(size(tspan)))
)./Mdenom);

M3_M2i =
M2i*sum(exp(Mroots*tspan).*(k13*(k21+k23)+k23*(k12+r1+Mroots*ones(size(tspan)
))))./Mdenom);

M3_M3i =
M3i*sum(exp(Mroots*tspan).*(k12*(k23+r2+Mroots*ones(size(tspan)))+...
(k13+r1+Mroots*ones(size(tspan))).*(k21+k23+r2+Mroots*ones(size(tspan))))./Md
enom);
M3out = M3_M1i+M3_M2i+M3_M3i;

Mout = M1out+M2out+M3out;

%% Output cost function
out = (Mout-decay);
```

Appendix H
Selected Data and Fits for Diffusion Studies

H.1 Selected Diffusion Decays

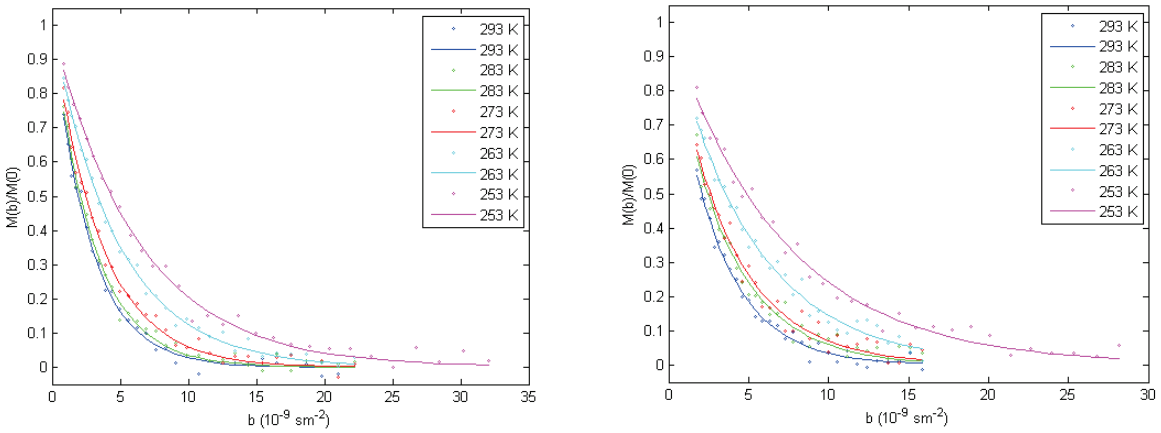

Figure H.1. Diffusion decays for *p*-xylene in MOF-5 at a loading of 64 molecules per unit cell for a diffusion time Δ of 25 ms (left) and 50 ms (right).

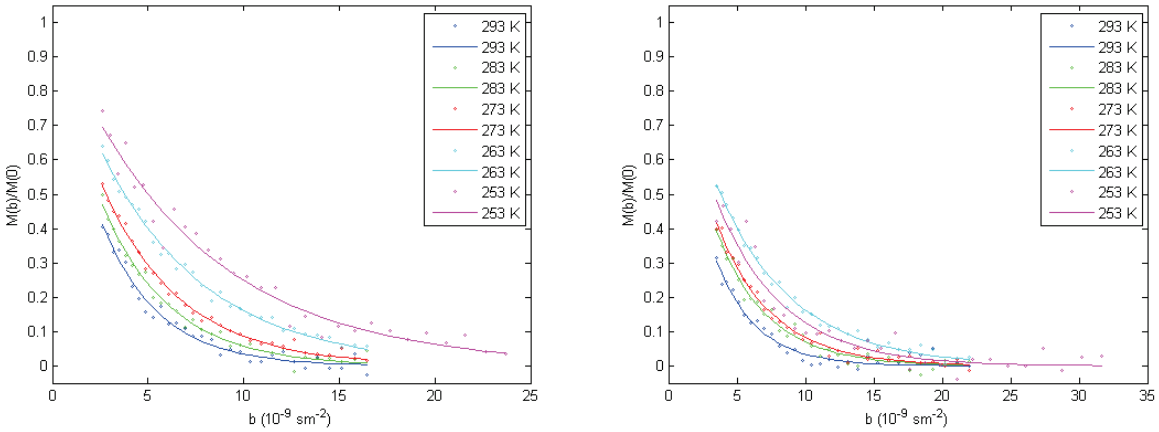

Figure H.2. Diffusion decays for *p*-xylene in MOF-5 at a loading of 64 molecules per unit cell for a diffusion time Δ of 75 ms (left) and 100 ms (right).

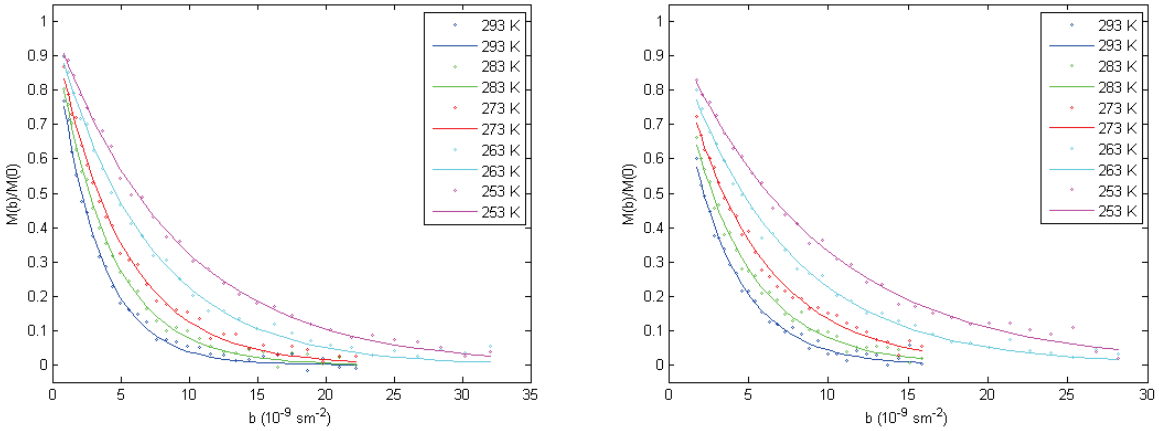

Figure H.3. Diffusion decays for *p*-xylene in MOF-5 at a loading of 49 molecules per unit cell for a diffusion time Δ of 25 ms (left) and 50 ms (right).

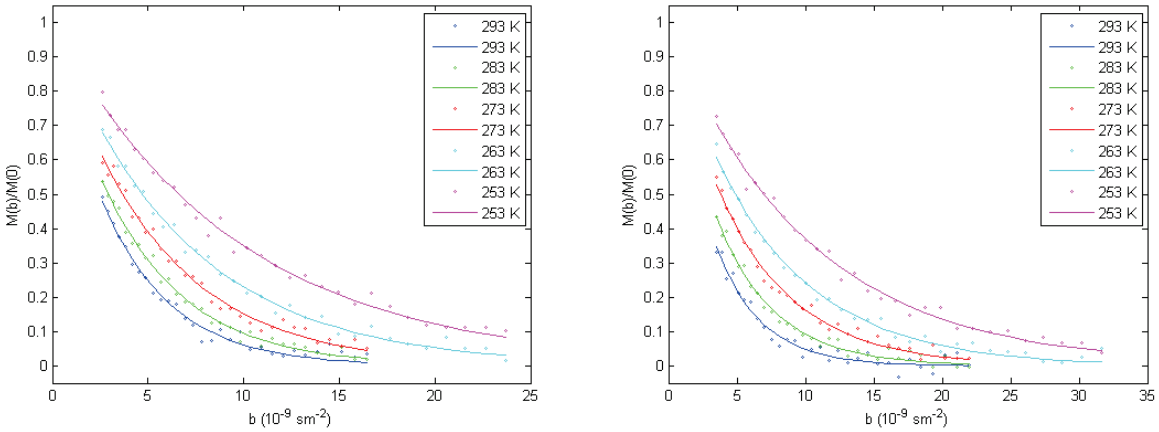

Figure H.4. Diffusion decays for *p*-xylene in MOF-5 at a loading of 49 molecules per unit cell for a diffusion time Δ of 75 ms (left) and 100 ms (right).

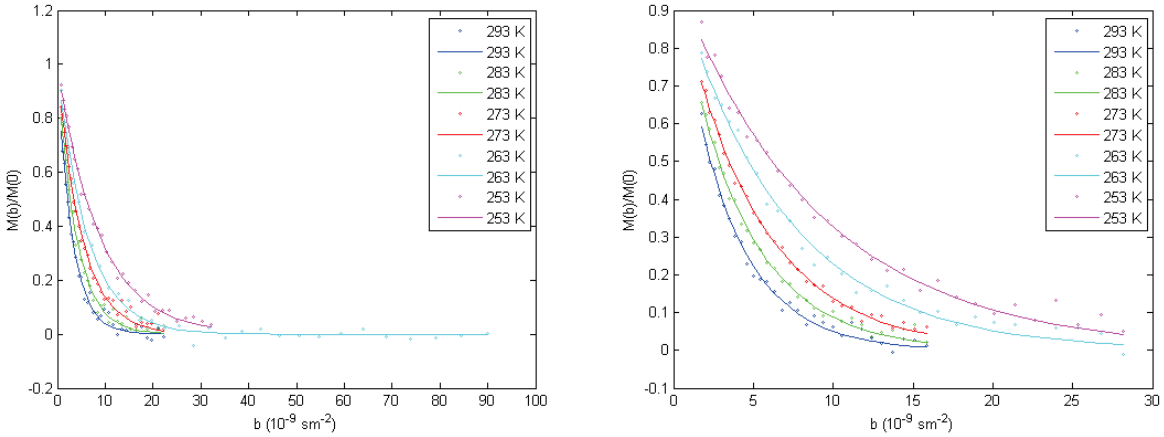

Figure H.5. Diffusion decays for *p*-xylene in MOF-5 at a loading of 39 molecules per unit cell for a diffusion time Δ of 25 ms (left) and 50 ms (right).

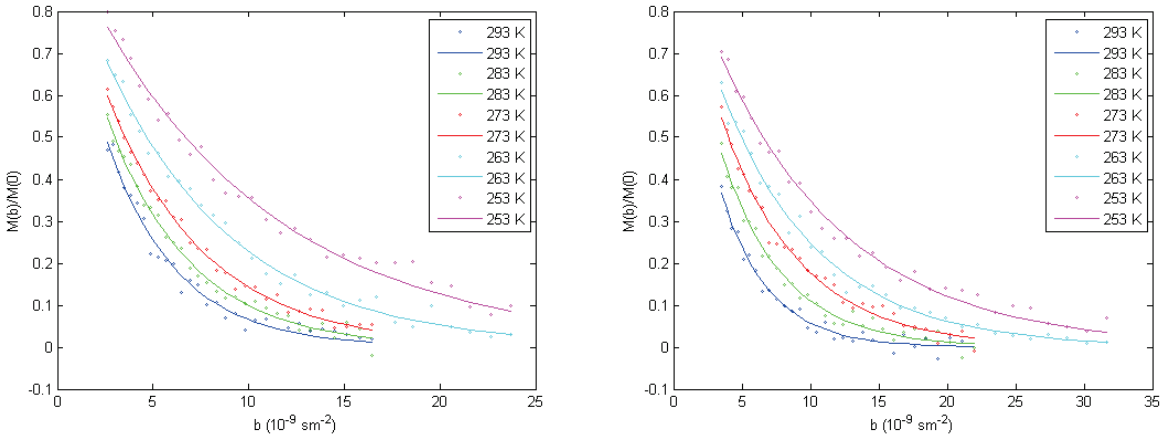

Figure H.6. Diffusion decays for *p*-xylene in MOF-5 at a loading of 39 molecules per unit cell for a diffusion time Δ of 75 ms (left) and 100 ms (right).

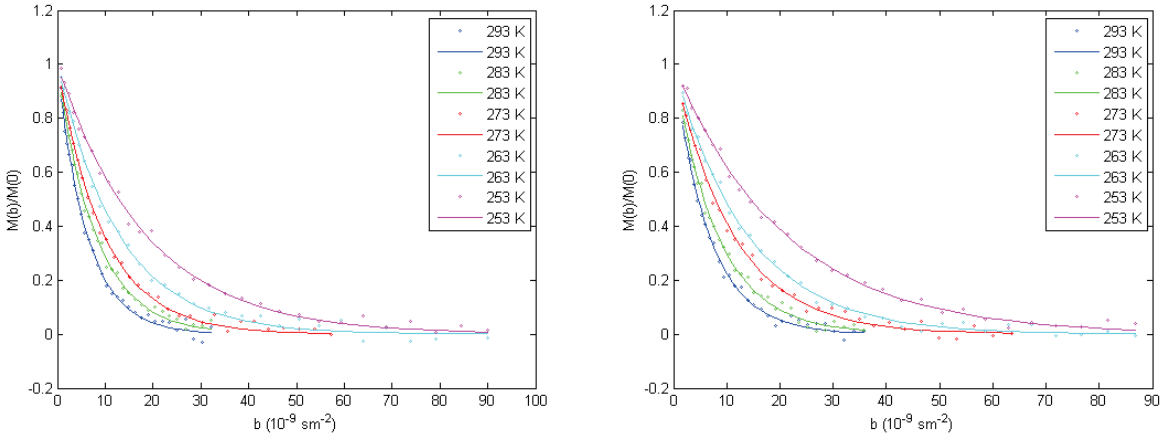

Figure H.7. Diffusion decays for anisole in MOF-5 at a loading of 67 molecules per unit cell for a diffusion time Δ of 25 ms (left) and 50 ms (right).

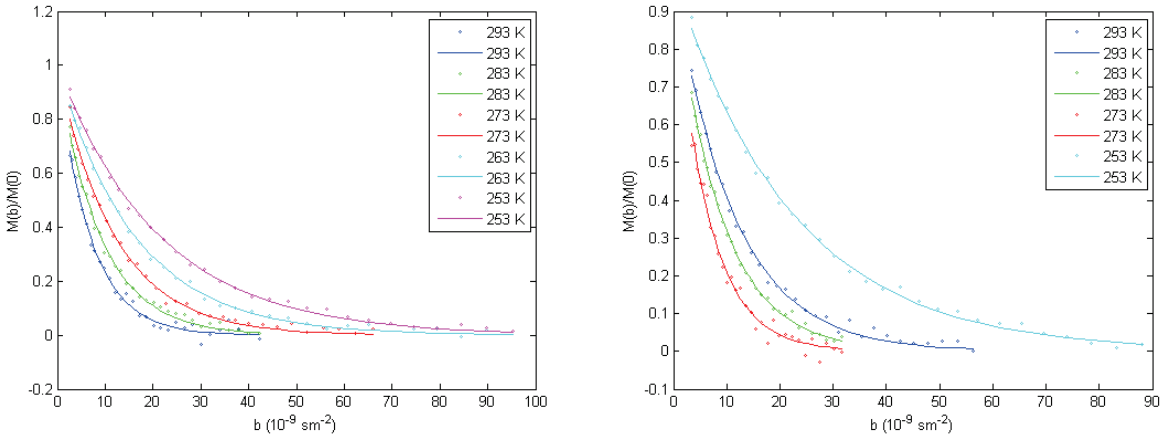

Figure H.8. Diffusion decays for anisole in MOF-5 at a loading of 67 molecules per unit cell for a diffusion time Δ of 75 ms (left) and 100 ms (right).

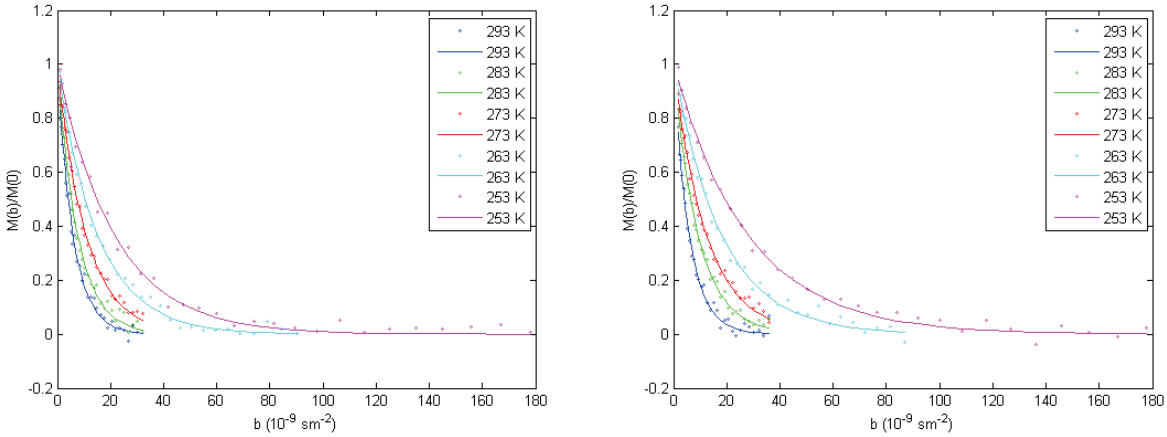

Figure H.9. Diffusion decays for anisole in MOF-5 at a loading of 50 molecules per unit cell for a diffusion time Δ of 25 ms (left) and 50 ms (right).

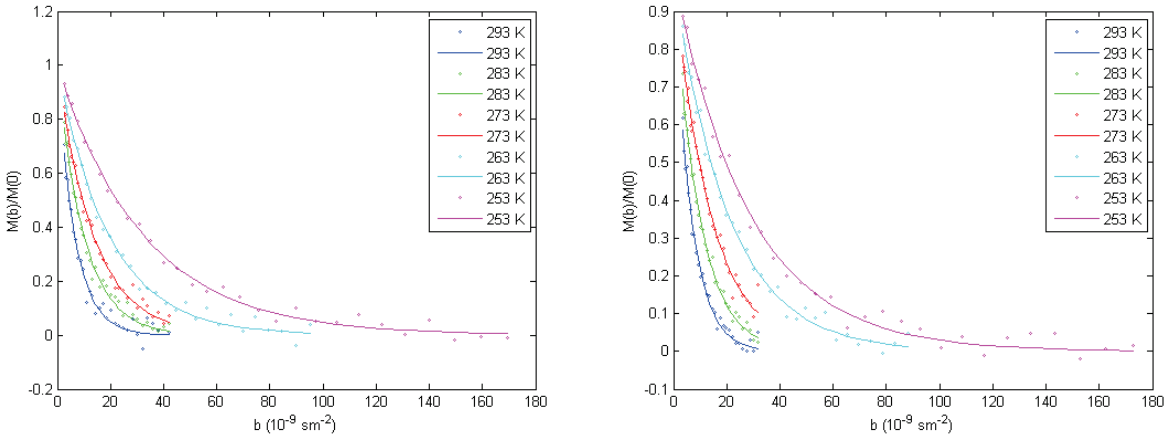

Figure H.10. Diffusion decays for anisole in MOF-5 at a loading of 50 molecules per unit cell for a diffusion time Δ of 75 ms (left) and 100 ms (right).

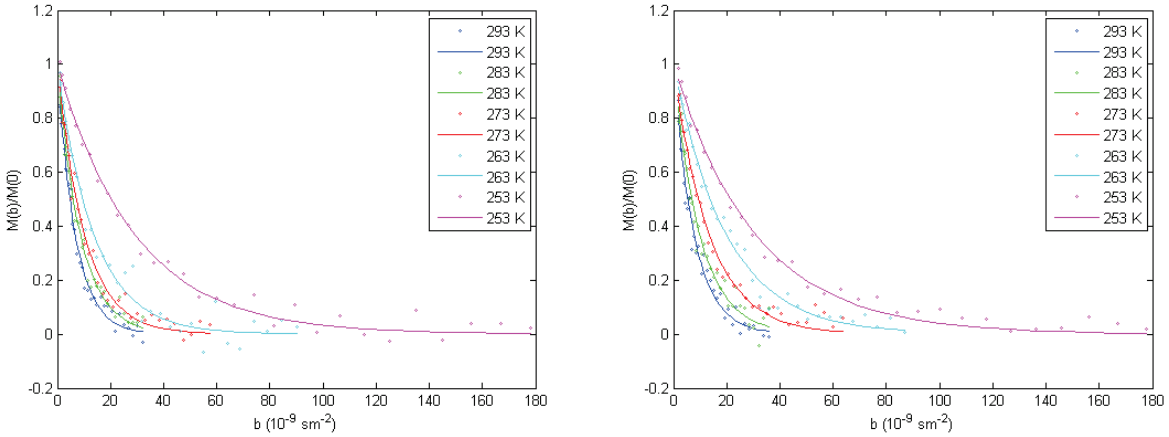

Figure H.11. Diffusion decays for anisole in MOF-5 at a loading of 36 molecules per unit cell for a diffusion time Δ of 25 ms (left) and 50 ms (right).

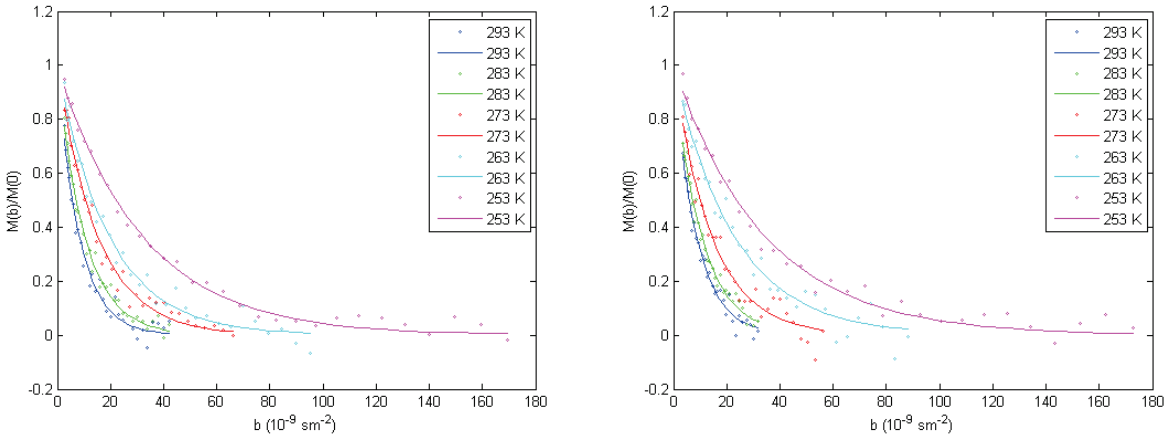

Figure H.12. Diffusion decays for anisole in MOF-5 at a loading of 36 molecules per unit cell for a diffusion time Δ of 75 ms (left) and 100 ms (right).

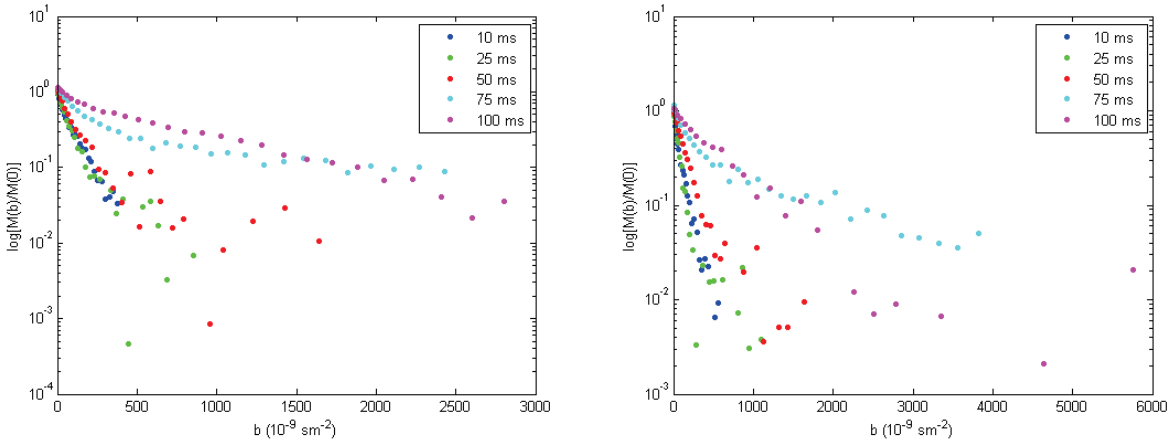

Figure H.13. Diffusion decays for anisole in IRMOF-3 at a loading of 35 molecules per unit cell for a diffusion time Δ of 10 ms, 25 ms, 50 ms, 75 ms, and 100 ms. Experiments were conducted at temperatures of 293K (left) and 263K (right). Note that the logarithmic decays are clearly non-linear at long diffusion times (Δ = 75 ms and 100 ms), indicating multi-exponential behavior.

H.2 Fit Results for Diffusion Decays

Table H.1. Diffusion coefficients from exponential fits for *p*-xylene in MOF-5

		Loading (molecules per unit cell)					
		64		49		39	
Temp (K)	**Δ (s)**	**D_{self} (m^2/s)**	**Error (m^2/s)**	**D_{self} (m^2/s)**	**Error (m^2/s)**	**D_{self} (m^2/s)**	**Error (m^2/s)**
293	0.01	3.40E-10	1.00E-11	3.70E-10	1.00E-11	3.50E-10	1.00E-11
293	0.025	3.60E-10	2.00E-11	3.28E-10	1.00E-11	3.30E-10	1.00E-11
293	0.05	3.40E-10	1.00E-11	3.15E-10	1.00E-11	3.00E-10	1.00E-11
293	0.075	3.40E-10	1.00E-11	2.80E-10	1.00E-11	2.70E-10	1.00E-11
293	0.1	3.40E-10	2.00E-11	3.20E-10	2.00E-11	2.90E-10	1.00E-11
283	0.01	3.21E-10	1.00E-11	2.87E-10	1.00E-11	2.90E-10	1.00E-11
283	0.025	3.40E-10	1.00E-11	2.58E-10	1.00E-11	2.60E-10	1.00E-11
283	0.05	2.90E-10	1.00E-11	2.56E-10	1.00E-11	2.40E-10	1.00E-11
283	0.075	2.90E-10	1.00E-11	2.34E-10	1.00E-11	2.30E-10	1.00E-11
283	0.1	2.70E-10	1.00E-11	2.38E-10	1.00E-11	2.20E-10	1.00E-11
273	0.01	2.93E-10	1.00E-11	2.40E-10	1.00E-11	2.36E-10	1.00E-11
273	0.025	2.80E-10	1.00E-11	2.08E-10	1.00E-11	2.00E-10	1.00E-11
273	0.05	2.60E-10	1.00E-11	2.03E-10	1.00E-11	1.99E-10	3.00E-12
273	0.075	2.46E-10	1.00E-11	1.88E-10	1.00E-11	1.95E-10	3.00E-12
273	0.1	2.50E-10	1.00E-11	1.82E-10	1.00E-11	1.73E-10	1.00E-11
263	0.01	2.23E-10	1.00E-11	1.71E-10	4.00E-12	1.86E-10	1.00E-11
263	0.025	2.08E-10	1.00E-11	1.51E-10	4.00E-12	1.60E-10	1.00E-11
263	0.05	1.94E-10	1.00E-11	1.50E-10	3.00E-12	1.49E-10	1.00E-11
263	0.075	1.83E-10	1.00E-11	1.48E-10	4.00E-12	1.48E-10	1.00E-11
263	0.1	1.82E-10	1.00E-11	1.43E-10	4.00E-12	1.42E-10	4.00E-12
253	0.01	1.80E-10	1.00E-11	1.33E-10	3.00E-12	1.35E-10	2.00E-12
253	0.025	1.59E-10	1.00E-11	1.13E-10	3.00E-12	1.14E-10	2.00E-12
253	0.05	1.42E-10	1.00E-11	1.11E-10	2.00E-12	1.12E-10	2.00E-12
253	0.075	1.39E-10	1.00E-11	1.05E-10	2.00E-12	1.04E-10	3.00E-12
253	0.1	~	~	1.00E-10	2.00E-12	1.06E-10	3.00E-12

Table H.2. Diffusion coefficients from exponential fits for anisole in MOF-5

		Loading (molecules per unit cell)					
		67		50		36	
Temp (K)	**Δ (s)**	**D_{self} (m^2/s)**	**Error (m^2/s)**	**D_{self} (m^2/s)**	**Error (m^2/s)**	**D_{self} (m^2/s)**	**Error (m^2/s)**
293	0.01	1.79E-10	4.00E-12	1.80E-10	4.00E-12	1.62E-10	4.00E-12
293	0.025	1.61E-10	4.00E-12	1.70E-10	4.00E-12	1.48E-10	4.00E-12
293	0.05	1.49E-10	4.00E-12	1.68E-10	4.00E-12	1.29E-10	4.00E-12
293	0.075	1.47E-10	5.00E-12	1.52E-10	5.00E-12	1.22E-10	5.00E-12
293	0.1	1.56E-10	6.00E-12	1.53E-10	6.00E-12	1.17E-10	6.00E-12
283	0.01	1.42E-10	3.00E-12	1.28E-10	3.00E-12	1.29E-10	3.00E-12
283	0.025	1.25E-10	2.00E-12	1.32E-10	2.00E-12	1.17E-10	2.00E-12
283	0.05	1.21E-10	3.00E-12	1.07E-10	3.00E-12	1.02E-10	3.00E-12
283	0.075	1.11E-10	2.00E-12	1.00E-10	2.00E-12	9.90E-11	2.00E-12
283	0.1	1.14E-10	2.00E-12	1.05E-10	2.00E-12	9.50E-11	2.00E-12
273	0.01	1.16E-10	2.00E-12	9.60E-11	2.00E-12	9.40E-11	2.00E-12
273	0.025	1.03E-10	2.00E-12	9.30E-11	2.00E-12	9.90E-11	2.00E-12
273	0.05	8.90E-11	2.00E-12	8.00E-11	2.00E-12	7.60E-11	2.00E-12
273	0.075	8.40E-11	2.00E-12	7.30E-11	2.00E-12	6.80E-11	2.00E-12
273	0.1	9.00E-11	2.00E-12	7.20E-11	2.00E-12	7.00E-11	2.00E-12
263	0.01	9.50E-11	2.00E-12	7.10E-11	2.00E-12	7.50E-11	2.00E-12
263	0.025	7.80E-11	2.00E-12	6.60E-11	2.00E-12	7.40E-11	2.00E-12
263	0.05	7.20E-11	2.00E-12	5.50E-11	2.00E-12	5.00E-11	2.00E-12
263	0.075	6.20E-11	1.00E-12	5.20E-11	1.00E-12	5.20E-11	1.00E-12
263	0.1	~	~	4.90E-11	1.00E-12	4.40E-11	1.00E-12
253	0.01	6.70E-11	1.00E-12	5.10E-11	1.00E-12	4.50E-11	1.00E-12
253	0.025	5.40E-11	1.00E-12	4.70E-11	1.00E-12	3.50E-11	1.00E-12
253	0.05	4.80E-11	1.00E-12	3.60E-11	1.00E-12	3.20E-11	1.00E-12
253	0.075	4.70E-11	1.00E-12	3.10E-11	1.00E-12	3.20E-11	1.00E-12
253	0.1	4.50E-11	1.00E-12	3.50E-11	1.00E-12	3.10E-11	1.00E-12

Table H.3. Diffusion coefficients from exponential fits for *p*-xylene in IRMOF-3

		Loading (molecules per unit cell)			
		54		35	
Temp (K)	**Δ (s)**	**D_{self} (m^2/s)**	**Error (m^2/s)**	**D_{self} (m^2/s)**	**Error (m^2/s)**
293	0.01	1.54E-10	3.00E-12	1.64E-10	6.00E-12
293	0.025	1.38E-10	3.00E-12	1.38E-10	6.00E-12
293	0.05	1.44E-10	4.00E-12	1.38E-10	7.00E-12
293	0.075	1.44E-10	4.00E-12	1.23E-10	6.00E-12
293	0.1	1.37E-10	5.00E-12	1.13E-10	6.00E-12
283	0.01	1.30E-10	3.00E-12	1.29E-10	5.00E-12
283	0.025	1.25E-10	3.00E-12	1.08E-10	4.00E-12
283	0.05	1.32E-10	3.00E-12	1.02E-10	5.00E-12
283	0.075	1.21E-10	4.00E-12	9.50E-11	6.00E-12
283	0.1	1.27E-10	4.00E-12	1.07E-10	5.00E-12
273	0.01	1.09E-10	3.00E-12	9.50E-11	3.00E-12
273	0.025	1.05E-10	3.00E-12	8.10E-11	4.00E-12
273	0.05	1.01E-10	2.00E-12	7.50E-11	5.00E-12
273	0.075	1.06E-10	3.00E-12	7.50E-11	6.00E-12
273	0.1	9.70E-11	3.00E-12	7.10E-11	5.00E-12
263	0.01	9.60E-11	1.00E-12	7.10E-11	2.00E-12
263	0.025	8.70E-11	1.00E-12	5.00E-11	1.00E-12
263	0.05	8.30E-11	2.00E-12	4.80E-11	1.00E-12
263	0.075	8.30E-11	2.00E-12	4.40E-11	2.00E-12
263	0.1	7.70E-11	2.00E-12	4.20E-11	2.00E-12
253	0.01	7.59E-11	1.00E-12	7.10E-11	3.00E-12
253	0.025	7.00E-11	1.00E-12	4.30E-11	1.00E-12
253	0.05	6.80E-11	1.00E-12	4.20E-11	2.00E-12
253	0.075	6.60E-11	1.00E-12	3.50E-11	1.00E-12
253	0.1	6.70E-11	2.00E-12	3.20E-11	2.00E-12

Table H.4. Diffusion coefficients from exponential fits for anisole in IRMOF-3

		Loading (molecules per unit cell)			
		62		53	
Temp (K)	**Δ (s)**	**D_{self} (m^2/s)**	**Error (m^2/s)**	**D_{self} (m^2/s)**	**Error (m^2/s)**
293	0.01	1.01E-10	2E-12	1.01E-10	0.002
293	0.025	9.1E-11	2E-12	9E-11	0.002
293	0.05	9.3E-11	2E-12	8.6E-11	0.002
293	0.075	8.8E-11	2E-12	8.2E-11	0.002
293	0.1	8.6E-11	2E-12	7.5E-11	0.002
283	0.01	8.1E-11	2E-12	8.4E-11	2E-12
283	0.025	7.6E-11	1E-12	7.1E-11	2E-12
283	0.05	7.23E-11	9E-13	6.8E-11	1E-12
283	0.075	7E-11	2E-12	6.3E-11	2E-12
283	0.1	7.4E-11	2E-12	5.8E-11	1E-12
273	0.01	8.1E-11	2E-12	5.8E-11	2E-12
273	0.025	8.3E-11	2E-12	5.06E-11	1E-12
273	0.05	6.6E-11	1E-12	4.74E-11	1E-12
273	0.075	6.3E-11	2E-12	4.13E-11	9E-13
273	0.1	6.2E-11	2E-12	3.97E-11	9E-13
263	0.01	6.3E-11	2E-12	3.1E-11	1E-12
263	0.025	6E-11	1E-12	3.14E-11	6E-13
263	0.05	5.1E-11	1E-12	2.72E-11	6E-13
263	0.075	4.9E-11	1E-12	1.97E-11	6E-13
263	0.1	4.76E-11	9E-13	1.8E-11	5E-13
253	0.01	5.4E-11	2E-12	2.28E-11	9E-13
253	0.025	4.7E-11	1E-12	2.82E-11	5E-13
253	0.05	3.83E-11	7E-13	2.11E-11	7E-13
253	0.075	3.61E-11	1E-12	1.11E-11	4E-13
253	0.1	3.6E-11	1E-12	9.9E-12	3E-13

Table H.5. Results for Arrhenius fits to diffusion data

	Molecules per cage	$E_{a,diff}$ (kJ/mol)	Error (kJ/mol)	D_0 (m²/s)	Error (m²/s)	T_1 E_a (kJ/mol)	Error (kJ/mol)
MOF-5 *p*-xylene	63	14	1	1.3E-07	7E-08	10.3	0.8
	49	16.5	0.5	2.6E-07	6E-08	9.2	0.4
	39	15.3	0.5	1.5E-07	3E-08	10.5	0.5
MOF-5 anisole	67	18.6	0.2	3E-07	3E-08	16.3	0.8
	50	23.5	0.5	2.3E-06	5E-07	15	3
	36	22	2	9E-07	7E-07	13	1
IRMOF-3 *p*-xylene	54	12.1	0.9	2E-08	7.00E-09	10	1
	35	23	2	1.00E-06	1.00E-06	11	2
IRMOF-3 anisole	62	14	1	3.00E-08	1.00E-08	15	1
	53	27	2	5.00E-06	4.00E-06	16	1

H.3 T_2 Relaxation Distributions for *p*-Xylene and Anisole in IRMOF-3

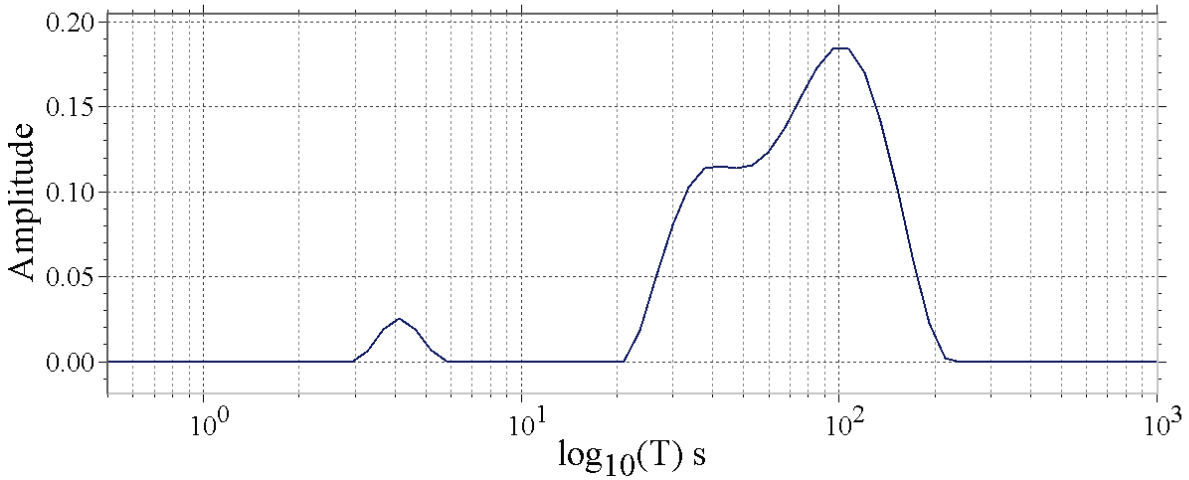

Figure H.14. T_2 relaxation distribution for 35 molecules of *p*-xylene per unit cell of IRMOF-3 obtained at 13 MHz.

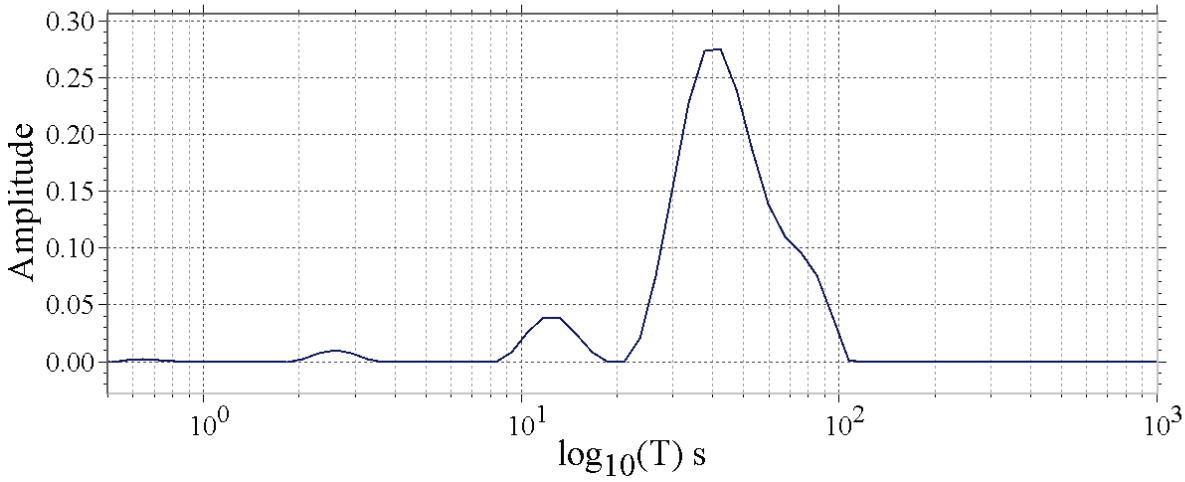

Figure H.15. T_2 relaxation distribution for 53 molecules of anisole per unit cell of IRMOF-3 obtained at 13 MHz

H.4 Diffusion Results for Neat *p*-Xylene and Anisole

The measured activation energies for the diffusion of neat *p*-xylene and anisole are 11 ± 4 kJ/mol and 14 ± 3 kJ/mol respectively.

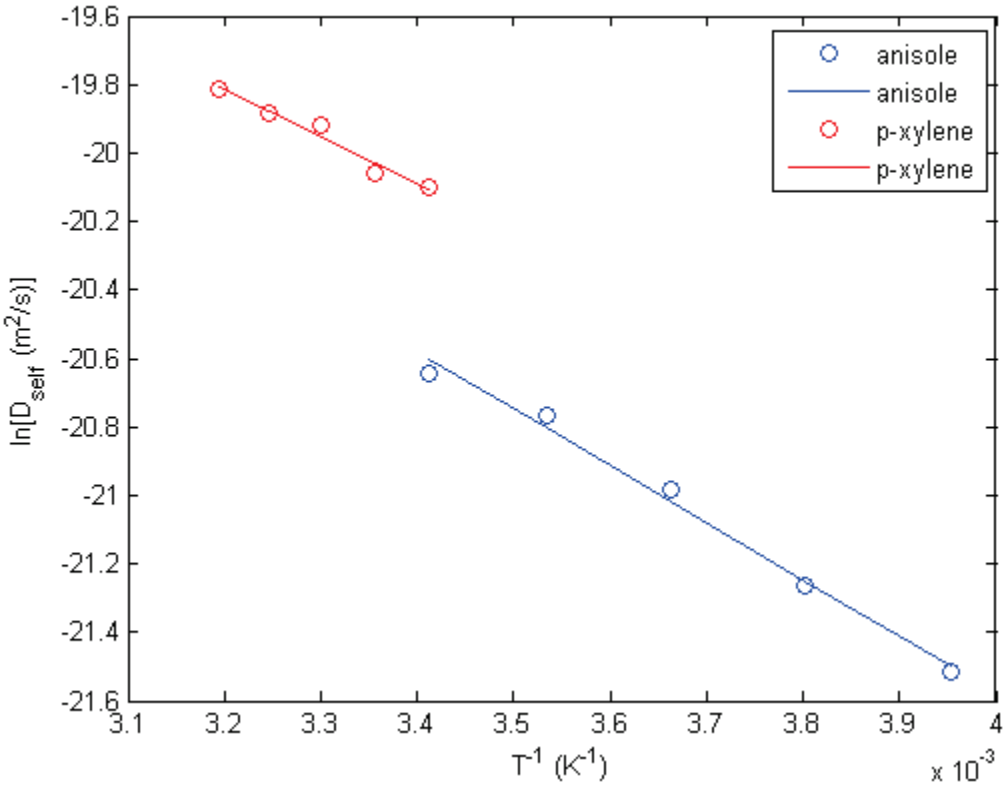

Figure H.16. Arrhenius plot of neat solvent diffusion coefficients.

H.5 Polarized Optical Micrographs of MOF-5

Images were acquired using an Olympus BX51 optical microscope equipped with an Olympus UAN360P polarizer. The polarizers were crossed in the image taken below.

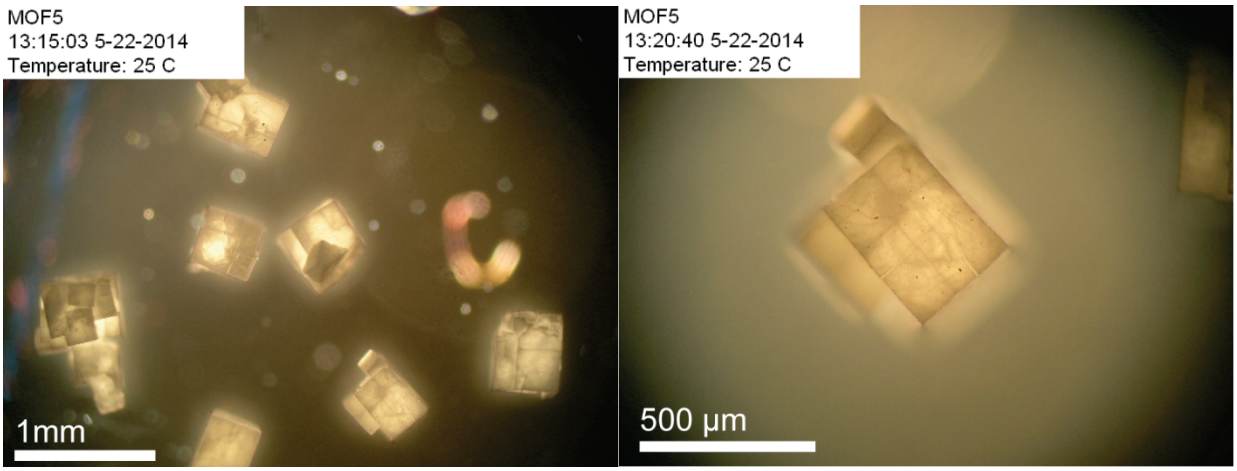

Figure H.17. Polarized optical micrographs of MOF-5 crystals

Appendix I
Supplementary Figures for Condensation Studies

I.1 MC Simulation Figures

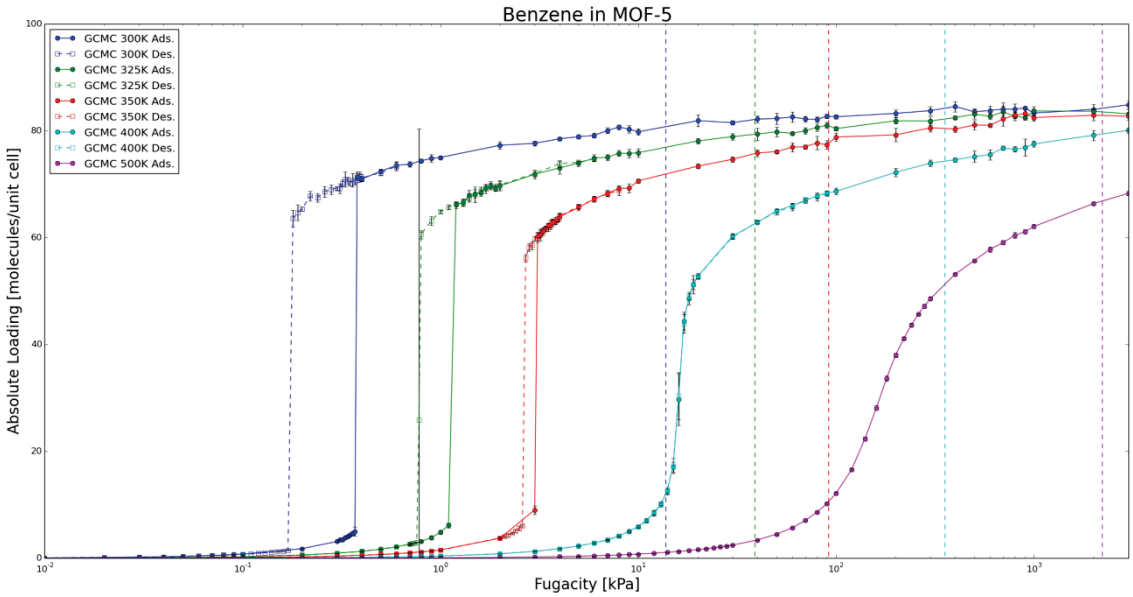

Figure I.1. Isotherms of benzene in IRMOF-1.

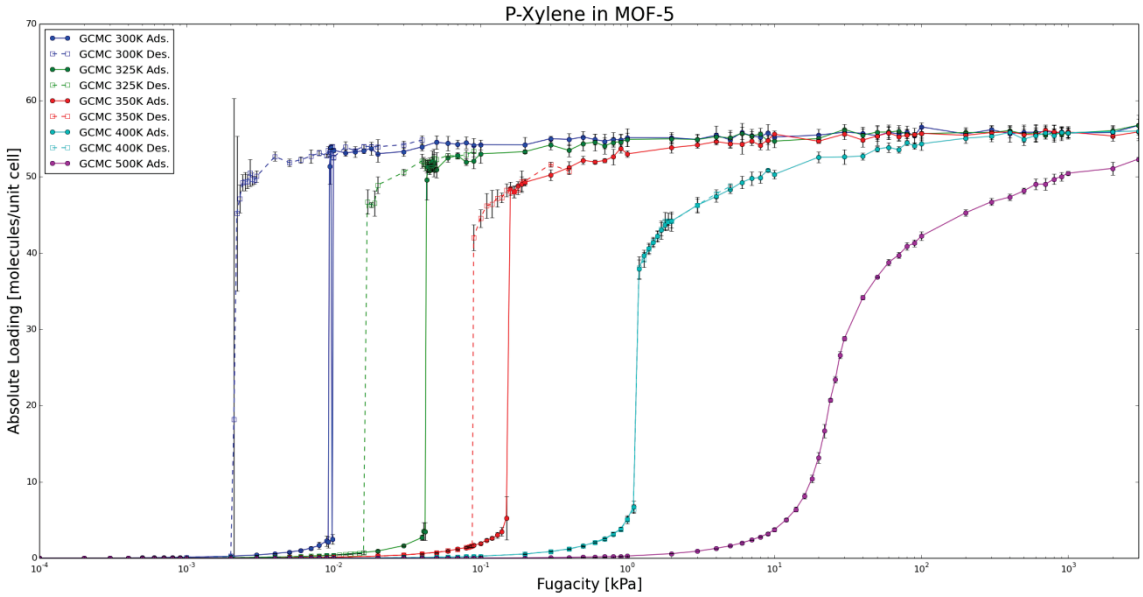

Figure I.2. Isotherms of *p*-xylene in IRMOF-1.

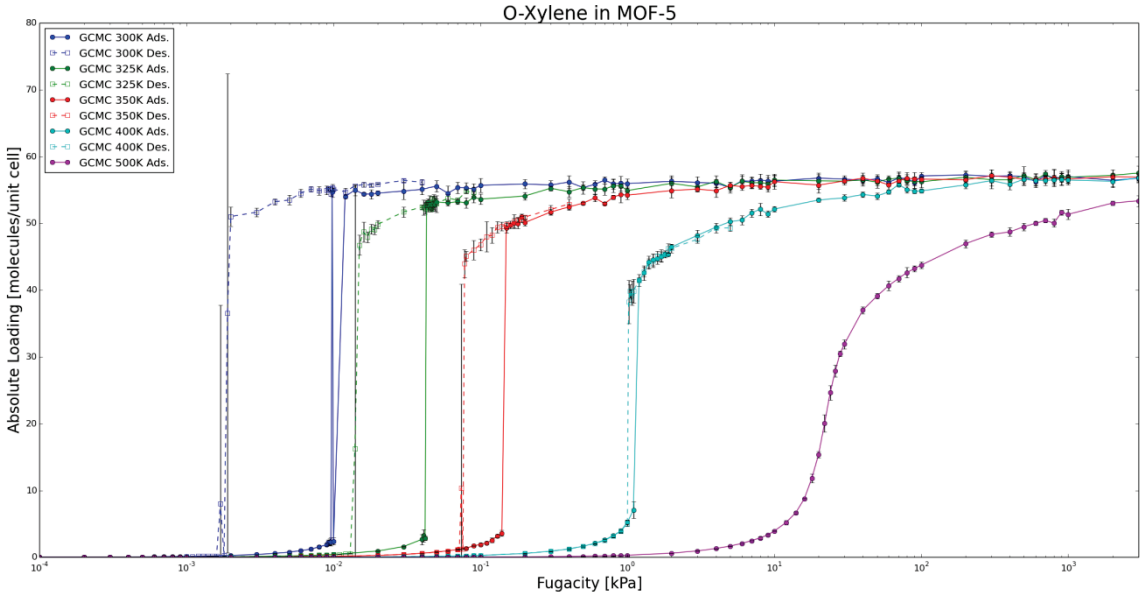

Figure I.3. Isotherms of *o*-xylene in IRMOF-1.

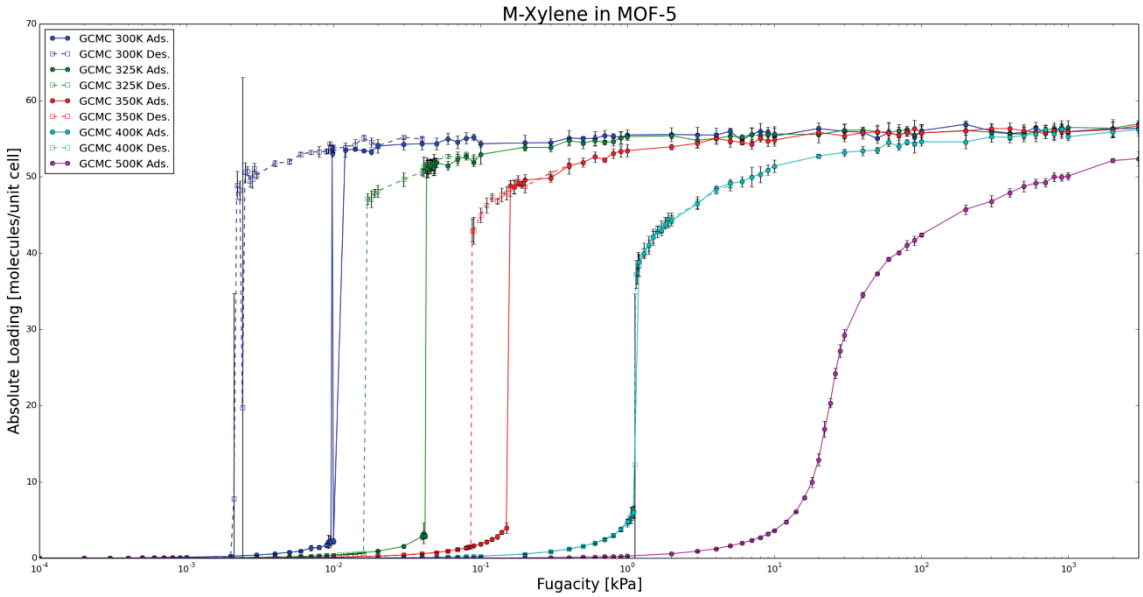

Figure I.4. Isotherms of *m*-xylene in IRMOF-1.

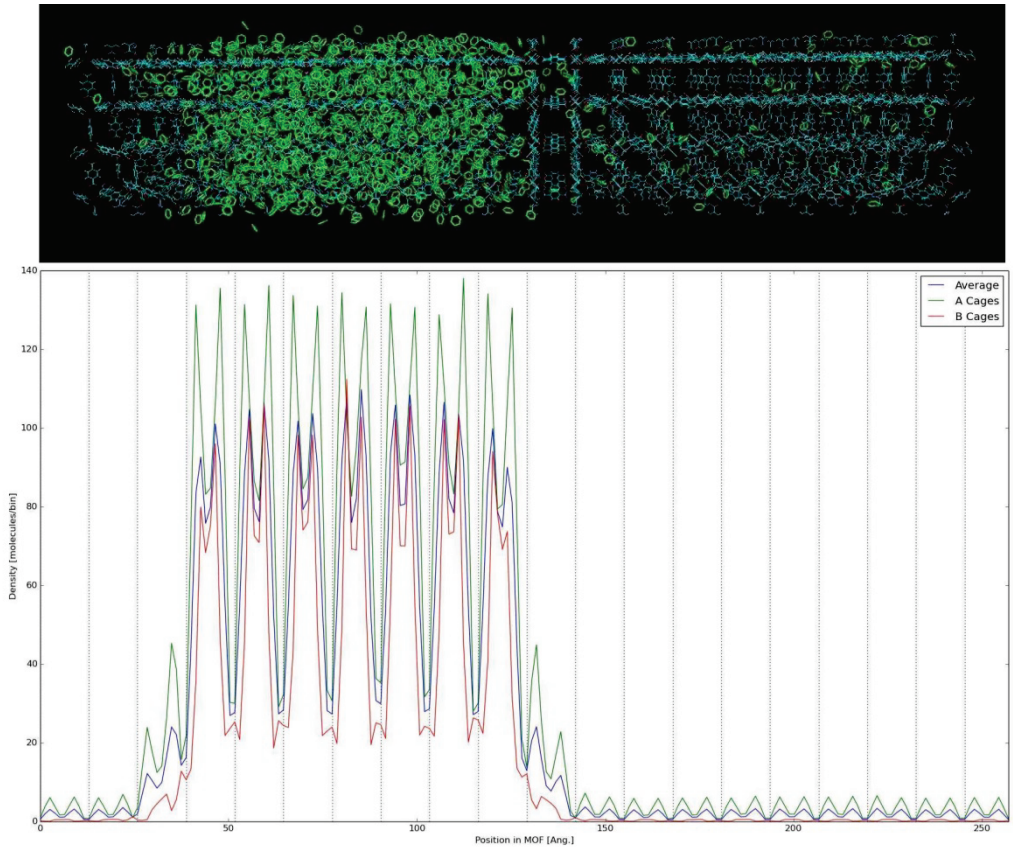

Figure I.5. IRMOF-1 has two different types of cages: A cages, in which the phenylene ring planes face inside, and B cages, in which the phenylene ring sides face inside. In the liquid phase, density maximas are towards the corners in both cage types. In the vapor phase, density maximas in the A cages are towards the corners, but density maximas in the B cages are in the centers.

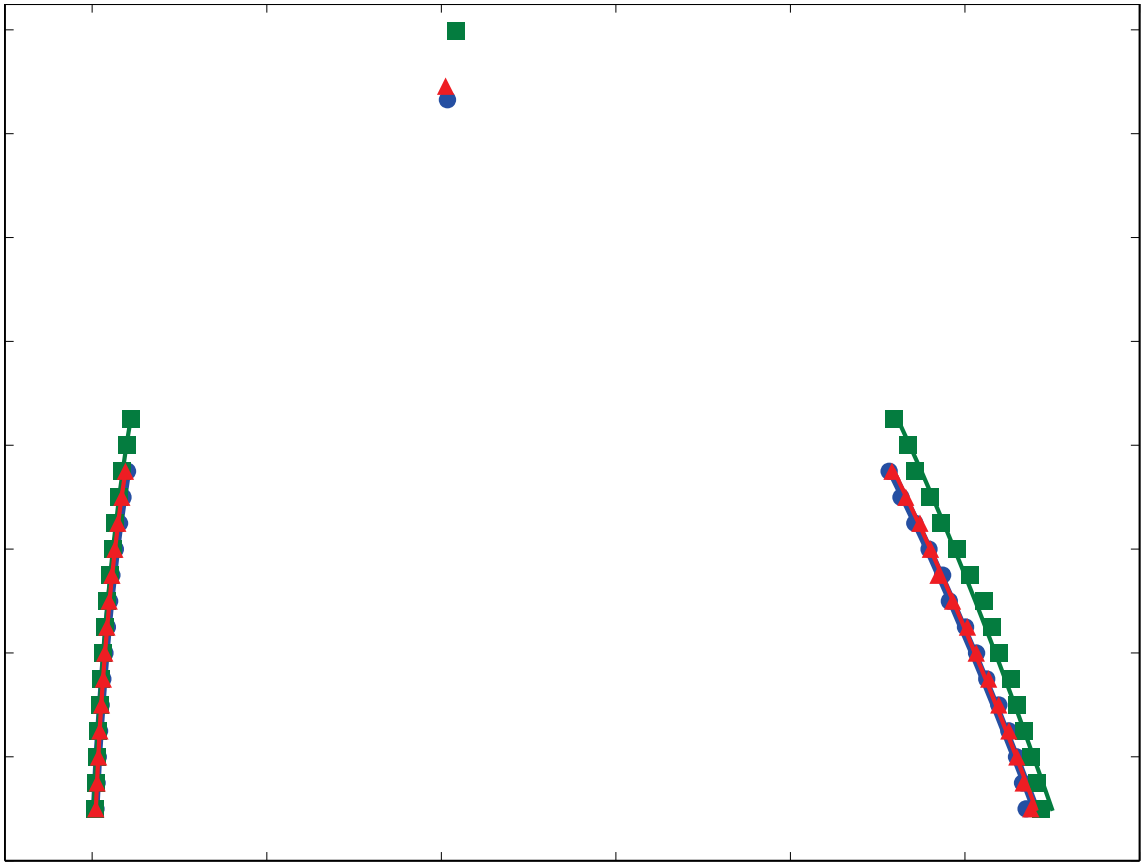

Figure I.6. Density-temperature phase diagram for *p*-xylene, *o*-xylene, and *m*-xylene in IRMOF-1 (blue circles, green squared, and red triangles, respectively).

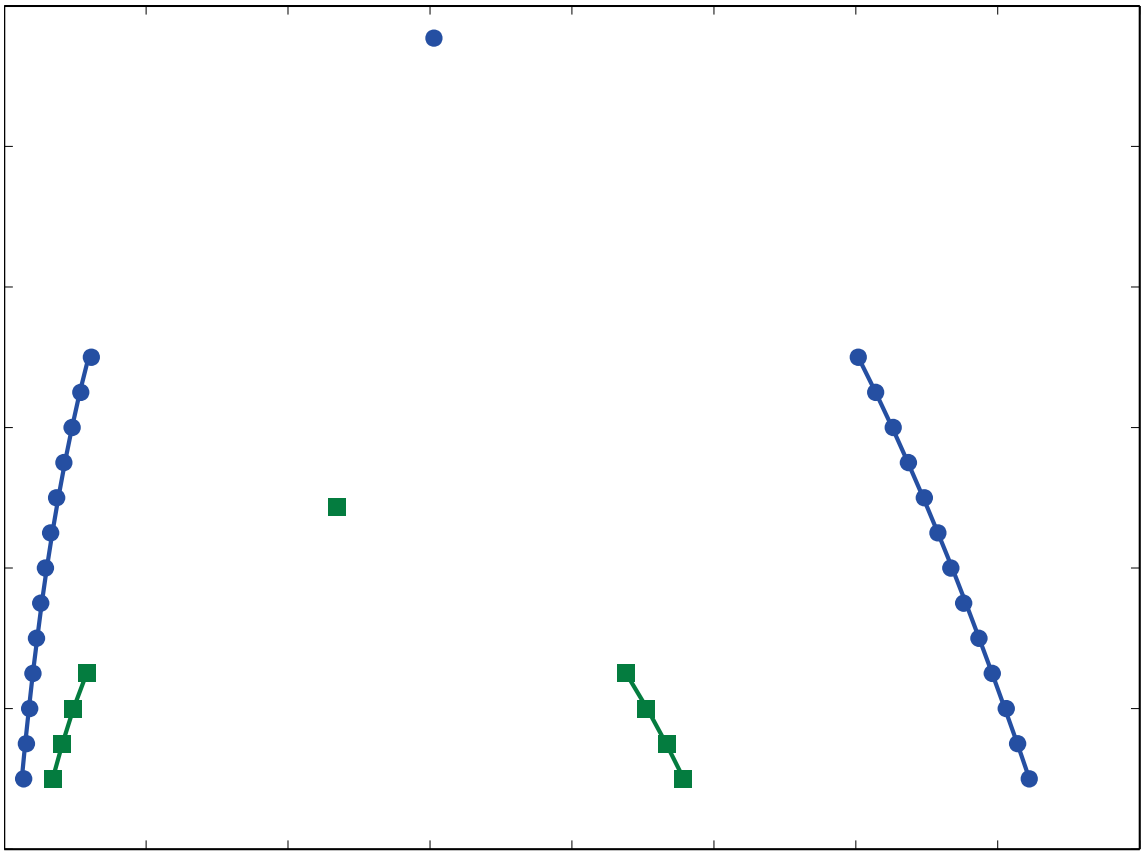

Figure I.7. Density-temperature phase diagram for benzene in IRMOF-1 (blue circle) and IRMOF-7 (green squares).

Table I.1. Critical temperature of benzene in various IRMOFs. Cage size is defined as one-half of the unit cell's edge length.

IRMOF	Cage Size (Å)	T_c (K)
IRMOF-1	12.916	375
IRMOF-7	12.914	309
IRMOF-10	17.140	381
IRMOF-14	17.191	353
IRMOF-16	21.490	429

I.2 NMR Experiment Figures

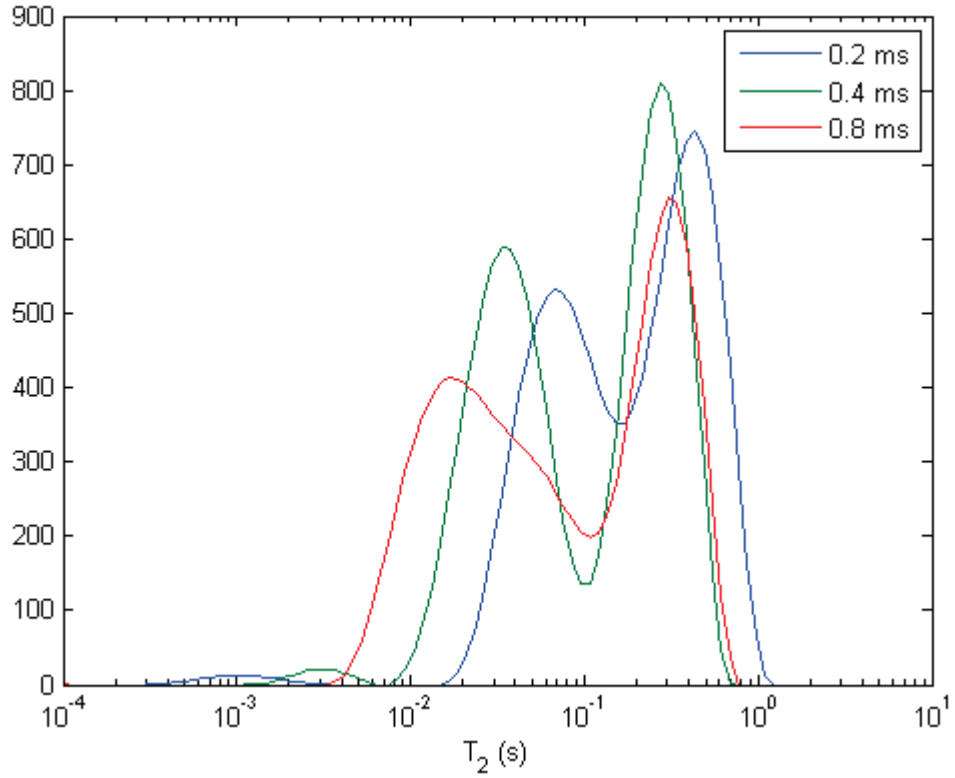

Figure I.8. Relaxation distributions with varying t_{echo} of benzene in IRMOF-1 (9 ± 1 molecules per unit cell) at 343K.

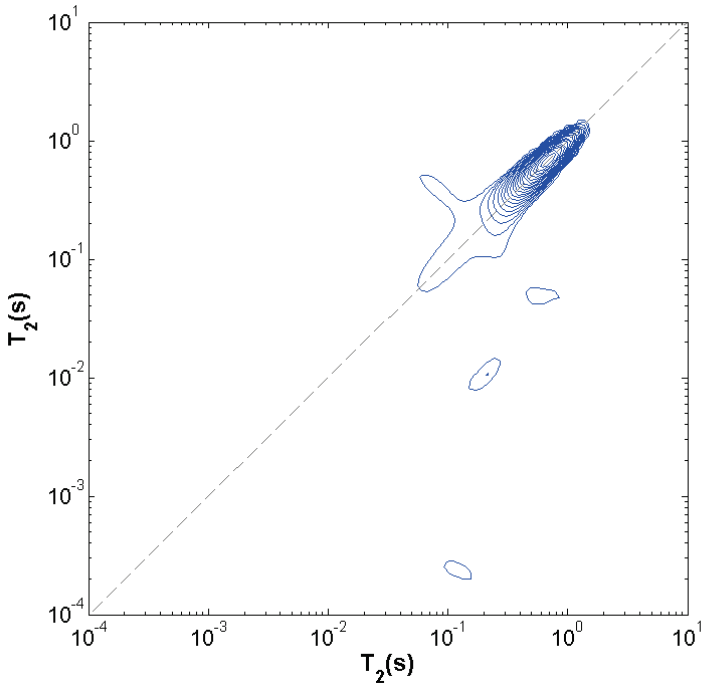

Figure I.9. T_2-T_2 relaxation exchange distribution at 295K of IRMOF-1 containing 7 molecules of p-xylene per unit cell illustrating the presence of exchange between distinct phases within a timescale of t_{echo}=500ms.

I.3 Discussion of Relaxation Distribution at 343K

The presence of field gradients at 295K results in the decrease in total signal intensity with increasing t_{echo}. This decrease indicates that some proportion of benzene molecules experience such strong gradients that they become undetectable due to substantially shortened T_2; thus at long t_{echo} a proportion of the signal attenuates before it can be detected. As temperature increases, the gradient strength decreases and T_2 increases. Therefore, components undetectable at 295K may become detectable at 343K; such components would still exhibit relatively short T_2 times, and thus, may explain the shift seen to lower relaxation times seen in the relaxation distributions at 343K.